U.S. DEPARTMENT OF INTERIOR
GEOLOGICAL SURVEY

OBSERVATIONS AND MODELING OF SEISMIC BACKGROUND NOISE

Jon Peterson

Open-File Report 93-322

This report is preliminary and has not been reviewed for conformity with U.S. Geological Survey editorial standards. Any use of trade names is for descriptive purposes only and does not imply endorsement by the U.S. Geological Survey.

Albuquerque, New Mexico

1993

TABLE OF CONTENTS

INTRODUCTION 1
THE DATABASE 2
Stations 2
Definition of Data Bands 7
Data Systems 7
SRO Systems 7
ASRO Systems 8
DWWSSN Systems 8
CDSN Systems 8
IRIS/USGS Systems 9
IRIS/IDA Systems 9
RSTN Systems 10
TERRAscope Systems 10
DATA PREPARATION 11
Data Selection 11
Data Processing 12
STATION NOISE SPECTRA 13
Presentation of Station Data 13
Spectral Overlay 13
Non-Seismic Noise 15
Short-Period Seismic Noise 18
Long-Period Seismic Noise 20
NOISE MODELS 30
Background 30
New Noise Models 30
Amplitude Spectra 35
ACKNOWLEDGEMENTS 39
REFERENCES 41

APPENDIX

INTRODUCTION

The preparation of this report had two purposes. One was to present a catalog of seismic background noise spectra obtained from a worldwide network of seismograph stations. The other purpose was to refine and document models of seismic background noise that have been in use for several years. The second objective was, in fact, the principal reason that this study was initiated and influenced the procedures used in collecting and processing the data.

With a single exception, all of the data used in this study were extracted from the digital data archive at the U.S. Geological Survey's Albuquerque Seismological Laboratory (ASL). This archive dates from 1972 when ASL first began deploying digital seismograph systems and collecting and distributing digital data under the sponsorship of the Defense Advanced Research Projects Agency (DARPA). There have been many changes and additions to the global seismograph networks during the past twenty years, but perhaps none as significant as the current deployment of very broadband seismographs by the U.S. Geological Survey (USGS) and the University of California San Diego (UCSD) under the scientific direction of the IRIS consortium. The new data acquisition systems have extended the bandwidth and resolution of seismic recording, and they utilize high-density recording media that permit the continuous recording of broadband data. The data improvements and continuous recording greatly benefit and simplify surveys of seismic background noise.

Although there are many other sources of digital data, the ASL archive data were used almost exclusively because of accessibility and because the data systems and their calibration are well documented for the most part. Fortunately, the ASL archive contains high-quality data from other stations in addition to those deployed by the USGS. Included are data from UCSD IRIS/IDA stations, the Regional Seismic Test Network (RSTN) deployed by Sandia National Laboratories (SNL), and the TERRAscope network deployed by the California Institute of Technology in cooperation with other institutions.

A map showing the approximate locations of the stations used in this study is provided in Figure 1. One might hope for a better distribution of stations in the southern hemisphere, especially Africa and South America, in order to look for regional variations in seismic noise (apart from the major differences between continental, coastal and island sites). Unfortunately, anyone looking for subtle regional variations in seismic noise is probably going to be disappointed by the spectral data presented in this report because much of the station data appear to be dominated by local disturbances caused by instrumental, environmental, cultural, or surf noise. Better instruments and better instrument siting, or a well-funded field program, will be needed before a global isoseismal noise map can be produced. However, by assembling a composite of background noise from a large network of stations, many of the local station variables are masked, and it is possible to create generalized spectral plots of Earth noise for hypothetical quiet and noisy station sites.

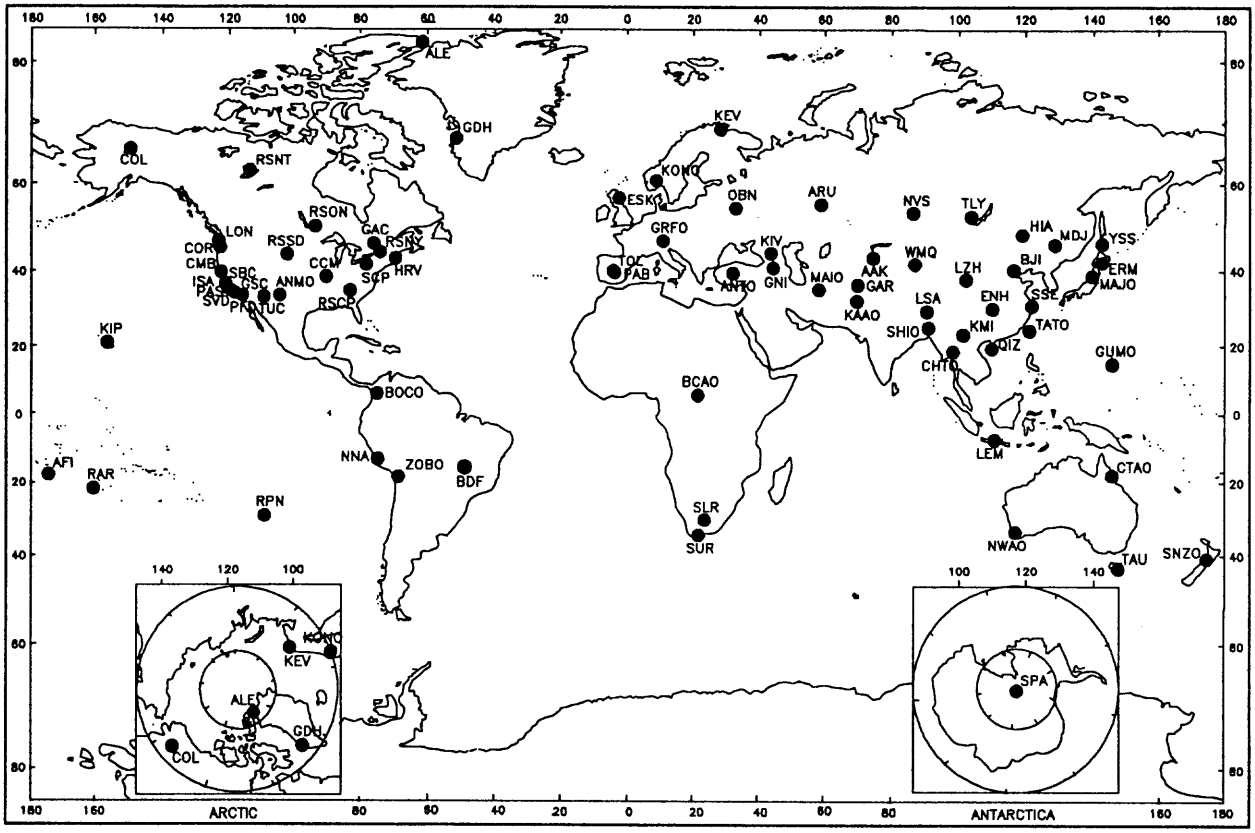

Figure 1.--Map showing the approximate locations of the stations used in this report.

THE DATABASE

Stations

Seismic data from 75 stations have been used in this study. All but one of the stations are part of what will be generically referred to as the global seismograph network, and all of the data recorded at the network stations, with the exception of some test data, are available to anyone through either the USGS or IRIS data management centers. The codes, coordinates, type of data system, and vault and site characteristics, if known, are listed in Table 1. A few of the data systems are no longer in operation, and one of the stations listed, ALQ, is a test system at ASL that operates intermittently. Several of the stations have been the subjects of previous background noise studies, generally in greater scope and detail than reported in this study. An analysis of seismic noise recorded at the five RSTN stations has been published by Rodgers and others (1987) and Breding (1987). Given (1990) has published a detailed report on seismic noise recorded at three of the IRIS/IDA sites listed in Table 1 (ARU, KIV, OBN).

CODE	LOCATION	TYPE	LAT	LONG	ELEV (M)	VAULT TYPE	DEPTH (M)	GEOLOGY
AAK	Ala Archa, Kyrgyzstan	IRIS/IDA	42.64N	74.49E	1645	Subsurface		Granitic
AFI	Afiamalu, Western Samoa	DWWSSN	13.91S	171.78W	706	Surface	2	Volcanics
ALE	Alert, Canada	IRIS/IDA	82.50N	62.35W	60			
ALQ	Albuquerque, New Mexico, USA	IRIS-2	34.94N	106.46W	1849	Subsurface	36	Granite
ANMO	Albuquerque, New Mexico, USA	IRIS-2	34.94N	106.46W	1740	Borehole	100	Granite
ANTO	Ankara, Turkey	SRO	39.87N	32.79E	883	Borehole	195	
ARU	Arti, Russian Federation	IRIS/IDA	56.40N	58.60E	250	Surface		Sandstone
BCAO	Bangui, Central African Republic	SRO	4.43N	18.54E	336	Borehole	64	Chert
BDF	Brasilia, Brazil	DWWSSN	15.66S	47.90W	1260	Surface		Quartzite/Slate
BJI	Baijatuan, Beijing, China	CDSN	40.04N	116.18E	43	Subsurface BB/LP Borehole SP	5 153	Alluvium Limestone
BOCO	Bogota, Columbia	SRO	4.59N	74.04W	3071	Borehole	100	Limestone
CCM	Cathedral Cave, Missouri, USA	IRIS-1	38.06N	91.24W	223	Subsurface	51	Limestone
CHTO	Chiangmai, Thailand	IRIS-2	18.79N	98.98E	316	Borehole	100	Granite
CMB	Columbia College, California, USA	DWWSSN	38.04N	120.39W	719	Surface		Limestone
COL	College, Alaska, USA	IRIS-2	64.90N	147.79W	320	Surface		Schist
COR	Corvallis, Oregon, USA	IRIS-1	44.59N	123.30W	121	Surface		Basalt
CTAO	Charters Towers, Australia	IRIS-2	20.09S	146.25E	357	Subsurface	37	Granodiorite
ENH	Enshi, Hubei Province, China	CDSN	30.27N	109.49E	487	Surface		Limestone

Table 1.--Locations and other parameters of stations used in this report.

CODE	LOCATION	TYPE	LAT	LONG	ELEV (M)	VAULT TYPE	DEPTH (M)	GEOLOGY
ERM	Erimo, Japan	IRIS/IDA	42.02N	143.15E	40	Subsurface	30	Slate
ESK	Eskdalemuir, Scotland, UK	IRIS/IDA	55.32N	3.21W	242	Surface		Graywacke
GAC	Glen Almond, Ontario, Canada	SRO	45.70N	75.48W	62	Borehole	100	Granite
GAR	Garm, Tajikistan	IRIS/IDA	39.00N	70.32E	1300	Subsurface	30	Granitic
GDH	Godhavn, Greenland	DWWSSN	69.25N	53.53W	23	Surface		Gneiss
GNI	Garni, Republic of Armenia	IRIS-2	40.05N	44.72E	1460	Subsurface	60	Basalt/Tuff
GRFO	Grafenburg, Germany	SRO	49.69N	11.22E	425	Borehole	100	Limestone
GSC	Goldstone, California, USA	TERRA	35.30N	116.81W	990	Surface		Granite
GUMO	Guam, Marianas Islands	IRIS-2	13.59N	144.87E	14	Borehole	100	Limestone
HIA	Hailar, Neimengu Province, China	CDSN	49.27N	119.74E	610	Subsurface	15	Andesite
HRV	Harvard, Massachusetts	IRIS-1	42.51N	71.56W	180	Surface		Granite
ISA	Isabella, California	TERRA	35.66N	118.47W	835	Surface		Granitic
KAAO	Kabul, Afghanistan	ASRO	34.54N	69.04E	1920	Surface		Banded Gneiss
KEV	Kevó, Finland	DWWSSN	69.76N	27.00E	80	Subsurface	15	Granite
KIP	Kipapa, Hawaii, USA	IRIS-2	21.42N	158.02W	70	Subsurface	36	Basalt
KIV	Kislovodsk, Russian Federation	IRIS/IDA	43.95N	42.68E	1206	Surface		Limestone
KMI	Kunming, Yunnan Province, China	CDSN	25.12N	102.74E	1945	Subsurface	27	Limestone
KONO	Kongsberg, Norway	IRIS-2	59.65N	9.60E	216	Subsurface	340	Gneiss
LEM	Lembang, Indonesia	DWWSSN	6.83S	107.62E	1252	Surface		Volcanics

Table 1.--Continued

CODE	LOCATION	TYPE	LAT	LONG	ELEV (M)	VAULT TYPE	DEPTH (M)	GEOLOGY
LON	Longmire, Washington, USA	DWWSSN	46.75N	121.81W	854	Surface		Volcanics
LSA	Lhasa, Tibet, China	CDSN	29.70N	91.15E	3789	Subsurface	15	Granite
LZH	Lanzhou, Gansu Province, China	CDSN	36.09N	103.84E	1560	Surface -BB/VLP Borehole-SP/LP	120	Loess Sandstone
MAIO	Mashad, Iran	SRO	36.30N	59.49E	1000	Borehole	100	Igneous
MAJO	Matsushiro, Japan	IRIS-2	36.54N	138.21E	422	Subsurface	48	Quartz Diorite
MDJ	Mudanjiang, China	CDSN	44.62N	129.59E	250	Subsurface	50	Granite
NNA	Nana, Peru	IRIS/IDA	11.99S	76.84W	575	Subsurface	30	Granite
NVS	Novosibirsk, Russian Federation	IRIS/IDA	54.84N	83.23E	150	Surface		Phyllite
NWAO	Narrogin, Australia	IRIS-2	32.93S	117.24E	265	Borehole	100	Granite
OBN	Obninsk, Russian Federation	IRIS/IDA	55.11N	36.57E	160	Subsurface	30	Limestone
PAB	San Pablo, Spain	IRIS-2	39.54N	4.35W	925	Subsurface	3	Granite
PAS	Pasadena, California, USA	TERRA	34.15N	118.17W	295	Surface		Quartz Diorite
PFO	Pinon Flat, California, USA	TERRA	33.61N	116.46W	1280	Subsurface	3	Granite
QIZ	Qiongshong, Quangduong Prov., China	CDSN	19.03N	109.84E	230	Surface		Granite
RAR	Rarotonga, Cook Islands	IRIS-2	21.21S	159.77W	28	Borehole	100	Basalt
RPN	Rapanui, Easter Island, Chile	IRIS/IDA	27.13S	109.33W	110	Surface		Basalt
RSCP	Cumberland Plateau, Tennessee, USA	RSTN	35.60N	85.59W	485	Borehole	100	Shale/limestone
RSNT	Yellowknife, NWT, Canada	RSTN	62.48N	114.59W	-50	Borehole	100	Slate
RSNY	Adirondak, New York, USA	RSTN	44.55N	74.53W	357	Borehole	100	Gneiss

Table 1.--Continued

CODE	LOCATION	TYPE	LAT.	LONG.	ELEV (M)	VAULT TYPE	DEPTH (M)	GEOLOGY
RSON	Red Lake, Ontario, Canada	RSTN	50.86N	93.70W	221	Borehole	103	Granite
RSSD	Black Hills, South Dakota, USA	RSTN	44.12N	104.04W	1950	Borehole	110	Limestone
SBC	Santa Barbara, California, USA	TERRA	34.44N	119.71W	90	Surface		Alluvium
SCP	State College, Pennsylvania, USA	DWWSSN	40.79N	77.87W	352	Surface		Limestone
SHIO	Shillong, India	SRO	25.57N	91.88E	1509	Borehole	91	Quartzite
SLR	Silverton, South Africa	DWWSSN	25.73S	28.28E	1348	Surface		Quartzite
SNZO	South Karori, New Zealand	IRIS-2	41.31S	174.70E	-12	Borehole	100	Graywacke
SPA	South Pole, Antarctica	IRIS-2	89.98S	0.0	2927	Subsurface	4	Snow and Ice
SSE	Shanghai, China	CDSN	31.10N	121.19E	10	Surface		Andesite
SUR	Sutherland, South Africa	IRIS/IDA	32.38S	20.81E	1770	Surface		
SVD	Seven Oaks Dam, California, USA	TERRA	34.10N	117.10W	600	Surface		Quat. Alluvium
TATO	Taipei, Taiwan	IRIS-2	24.97N	121.49E	53	Borehole	90	Sandstone/shale
TAU	Hobart, Tasmania	DWWSSN	42.91S	147.32E	132	Subsurface	7	Dolerite
TLY	Talaya, Russian Federation	IRIS/IDA	51.68N	103.64E	579	Subsurface		Granitic
TOL	Toledo, Spain	IRIS-2	39.88N	4.05W	480	Surface		Alluvium
TUC	Tucson, Arizona, USA	IRIS-2	32.31N	110.78W	874			Granite
WMQ	Urumqi, Xinjiang Province, China	CDSN	43.82N	87.70E	970	Subsurface	6	Sandstone
YSS	Yuzhno-Sakhalinsk, Russian Federation	IRIS-2	46.95N	142.75E	100	Subsurface	3	Schist
ZOBO	Zongo Valley, Bolivia	ASRO	16.27S	68.13W	4450	Subsurface	300	Granodiorite

Table 1.--Continued

Definition of Data Bands

Most data acquisition systems are designed to record seismic data in two or more frequency bands. The major purpose of separating recording bands in the past was to suppress the recording of microseisms; today, it is done mostly as a matter of the convenience for the data user. In this report the recording bands are defined by sampling rate. The SP20, SP40, SP80, and SP100 bands are short-period channels with sampling rates of 20, 40, 80, and 100 samples per sec, respectively. BB and VBB are broadband and very broadband channels sampled at 20 samples per sec. The distinction between the BB and VBB bands in this report lies in the bandwidth of the seismometer to an input of Earth velocity -- from 0.2 to 20 sec period in the case of the BB channels and 0.2 to 360 sec period in the case of the VBB channels. MP is a mid-period band with a sampling rate of 5 samples per sec. LP (long period), VLP (very long period), and ULP (ultra long period) bands have sampling rates of 1.0, 0.1, and 0.01 samples per sec, respectively.

In general, the VBB, MP, LP, VLP, and ULP signals are recorded continuously, while the BB and SP signals are recorded only when triggered by a signal that exceeds a preset or programmable threshold. Most of the data acquisition systems record three orthogonal components (vertical, north, and east), but there are a few exceptions in which only vertical components are recorded.

Data Systems

The digital data used in this study were generated by a variety of data acquisition systems representing technology that has evolved steadily over the past twenty years. Only a brief description of the data systems is needed here because most are well documented in the references provided.

SRO Systems

The Seismic Research Observatories (SRO) were developed and deployed in the mid 1970s. The most innovative feature of the SRO system was the KS-36000 borehole sensor system which was developed by Teledyne-Geotech, Inc. primarily for the purpose of improving the quality and consistency of long-period data. The KS-36000 sensor systems contain force-balance accelerometers that are encased in small evacuated modules. The accelerometers produce signals that are flat to Earth acceleration from about 1 to 50 sec period. Electronics located at the surface split the three-component broadband signals into SP20 and LP bands for digital encoding and recording. The LP signals are recorded continuously, the SP20 signals are recorded only when triggered by a signal detector. The borehole seismometers are installed in cased and cemented boreholes, normally at a depth of about 100 m. In operation, the three component signals have about the same level of noise power, and the horizontal components are not affected significantly by surface winds. More details on the SRO

system, including its testing and calibration, can be found in a report by Peterson and others (1980).

ASRO Systems

The ASRO data systems are updated versions of the High-Gain Long-Period (HGLP) seismographs installed in the early 1970s by the Lamont-Doherty Geological Observatory (LDGO) and the Albuquerque Seismological Laboratory. The HGLP systems, described by Pomeroy and others (1969), employed conventional long-period seismometers (Teledyne-Geotech Models S11 and S12) operated at periods of 30 sec, together with phototube amplifiers, photographic recorders, analog-to-digital converters, and a digital tape recorder. Only long-period data channels were recorded. LDGO developed special installation techniques using sealed tanks and vaults to isolate the seismometers from environmental noise sources, permitting a much higher operating magnification than earlier LP systems. Five of the original HGLP systems were modified later by adding solid-state amplifiers, Teledyne-Geotech Model JM-6480 1-sec seismometers, and SRO-type recording systems, and the period of the long-period seismometers was reduced to 20 sec. The modified HGLP systems were then called ASRO systems. Only the ZOBO ASRO system is still in operation, and this will soon be replaced by new instrumentation.

DWWSSN Systems

In the early 1980s, digital recorders were installed at 15 World-Wide Standardized Seismograph Network (WWSSN) stations. The objective of this program was to expand the global digital network at relatively low cost by attaching amplifiers and digital recorders to the existing WWSSN seismometers (Geotech Model 1051 "Benioff" short-period seismometers and Sprengnether Models 201 and 100 long-period seismometers). The program met with only partial success because of long-period instrument noise. A complete description of the digital WWSSN (DWWSSN) system, including its test and calibration, is provided in a report by Peterson and Hutt (1982). Five of the DWWSSN systems (at AFI, COL, CTAO, KEV, and TOL) were equipped with Streckeisen STS-1/VBB seismometers in the late 1980s, and three of these have since been upgraded to IRIS-type systems. The DWWSSN system originally installed at Jamestown, California and since moved to CMB is equipped with Teledyne-Geotech GS-13 short-period seismometers and Guralp CMG3 broadband seismometers.

CDSN Systems

During the mid 1980s, the USGS, the State Seismological Bureau of China (SSB), and DARPA cooperated in the development and deployment of a network of nine digital data acquisition systems in China. A tenth station (LSA) was installed in 1991. The China Digital Seismograph Network (CDSN) was equipped with broadband Streckeisen STS-1 seismometers and DJ-1 short-period seismometers of Chinese

manufacture. The STS-1 force-balance seismometers have an output flat to velocity from a period of 0.2 sec to 20 sec and generate separate BB and LP signals for recording. The LP signals and derivative VLP signals are recorded continuously. BB signals are recorded at low gain only when triggered by an event detector. The DJ-1 electromagnetic seismometers generate the higher gain SP40 signals that are recorded only when triggered. The LZH station is an exception; it is equipped with a KS-36000 borehole seismometer installed at 120 m that is used to produce LP and SP40 signals at that site. The BJI station is equipped with a borehole seismometer containing a triaxial set of DJ-1 seismometers. The test and calibration of the CDSN sensor systems has been reported by Peterson and Tilgner (1985). A description of the CDSN stations, including noise spectra, is provided in a Joint Report (1987) by the Institute of Geophysics, State Seismological Bureau and the Albuquerque Seismological Laboratory.

IRIS/USGS Systems

In 1987 the IRIS Consortium and the USGS began development of new broadband data acquisition systems. The USGS based its version of the new IRIS system on a very broadband data acquisition system conceived and developed at Harvard University by J.M. Steim (1986). The Steckeisen STS-1/VBB seismometers used in this application have a velocity response extended from 20 sec to 360 sec period, and 24-bit digital encoders were used for the first time to greatly increase the recording range of the seismograph system.

IRIS-1 systems used at several of the network stations are essentially copies of the Harvard system. They record continuous VBB, LP, VLP, and ULP signals. The LP, VLP, and ULP signals are derived from the VBB signals via digital filtration and decimation.

The IRIS-2 systems currently being deployed by the USGS are similar to the IRIS-1 systems, but have many additional features including optional short-period seismometers sampled at a rate of 80 or 100 samples per sec. Teledyne-Geotech GS-13 seismometers are most often used for short-period data acquisition. Many of the SRO systems have been converted to IRIS-2 systems. A modified version of the KS-36000 borehole seismometer is operated at these stations in place of the STS-1/VBB seismometers in order to retain the advantages of borehole operation. The modified seismometer, designated KS-36000I, has been redesigned by Teledyne-Geotech to produce a velocity response with essentially the same bandwidth and gain characteristics of the STS-1/VBB seismometer. A description of the IRIS-2 system is included in a report on the joint IRIS-USGS program by Peterson and Hutt (1992).

IRIS/IDA Systems

In a parallel program, UCSD and the IRIS Consortium have upgraded the International Deployment of Accelerometers (IDA) network and developed new data systems that are currently being deployed. The IDA network, described by Agnew

and others (1976), was established in the mid 1970s by UCSD as a global array of LaCoste-Romberg gravimeters for recording very long-period data. Most of these stations have now been equipped with Streckeisen STS-1/VBB seismometers and new recording systems. The VBB signals (or MP signals in the case of ESK or NNA) are recorded continuously and have generally the same response characteristics as the other IRIS-type systems. The most recent version of the IRIS/IDA system, called the IRIS-3 system and described by Given and others (1992), has expanded recording options, 24-bit digital encoders, and other new features. Triggered short-period signals are recorded at the AAK, NVS, and TLY stations and at other more recently installed IRIS/IDA stations. However, the triggered data were not used in this study.

RSTN Systems

The five-station RSTN was deployed in the early 1980s by Sandia National Laboratories as a test and demonstration of a regional monitoring network that could be used within the context of a test ban monitoring program. The RSTN data systems developed at SNL were equipped with KS-36000-04 borehole seismometers, a modified version of the original KS-36000, and a separate borehole package containing a three-component set of Teledyne-Geotech S-750 short-period seismometers. The KS-36000-04 seismometer produced three signals, SP40, MP, and LP, that are digitized separately, then transmitted via satellite to a recording system, together with digital SP40 signals from the S-750 accelerometers. All data bands were recorded continuously and archived at SNL. However, the archived short-period signals have been processed through an event detector and only SP events are stored in the ASL archive. The RSTN data available in the ASL archive spans a time period from about December 1982 to October 1986. A detailed description of the RSTN and RSTN data is provided in a report by Breding (1983).

TERRAscope Systems

TERRAscope is a broadband seismograph network deployed in southern California by the California Institute of Technology in cooperation with other organizations (Kanamori and others, 1991). All of the TERRAscope stations used in this study except SVD are equipped with Streckeisen STS-1/VBB seismometers; SVD is equipped with a Streckeisen STS-2 broadband sensor system. The data bands and data formats used in the TERRAscope network are similar to those used in the IRIS-1 and IRIS-2 systems.

DATA PREPARATION

Data Selection

The selection of data records used in this study took place over several years, which accounts for the fact that some of the noise spectra for stations currently in operation are two or three years old. The quest has not been to find the quietest data record at the quietest site or noisiest data record at the noisiest site, but to select representative values of noise during quiet and noisy periods at the network stations. In fact, the background noise during quiet intervals at most stations for periods outside the principal microseismic band (1 - 20 sec) is remarkably consistent over the periods examined. The important tasks in data collection were to avoid seismic events and other transient phenomena and examine a sufficient number of time intervals to insure consistency in the data records chosen for final processing.

Although there are a few exceptions, the basic data record length used in this study is 8,192 (8K) samples, an array of long integers that can be handled comfortably in a personal computer. The equivalent recording times range from 81.92 sec for the SP100 band to 9.48 days for the ULP band.

A survey of station noise almost always began with the selection of LP data records because it was most difficult to find concurrent 2.3-hour data records from all three components unaffected by events, noise bursts, or a significant change in noise characteristics. LP signals were plotted as 24-hour seismograms for 3 or 4 quiet days, and the seismograms were visually scanned for small events and noise bursts or other types of instrumental problems. Noise spectra were computed at two-hour intervals over the quietest 24-hour seismograms. The three quietest of the LP time series were then retained for final processing. At most stations there is very little variation in the quiet LP noise spectra on a day-to-day or seasonal basis except in the microseismic band.

The IRIS/IDA stations that were used in this study did not have separately recorded LP data channels. In order to present station spectra for the standard LP band, LP data records were derived from the IRIS/IDA MP or VBB time series by first filtering the signals using a 10-pole Butterworth low-pass filter cornered at 8 sec period and then decimating to 1 sample per sec.

VBB data records were generally taken from the same 24-hour periods that yielded the quietest LP data records. VBB noise spectra were computed at the beginning of each hour of the day. The three quietest records were then selected for processing. The selection was based on the background noise power at periods shorter than 1 sec. The amplitude of microseismic noise in the mid-period band was not one of the selection criteria unless it appeared to be much higher than normal, in which case the record was not selected. Where the daily cycle produced significant (6 dB or greater) variation between quiet and noisy records of data, three of the noisy records were also selected for processing.

The selection of triggered BB and SP data records presented more of a problem,

except in those cases where continuous test data were available. Continuous 24-hour recordings of SP40 and BB signals were made at the CDSN stations as part of the installation testing, and this procedure is also being followed at the IRIS/USGS stations where optional SP channels are recorded. Where continuously recorded SP and BB test data were available, the procedures used for selecting data records were similar to those described above for the VBB data channels, although the time span available in these cases was usually limited to one or two contiguous days. The SRO systems were designed with an automated calibration program that included the continuous recording of SP data for a 15-minute duration once each month. The disadvantage in using these segments is that all of the available data are from the same time of day.

In the cases where only triggered data are available in the archive, the database was searched for records triggered by step calibration pulses or noise spikes. This method was used primarily with the RSTN data. The data records were generally shorter than 8K in length, and it was not always possible to achieve as good a comparison of day/night noise differences.

Altogether, about 12,000 data records were reviewed and just under 2,000 were retained for final processing. The selection of data could be automated with better data retrieval facilities than are available at ASL where the emphasis is on bulk data transfers rather than the extraction of small data records.

Data Processing

The computation of power spectral density (PSD) estimates for this report has generally followed recipes provided by Bendat and Piersol (1971) or Otnes and Enochson (1972). Both ensemble and frequency smoothing were used to reduce the variance of the estimates. Spectral estimates for each 8K data record were obtained by averaging the PSD estimates computed from 12 overlapping segments derived from the data record. The segments overlapped by 75%. The mean value and slope were removed from each segment, a Hanning taper was applied, and a spectral estimate was computed using a fast Fourier transform algorithm adapted from Stearns (1975). The 12 estimates were then averaged, and the instrument response (except digital filter response) was removed from the result. The ensemble averaging provides 24 degrees of freedom giving a 95% level of confidence that the spectral point lies within -2.14 dB to +2.87 dB of the estimate. PSD estimates computed from three independent data records were then averaged to broaden the sample base, and finally a five-point frequency smoothing was applied. In a few cases where only short triggered record lengths are available, four-segment ensemble averaging was used, and in some cases less than three independent records were averaged. In removing the instrument response, the spectral power has been referred to a seismometer input of Earth acceleration.

The ULP data were processed differently. The ULP 8K data records are 9.48 days in length. Only one data record was chosen for each station, and in order to preserve sufficient bandwidth to present the Earth tide spectral components, the PSD

estimate was computed from the 8K data record without ensemble averaging. The ULP PSD estimates were then smoothed using a frequency domain "supersmoothing" algorithm originated by Holcomb (1989) that constructs a least-squares fit of the estimate using a decreasing number of adjacent data points for fitting as the period increases.

STATION NOISE SPECTRA

Presentation of Station Data

Station noise spectra are presented in Figures A1 through A88 of the Appendix. The information in the upper left corner of the plots includes the station code, the type of data system, and for each separate recording band, the seismometer and the Julian day or days from which the independent data records were obtained. The spectra are presented in units of decibels referred to 1 $(m/sec^2)^2/Hz$ as a function of period. Plotted together with the station noise spectra are dashed curves representing the low- and high-noise models.

To avoid excessive overlap, the SP, BB, and VBB spectra are plotted only to a period of about 10 sec. The LP spectra are plotted beginning at a period of 10 sec, and the ULP spectra are plotted beginning at a period of 1000 sec. At stations where both BB or VBB and SP channels are recorded, the SP spectra are plotted in a separate figure.

At stations where there is at least a 6 dB daily variation in noise level, both noisy and quiet spectra are plotted for the SP, BB, or VBB data bands. In a few cases, both noisy and quiet LP data bands are plotted. Except as noted in the figure captions, quiet spectra are derived from nighttime data records and noisy spectra from daytime data records. Actual time of day varies from station to station.

A few anomalous characteristics of the plots are worth noting. Because the digital filter transfer functions were not deconvolved from the noise spectra at stations with digital low-pass filters, the spectra from these stations show a very steep rolloff between the filter corner period and the Nyquist period (see Figure A17, for example). At stations where analog low-pass filters are used to prevent aliasing, the noise spectra may rise sharply between the filter corner period and the Nyquist period. This occurs when the seismometer gain is insufficient to raise the seismic background signal above least-count digitizer noise, which is generally flat before deconvolution of the transfer function and shaped to the inverse low-pass filter response following deconvolution. See the Hailar noise spectra (Figure A32 and A33), for example. This effect can also be found in LP spectra on the long-period side (see the RSTN LP spectra, for example).

Spectral Overlay

Most of the noise spectra shown in the Appendix, for both quiet and noisy time periods, are plotted together in Figure 2. The DWWSSN LP spectra and the RSTN LP

spectra at periods longer than 1000 sec have not been included in the overlay, and the SP, BB, and VBB spectra have been edited at short periods to exclude the effects of the analog and digital anti-aliasing filters described above.

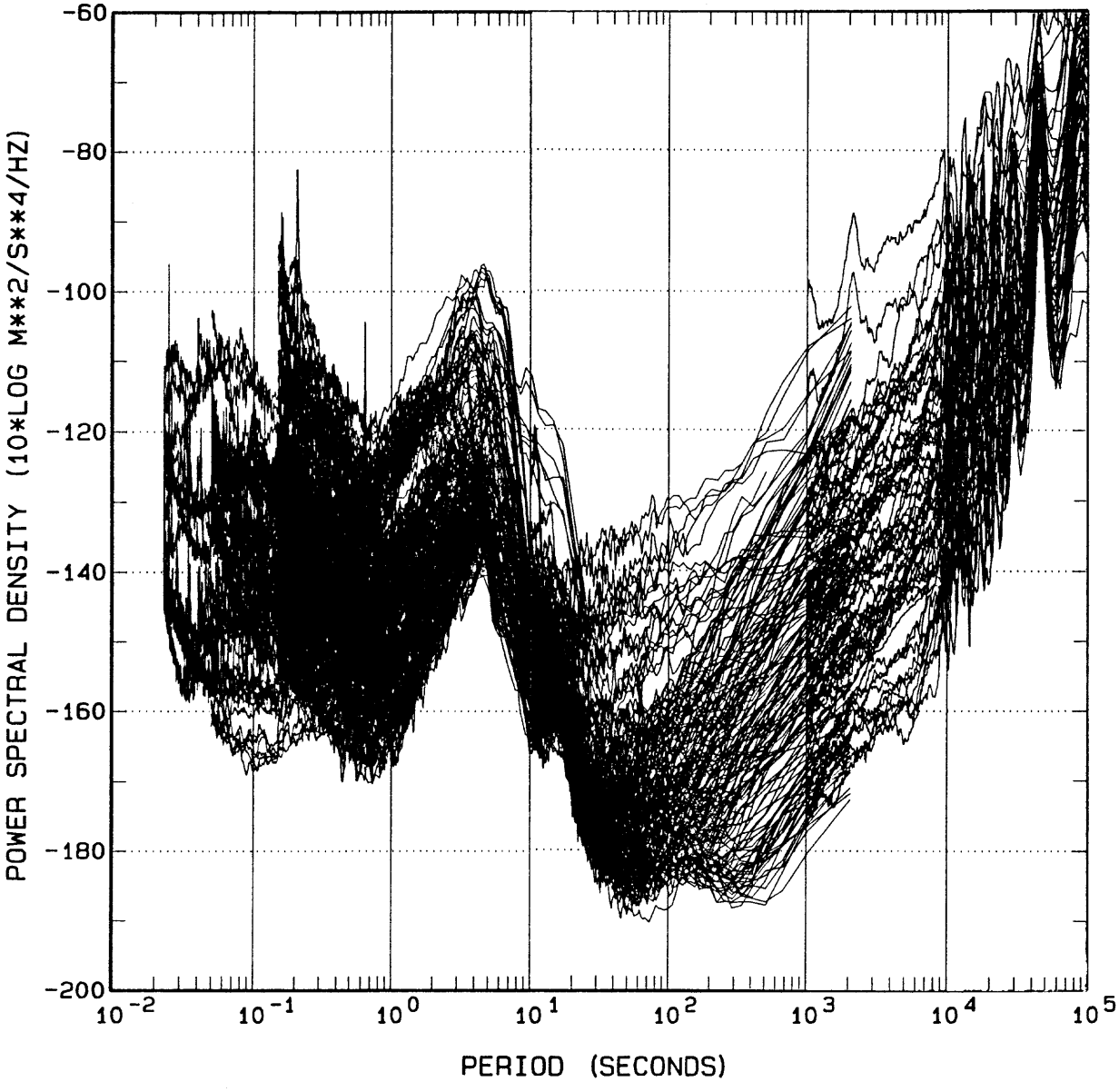

Figure 2.--An overlay of most station spectra presented in the Appendix. Not included are the DWWSSN LP spectra and RSTN LP spectra at periods longer than 1000 sec.

Major structural features of Earth noise are revealed by the overlay, the most dominant features being the natural microseisms in the period range from about 1 to 20 sec with peaks at 5 sec and 18 sec, and the Earth tides with peaks at semi-diurnal and diurnal periods. The rounded low-noise peak in the long-period band at a period of about 120 sec appears to be a real and significant noise feature, its cause unknown.

However, the domelike noise peak at about 0.3 sec period is shaped by two different sets of instruments and probably exists as the result of insufficient gain in the STS seismometers to resolve quiet Earth noise at that period.

The trace overlays also demonstrate the dynamic range needed for broadband recording -- at least 90 dB in the 1 to 100 sec period band simply to accommodate background noise. Island stations, such as KIP, may have both a very high level of microseismic noise and a low level of long-period noise. The situation is worse during intense microseismic storms, which were excluded from this study.

Non-Seismic Noise

How much of the lower envelope of the overlay in Figure 2 is a true representation of Earth background noise, and how much of it is shaped by instrument noise? Most of the spectral data that shape the low-noise envelope of the overlay at periods longer than 1 sec are derived from the STS-1 seismometers. Tests were conducted at ASL using two STS-1/VBB vertical-component seismometers operating side by side. Signals recorded from the two sensors were normalized to a uniform gain, the mean value of each signal was removed, and a difference (error) signal was derived by subtracting one signal from the other. The PSD was then computed for each of the parallel data sets and the difference signal. The difference signal is the sum of self noise in the two seismometers plus any errors due to differences in transfer functions, either amplitude or phase, coupling to the Earth, or vertical misalignment. Therefore, it is not a measurement of self-noise power but represents an upper limit to the sum of independent self noise generated by the two instruments.

The results of the tests are shown in Figure 3 in which the PSD estimates of the two test signals and the difference signal are plotted after being corrected for instrument response. The difference signal spectra mimics the shape of the test signal spectra in the microseismic band at least partly because of a small percentage error in normalizing the gains of the two signals. A 40 dB spread between the test signals and difference signal represents an error of 1% in gain.

Between periods of 1 sec and about 6,000 sec, the difference noise power is significantly lower than the test signal noise power. At periods above 6,000 sec, the difference signal power is slightly below the test signal power even though the sensor gain is decreasing at a rate of 40 dB per decade in this band. This test demonstrates that the STS-1 vertical-component seismometers are capable of resolving Earth noise at the quietest sites in the network at periods of 1 sec and longer.

At periods shorter than 1 sec, the test signals and the difference signal have approximately the same power indicating that the two test signals are partially incoherent and generated largely by non-seismic sources. Figure 4 shows the test data together with measured digitizer noise that has been referenced to an input of Earth acceleration using the IRIS-2 STS-1/VBB transfer function. The system noise is greater than the digitizer noise, indicating that the major contributor of non-coherent noise at short periods is the seismometer. Comparable STS-1 short-period noise was

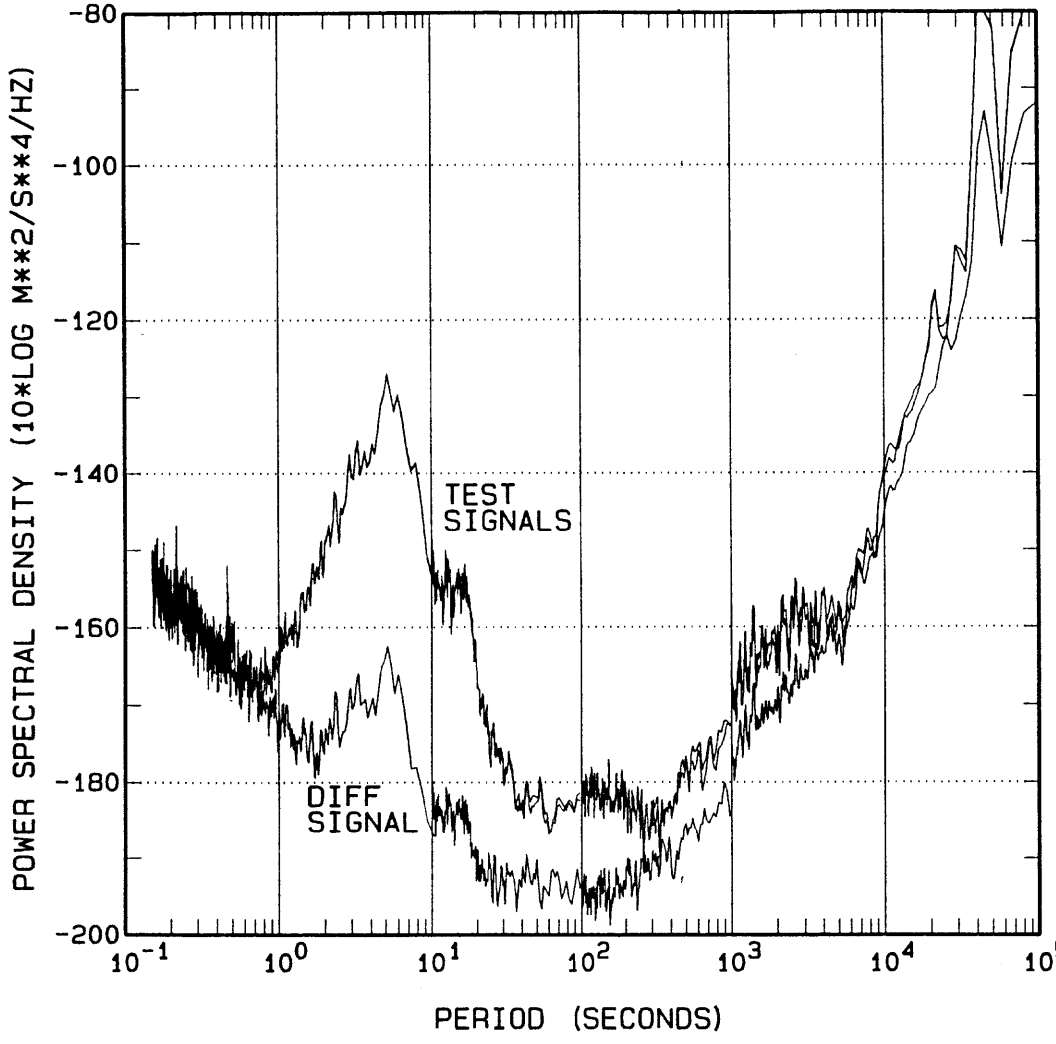

Figure 3.--Spectra computed from two vertical-component STS-1 test signals and their difference signal, all referred to an input of Earth acceleration. The test signals were recorded during a quiet (non-event) period in the ASL subsurface vault, one of the quietest vaults in the network. Test data were provided by C.R. Hutt.

measured by Steim (1986, Figure 4.1.22).

Non-seismic noise in the KS-36000 seismometer was measured in earlier tests (see Peterson and others, 1980). The testing in the long-period band revealed that non-coherent noise power reached the level of coherent noise power at periods between 60 and 100 sec and became the dominant noise power at periods longer than 100 sec. The modified versions of the KS-36000 seismometers used in the IRIS/USGS network are expected to have similar long-period noise characteristics. Short-period digitizer noise was negligible because of the high gains used in the SRO short-period

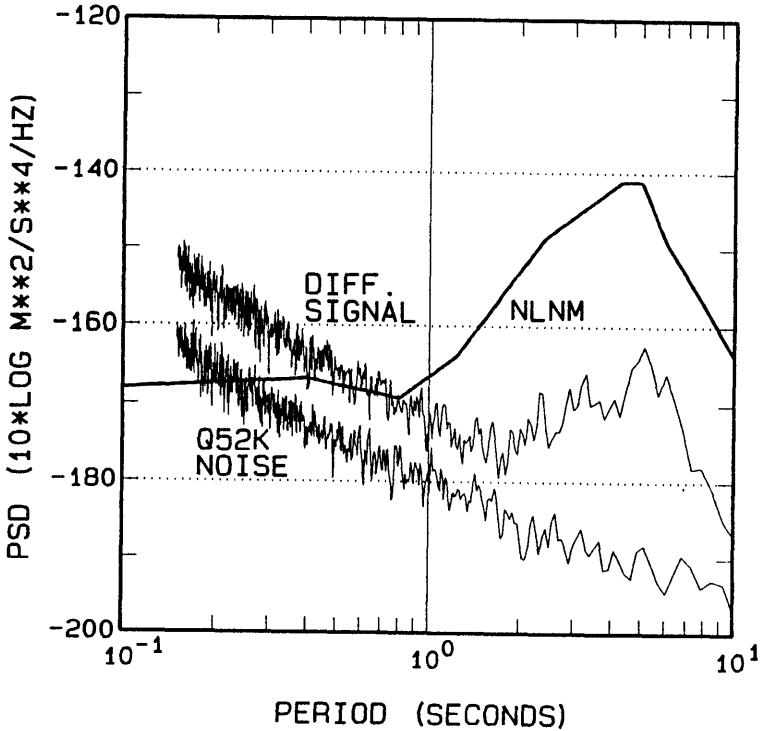

Figure 4.--Comparison of spectra computed from the difference signal and one of the Q52K digitizers used in the difference test. The digitizer had a shorted input to measure the digitizer noise, and the spectra were corrected for instrument response using the STS-1/VBB transfer function. The new low-noise model (NLNM) is also shown in the figure.

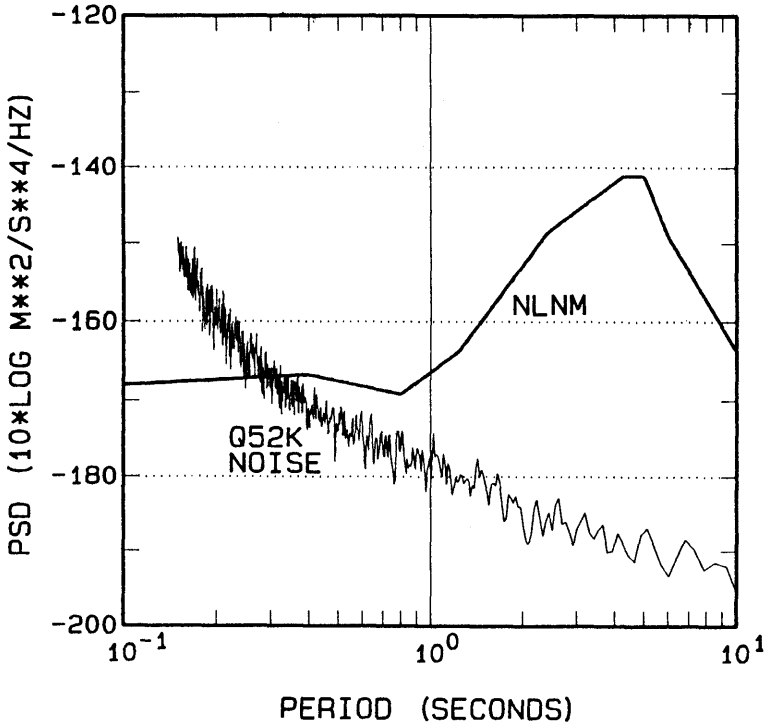

Figure 5.--Digitizer noise spectra. In this case, the spectra were corrected for instrument response using the KS36000I transfer function.

band. However, the gain at short periods was reduced significantly during the modification of the KS-36000 seismometer such that digitizer noise now limits resolution of Earth background at quiet sites. Figure 5 shows a plot of digitizer noise power referenced to an input of Earth acceleration as it would appear in an IRIS-2 system with a KS-36000I seismometer. Clearly, the IRIS systems using the KS-36000I seismometer have the same limitations in resolving background at quiet sites as the IRIS systems with the STS-1 seismometers.

In Figures 4 and 5 the digitizer noise appears high relative to background noise at a quiet site, not because of a problem with the digitizers, but because the seismometer gain is too low to resolve the background signal. Indeed, the measured RMS (root-mean-square) noise in the Quanterra Q52K digitizer over the 8,192 sample record was only 0.664 counts. Although the SP recording might be improved by boosting the gain of the broadband seismometers, this would have the great disadvantage of lowering the clipping threshold for large earthquakes. Clearly, at quiet sites, separate short-period seismometers, such as the GS-13, should be used with the gain set high enough to overcome digitizer noise throughout the band of interest. Fortunately, the IRIS systems include an option for adding short-period seismometers.

Short-Period Seismic Noise

Seismic background noise at periods below 1 second is highly variable across the network. At continental sites the background noise appears to be primarily cultural in origin, varying, as it does at many stations, on an almost hourly basis. At island and coastal sites, such as KIP or GUMO, natural microseisms have a much broader bandwidth and the dominant noise below 1 sec period is microseismic in origin, sometimes modulated by cultural noise, as again in the cases of KIP and GUMO.

A listing of the stations used in this study, sorted by short-period noise amplitude in a specific band, is provided in Table 2. The numbers in the table represent the RMS noise in decibels in excess of the RMS noise computed from the low-noise model (-168.36 dB referred to 1.0 m/sec/sec). The RMS noise was computed over a 1-octave band centered on a period of 0.8 sec. The center period of 0.8 sec was chosen because at continental sites there appears to be a modest low-noise window at that period for teleseismic P waves, and because it avoids the short-period band of insensitivity of the broadband seismometers. For the stations listed, both the average and median values of short-period noise are about 22 dB above the noise model.

The network of stations used in this study is not well suited for the detection of small events, even when considering only continental stations. Indeed, many mid-continent stations that one would expect to be quiet have above average short-period noise. Part of the problem is that some of the data systems have limited resolution in the short-period band, but mainly it is because the stations are poorly sited and lack sufficient isolation from local cultural noise. The majority of station vaults were constructed in relatively isolated locations nearly 30 years ago as the WWSSN was being deployed. Since then, many of the stations have become small scientific

outposts in a jungle of factories, shops, and high-rise apartment buildings.

STATION	BAND	Z	N	E	STATION	BAND	Z	N	E
ANMO	SP	2.17	1.09	0.99	GRFO	SP	21.85		
MAIO	SP	2.65			TOL	VBB	21.87	24.52	24.28
KAAO	SP	5.51			SSE	BB	22.59	21.91	22.07
LSA	SP	6.36	5.40	4.70	NNA	MP	23.12	22.31	22.85
BCAO	SP	8.75			ARU	VBB	23.27	17.50	14.55
ENH	SP	9.65	9.13	10.99	GNI	VBB	23.33	27.46	27.19
TUC	VBB	9.77	7.78	7.41	CTAO	VBB	23.38	22.51	22.42
GSC	VBB	9.88	12.21	12.16	QIZ	BB	23.74	21.70	21.06
RSNT	SP	10.27	9.94	10.73	MDJ	BB	23.79	25.49	27.47
COL	VBB	10.57	11.56	11.07	YSS	VBB	24.40	26.72	27.26
RSSD	SP	10.85	14.32	12.99	TLY	VBB	24.74	24.55	25.53
SPA	VBB	11.08	7.08	7.10	COR	VBB	25.06	25.02	25.05
GAR	VBB	11.34	12.30	10.16	ESK	MP	25.07	26.12	19.91
SHIO	SP	11.45			LZH	SP	25.96		
ZOBO	SP	11.52			NWAO	VBB	26.28	25.26	24.94
HIA	BB	11.82	12.15	12.63	PAS	VBB	27.28	25.91	26.99
CHTO	SP	12.48			KEV	SP	27.45		
ISA	VBB	12.70	12.89	13.20	SUR	VBB	27.91	28.47	27.24
CMB	SP	13.43			ANTO	SP	29.03		
AAK	VBB	13.85	14.35	14.06	HRV	VBB	30.98	30.29	30.18
CCN	VBB	13.89	15.72	13.78	BOCO	SP	31.70		
RSCP	SP	14.85	21.93	21.82	SVD	VBB	32.49	29.70	27.84
KONO	VBB	14.93	12.31	14.19	TAU	SP	32.67		
ALE	VBB	15.29	14.62	15.24	OBN	VBB	34.29	43.43	41.58
NVS	VBB	16.96	15.96	18.47	LEM	SP	35.53		
RSNY	SP	17.20	15.49	17.27	KIP	VBB	36.04	37.82	37.73
PFO	VBB	17.54	14.83	14.55	KIV	VBB	36.17	46.48	41.79
KMI	SP	18.56	20.62	21.61	RAR	VBB	38.24	37.63	37.45
WMQ	SP	18.59	15.65	13.76	AFI	SP	40.02		
BJI	SP	19.26	16.64	15.13	GUMO	VBB	40.42	41.49	39.75
RSON	SP	19.46	20.67	18.26	GDH	SP	41.27		
LON	SP	19.79			TATO	VBB	41.39	40.43	37.63
SLR	SP	20.08			SNZO	VBB	41.87	41.70	40.56
SCP	SP	20.30	21.20	17.54	ERM	VBB	42.33	43.11	41.53
MAJO	VBB	20.65	21.90	19.92	SBC	VBB	43.96	44.65	44.55
BDF	SP	21.43			RPN	VBB	46.28	44.15	45.11
PAB	VBB	21.70	21.91	21.32					

Table 2.--Stations listed by increasing RMS noise in the 1-octave band centered on 0.8 sec. The amplitudes listed are decibels in excess of LNM RMS noise in that band.

Because it is expensive to move the seismograph stations to remote areas and difficult to staff them, the best solution is to deploy satellite short-period seismometers at remote sites with data telemetered back to the station or other collection points. In addition, boreholes for short-period seismometers can decrease background noise at stations situated on alluvial deposits if the seismometers can be placed below the alluvium in hard rock, as clearly demonstrated by a comparison of the SP40 (borehole) and BB (vault) station data at BJI and LZH (Figures A11 and A12, A48 and A49, respectively).

Cultural noise can generally be distinguished from natural microseisms by its day/night pattern. A large diurnal variation in station background noise would indicate that significant improvements could be made by relocating short-period instruments to a more isolated site. The variations of background noise over a 24-hour period are shown in Figure 6 for the stations where continuous SP, BB, or VBB data are recorded. Noise spectra were computed for data records at the beginning of each hour, and RMS values were computed from the spectra over the band from 0.2 to 1 sec. The differences in decibels between each hourly segment and the lowest noise segment of the 24-hour period are plotted as a function of local time for the day specified. The amplitude range is 20 dB for all station plots except for ARU, GSC and ISA. The time series were not visually scanned in all cases, so anomalous points may be earthquakes or unusual noise bursts. Data from coastal and island stations, such as ERM and RPN, or stations near lakes, such as TLY, may be affected more by surf than cultural noise. The plots in Figure 6 were derived from a limited data set and are intended only as illustrations of noise variation at the individual stations. Some of the stations would clearly benefit by being moved to sites perhaps not too distant, a good example being the station COL at College, Alaska where there is good rock and many options for remote sites. The plots in Figure 6 also demonstrate that stations with significant diurnal variation in noise are not well defined by an average noise curve because the transition between low and high background noise can be abrupt, and, in these cases, an average noise curve would be inaccurate most of the time.

Long-Period Seismic Noise

There is as much or more background noise variability in the long-period band (periods longer than 10 sec) as in the short-period band, but mostly in the horizontal components. The long-period vertical-component background signals are relatively stable as a function of time. Reports by Sorrells (1971) and Sorrells and others (1971) have attributed long-period noise to Earth motion caused by local fluctuations in the atmospheric pressure field. Although pressure change causes both vertical and horizontal displacements, Sorrells (1971) showed that the associated tilt is the principal source of noise in the horizontal components, and the development of the KS-36000 borehole seismometer followed his prediction that the deformation associated with pressure change would be rapidly attenuated in hard rock.

Deployment of the KS-series seismometers helped to significantly improve the long-period data base. Nevertheless, there are some important tradeoffs between

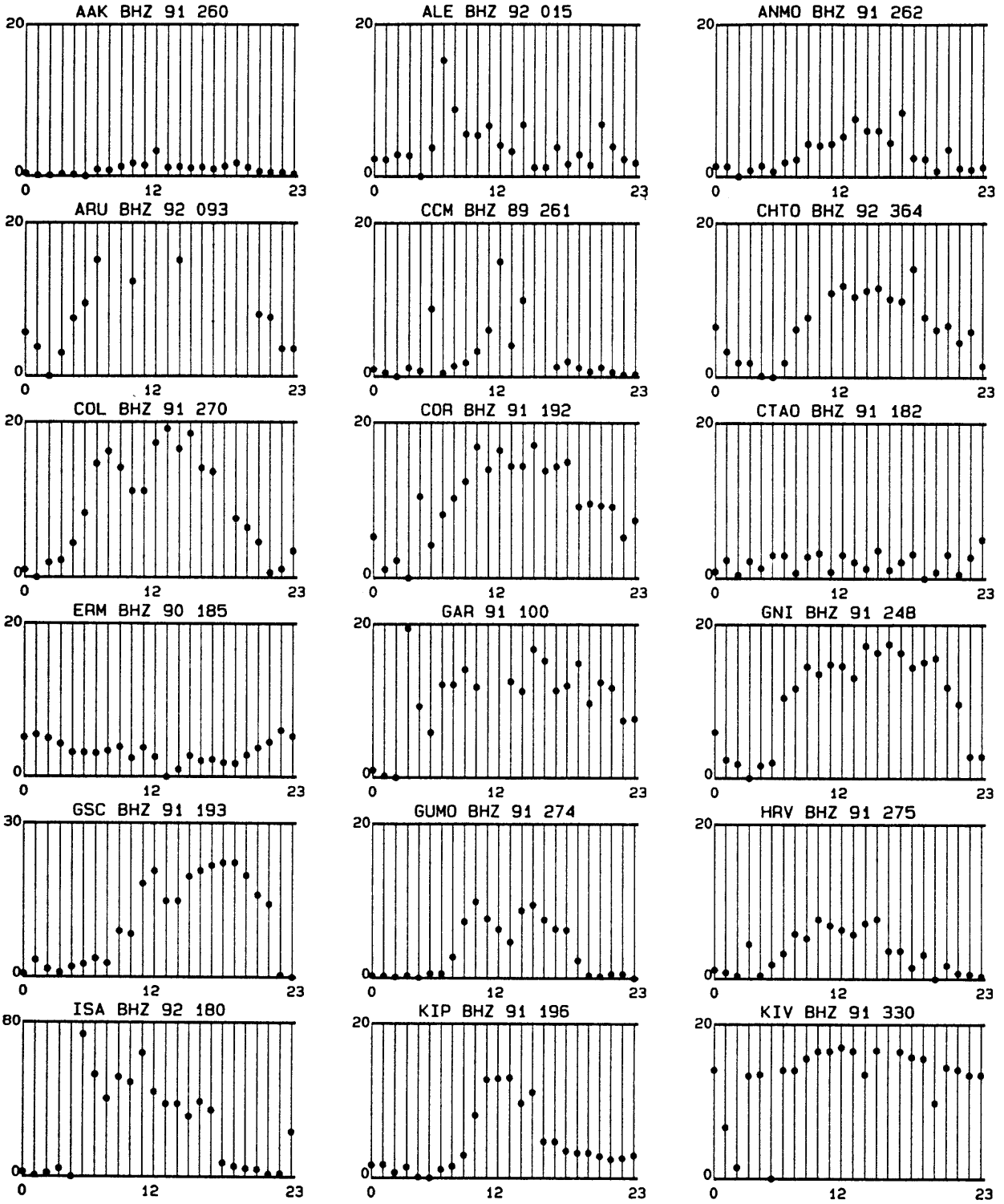

Figure 6.--Individual station plots showing the daily variation of short-period VBB noise. The days analyzed are listed next to the station codes. The time scale is referenced to local time, each point taken at the beginning of the hour. The amplitude scale is in dB referred to the amplitude of the lowest noise segment.

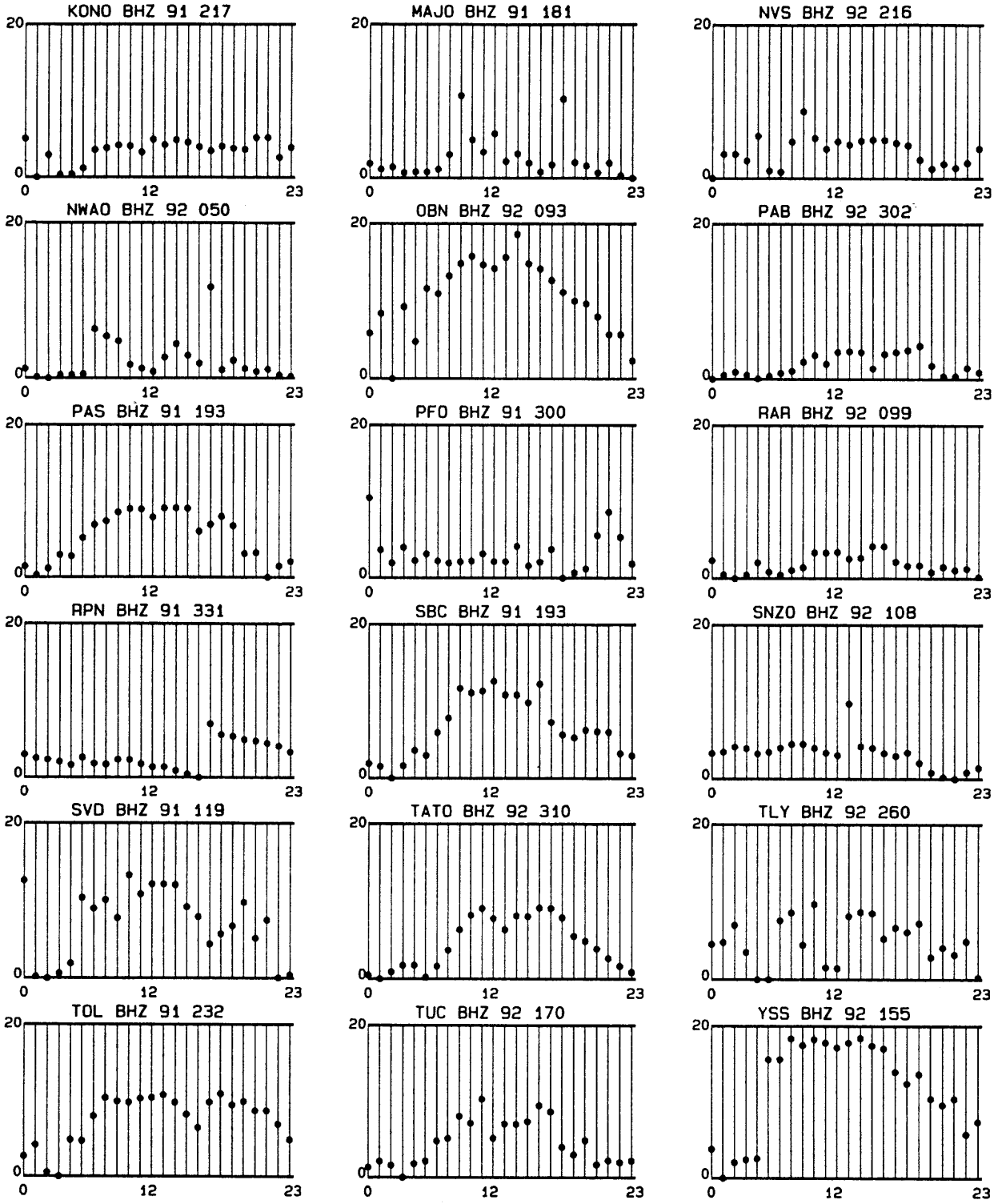

Figure 6.--Continued.

using borehole seismometers and seismometers designed for vault installation. One is cost. The borehole seismometers cost more than the vault seismometers. At a new station, the difference in cost between a good surface vault and a 100-meter borehole may not be significant, but at a station where a vault already exists, the additional cost for a borehole can be formidable.

The other tradeoff involves data requirements. Separate plots in Figure 7 show noise spectra overlays derived from the KS vertical and horizontal components and the STS vertical and horizontal components. Only the quiet spectral data are shown. The STS vertical component seismometer has better resolution than the KS vertical component seismometer at periods longer than 100 sec and the variability of noise from site to site is about the same for the two types of seismometers. For the horizontal-component seismometers, the resolution at quiet sites is about the same during the quiet periods shown, but the variability of noise between sites is much greater for the STS seismometers and, of course, noise at a given surface site will be much larger for the STS horizontals during windy periods. Butler and Hutt (1992) describe an ongoing experiment at Rarotonga in which borehole and vault data are compared. There appears to be little difference between the two data sets during quiet periods, but the horizontal vault data are much noisier during daytime hours. Clearly, there are data tradeoffs in the choice between STS and KS seismometers -- more useful bandwidth for the STS seismometers vs greater background noise stability in the horizontal components for the KS seismometers.

A closer look at the long-period noise recorded at some of the network stations is interesting. Pseudo particle motion plots of the first 500 sample points of the time series used for computing LP noise spectra at four stations are shown in Figure 8. The adjective 'pseudo' is used because the larger excursions in the plots actually portray Earth tilt rather than the apparent translational displacements. The numbers near the top of the individual plots represent thousands of digital counts.

The ANMO data shown in Figure 8 were acquired from a KS borehole seismometer, data from other stations were acquired from STS seismometers. The ANMO particle motion plots have approximately the same amplitude in the three planes and appear to be caused by natural microseisms or instrumental noise. The STS plots are more interesting because of the large excursions in the horizontal plane and the fact that they so precisely oriented. The orientation is maintained over the course of a day, as shown for CCM in Figure 9 and for BJI in Figure 10, and over the course of a year, as shown for BJI in Figure 11. Almost all STS horizontal signals appear to have some preferential orientation (see Figure 12 for examples from other stations), which could be due to prevailing wind direction or some preferentially-oriented compliance in the pier or surface rock. And the effects may not all be due to atmospheric turbulence. The noise data from CCM are unusual in that the seismometers are installed in a cave at a depth of 50 m, which should significantly attenuate surface tilt due to atmospheric pressure changes.

Broadband horizontal seismometers are exceedingly sensitive tilt meters. (See Rodgers, 1968, for a thorough analysis of the tilt response of horizontal pendulum seismometers.) The torque acting about the hinge of a pendulum seismometer due to

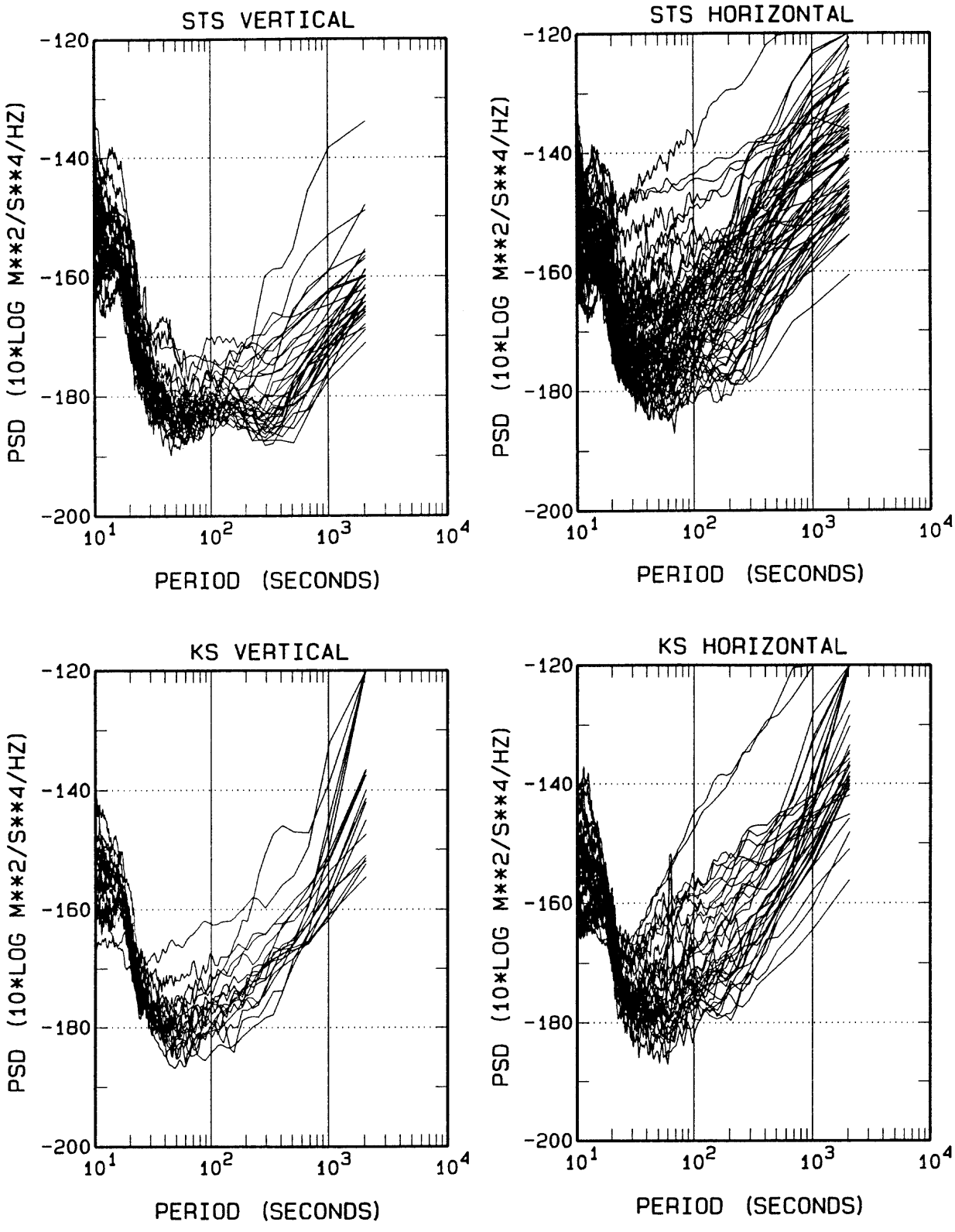

Figure 7.--Overlays of the STS and KS LP spectra. Vertical-component STS-1 spectra are in the upper left, horizontal STS-1 spectra in the upper right, vertical-component KS spectra in the lower left, and KS horizontal spectra in the lower right. The data were recorded during quiet, relatively wind-free periods.

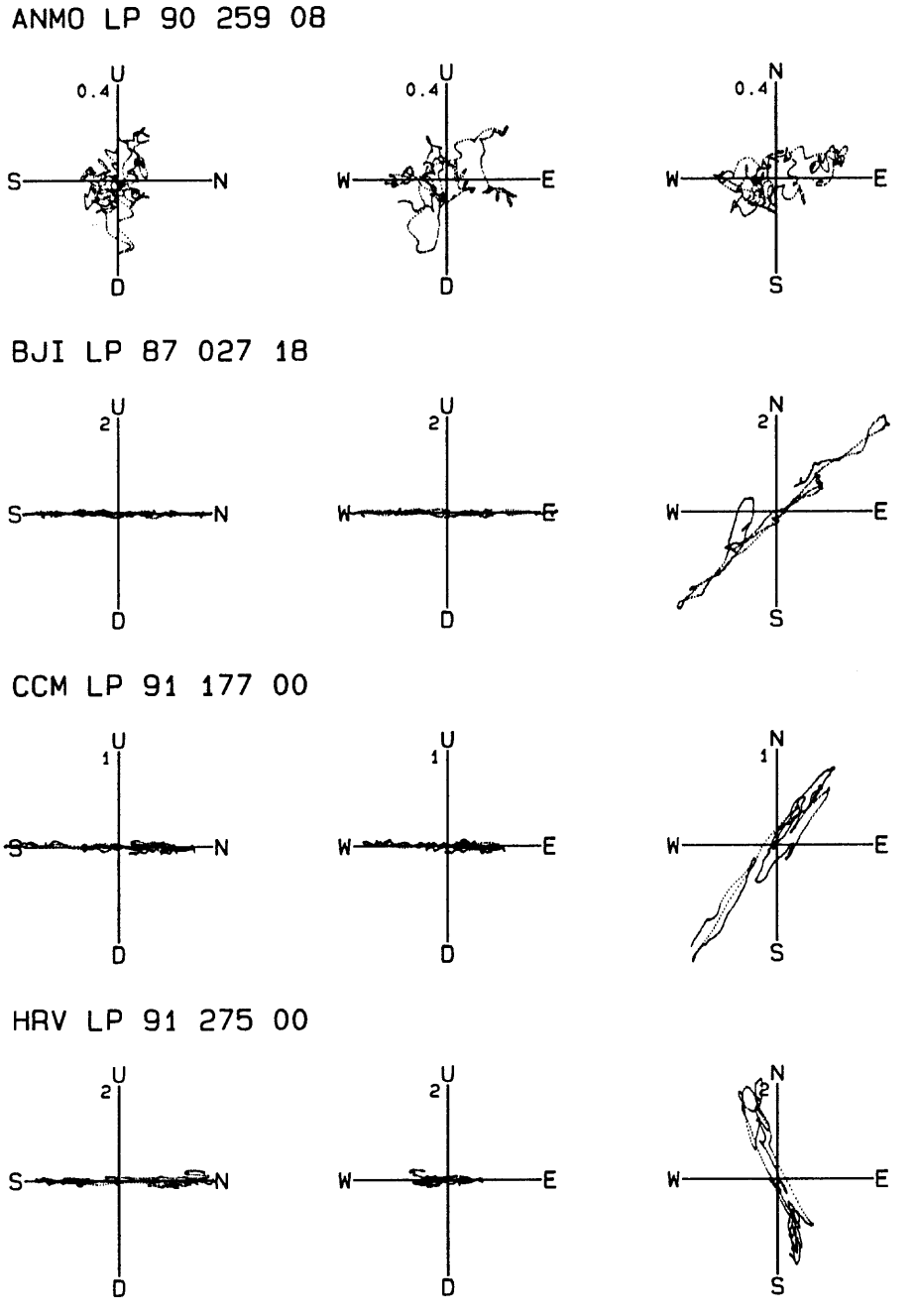

Figure 8.--Pseudo particle motion plots of LP signals from four stations. ANMO is equipped with a KS-36000I seismometer, the other stations with STS-1 seismometers.

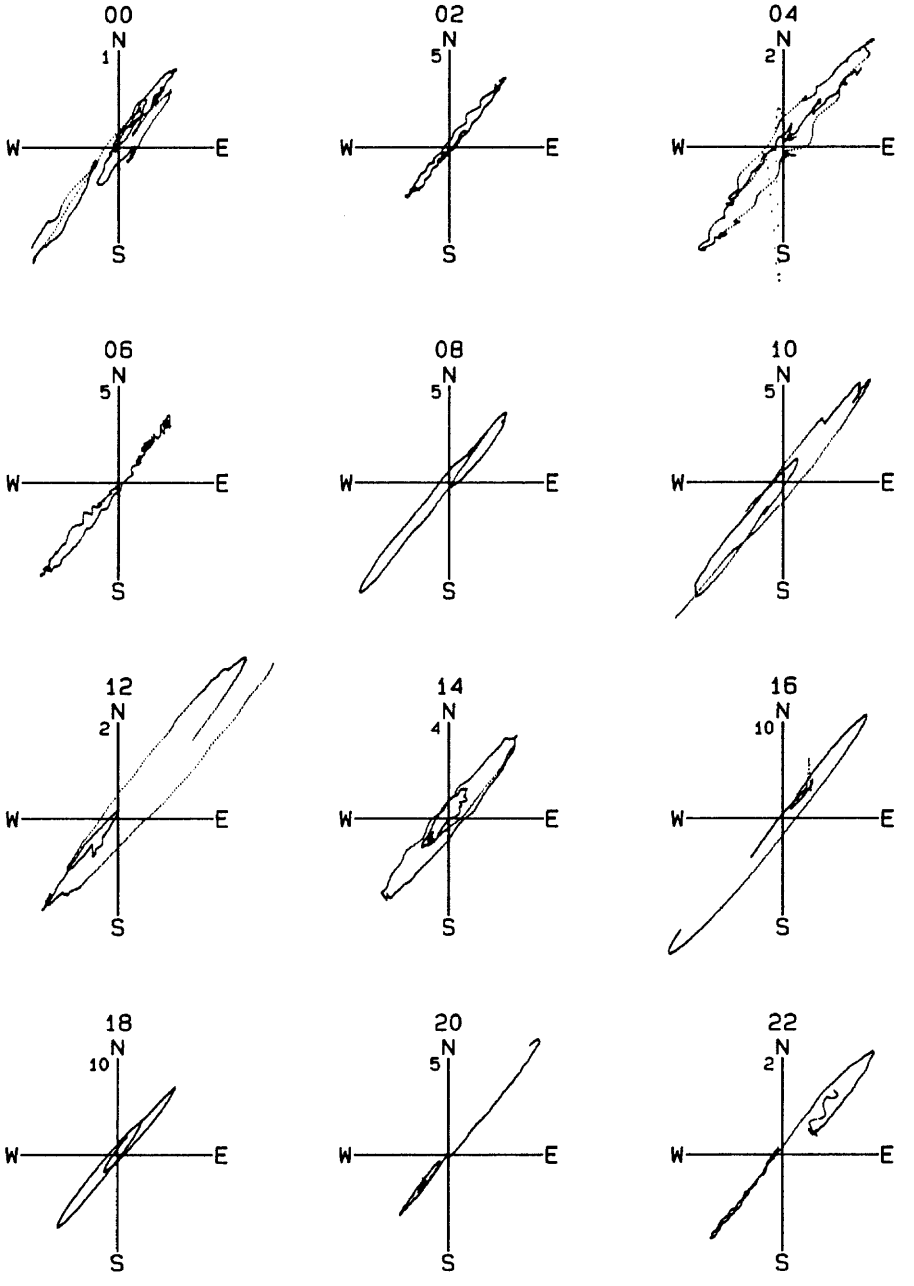

Figure 9.--Pseudo particle motion plots of CCM LPH signals taken at 2-hour intervals over a 24-hour period. Times are given above the plots.

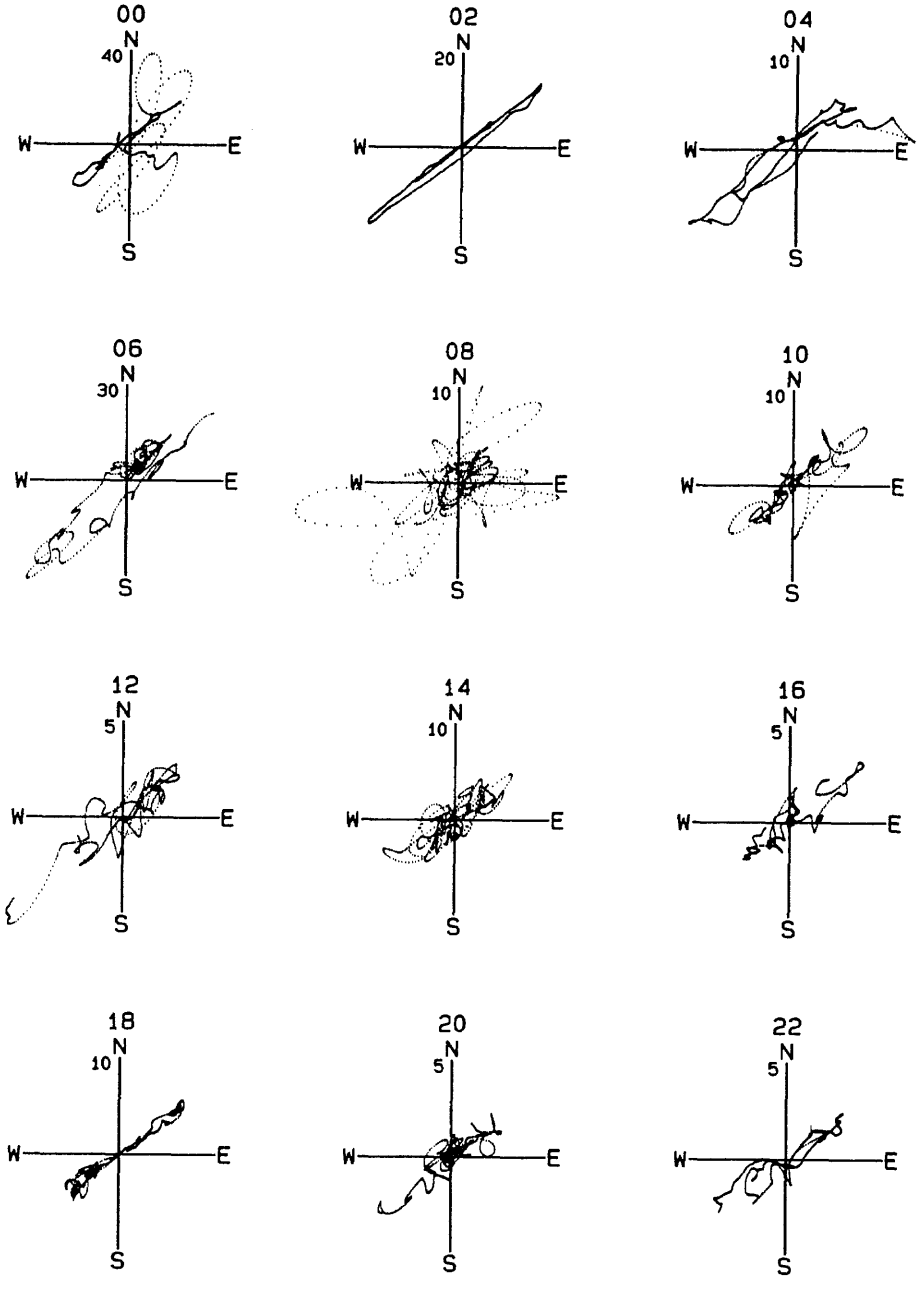

Figure 10.--Pseudo particle motion plots of BJI LPH signals taken at 2-hour intervals over a 24-hour period. Times are given above the plots.

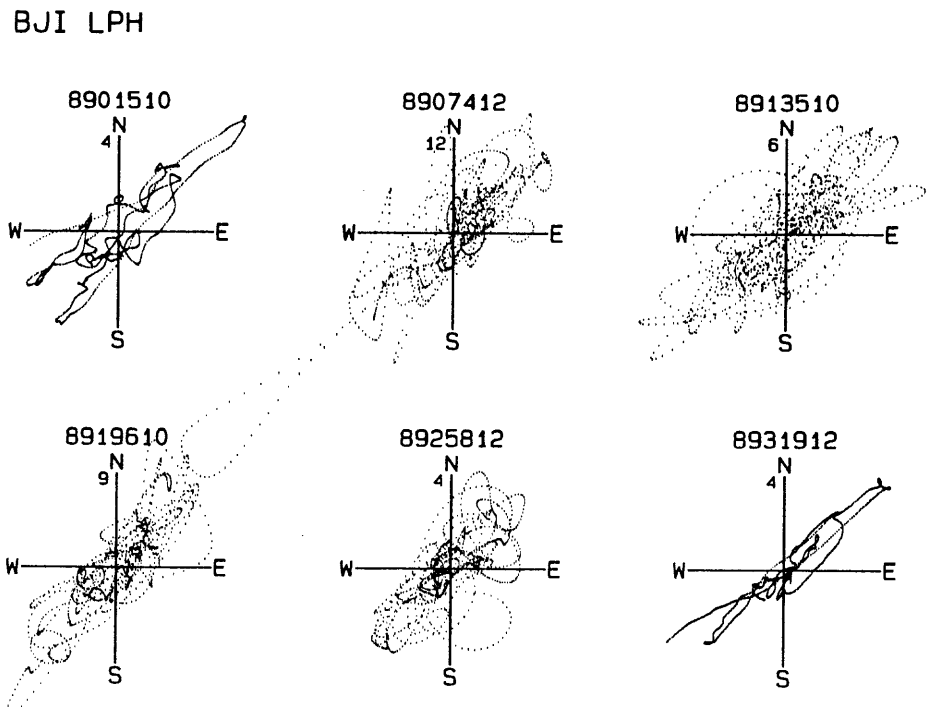

Figure 11.--Pseudo particle motion plots of BJI LPH signals taken at six different times of the year. Dates are given above the individual plots.

a translational Earth acceleration of a_x m/sec^2 is $-Mr_{cm}a_x$ newton-m, where M is the mass of the pendulum and r_{cm} is the distance from the hinge to the center of mass. The torque acting about the hinge of a horizontal pendulum seismometer due to a small tilt of θ radians is $Mg_o\theta r_{cm}$ newton-m, where g_o is the local acceleration of gravity. Then, a small tilt will produce an apparent translational acceleration of

$$a_x = g_o\theta \quad \text{m/sec}^2$$

At a period of 50 sec, the acceleration sensitivity of an IRIS/USGS or CDSN STS-1 seismometer is about 3.0 x 10^{10} counts/m/sec^2, so the tilt responsible for a signal output of 2,000 counts (as in the figures shown) is only about 6.8 nanoradians.

It is difficult to conceive of a horizontal seismometer that does not also respond to tilt, but it is easy to conceive of a tiltmeter, like a simple balance, that should not respond to translational acceleration. The development of a tiltmeter having sufficient resolution and stability to be used to subtract tilt signals from the output of a horizontal seismometer is one of the more predictable major advances for instrumental seismology.

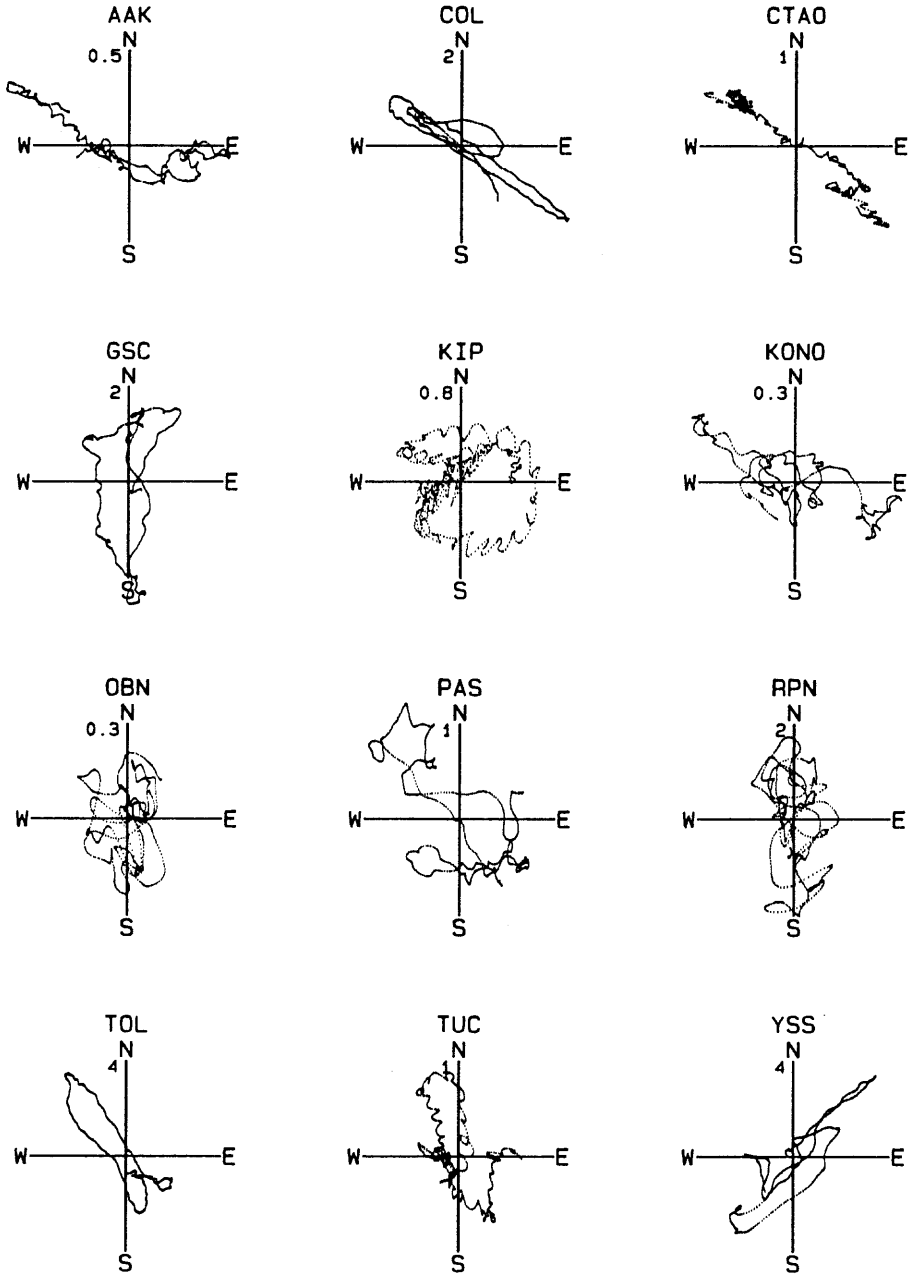

Figure 12.--Pseudo particle motion plots of LPH signals recorded at several other network stations.

NOISE MODELS

Background

Earth noise models have been part of the science at least since Brune and Oliver (1959) published curves of high and low seismic background displacement based on a worldwide survey of station noise. They have been useful as baselines for evaluating and comparing station site characteristics, for defining instrument specifications, and for predicting the response of sensor systems to quiet and noisy background conditions.

The USGS low-noise model (LNM) originated from a low-noise composite of SRO and ASRO data constructed by Peterson (1980) over the period range from 0.1 to 100 sec. The composite was derived from individual station PSD by overlaying the spectral plots and selecting low-noise points while ignoring narrow spectral peaks and valleys. Soon after, the SRO/ASRO composite was extended to longer periods by patching it at 100-sec period with IDA gravimeter data published by Agnew and Berger (1978), and extended to shorter periods by patching it at 0.5-sec period with low-noise spectra from Lajitas, Texas, published by Li (1981). The combined composite was approximated by a sequence of linear segments to make it easier to process in a computer, and the result was called a low-noise model. The LNM was modified slightly at short periods after Li and others (1984) published a new report on the Lajitas data. A high-noise model (HNM) was constructed in essentially the same fashion using SRO data from coastal and island sites.

New Noise Models

As STS-1 data became available from the China and IRIS broadband networks, it became clear that the LNM needed modification, especially at long periods. The construction of the new noise models has followed the same procedures used to develop the original noise models. In this case, straight line segments were graphically fitted to the lower and upper envelopes of the spectral overlay shown in Figure 2, and the result is shown in Figure 13. In graphically fitting the noise models to the overlay, the purpose was to preserve the general structure of the Earth noise without excessive attention to the narrow peaks and minor excursions of individual spectra.

Perceptive readers will notice that there are new spectra in the overlay that have not been seen before in this report. In fact, there are two additional spectral plots in the overlay. One was computed from vertical-component SP20 signals recorded at Alice Springs, Australia, and provided to the author by John Claassen of SNL; the other was computed from vertical-component SP20 signals recorded at BOSA (Boshof, South Africa), a new network station that will come on line in the near future. The Alice Springs and Boshof spectral data are plotted separately in Figure 14. The additional stations, both of which use Teledyne-Geotech GS-21 seismometers, were included to support the contention that the apparent noise bubble

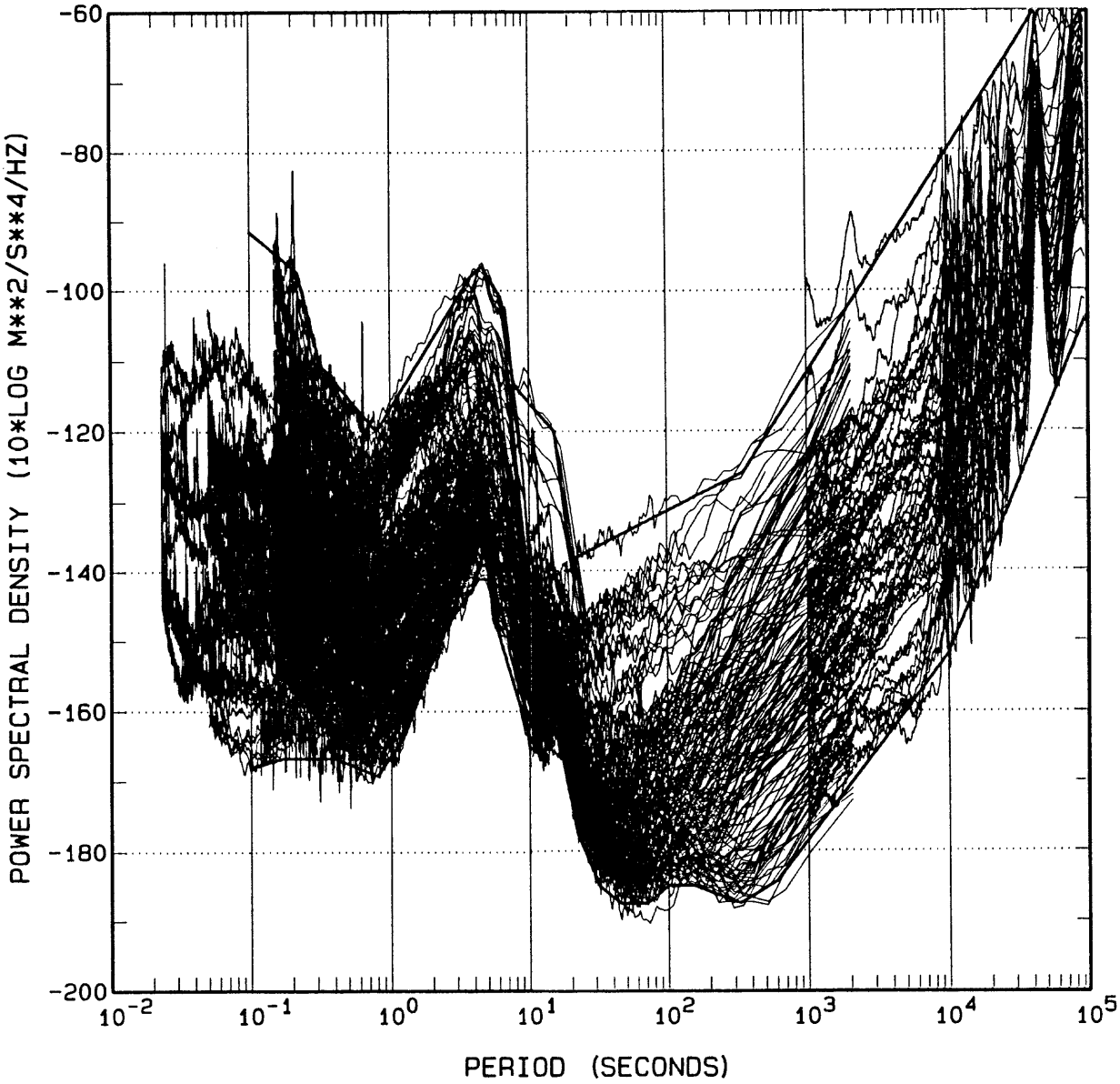

Figure 13.--An overlay of network spectra with straight-line segments fitted to the high-noise and low-noise envelopes of the overlay.

at 0.3 sec in Figure 2 is shaped primarily by instrument noise. Despite the additional data, the availability of spectra from quiet sites at periods shorter than 0.5 sec is clearly inadequate at the present time and revisions to the LNM may be needed as better data become available.

The new low-noise model (NLNM) may also need revision in the mid-period band if data records from mid-continent sites are found with lower amplitude microseisms. The selection of data records did not focus on this as a singular objective. Rather, it was expected that the spectra computed from a large number of data records gathered from an extensive global network of stations at different times

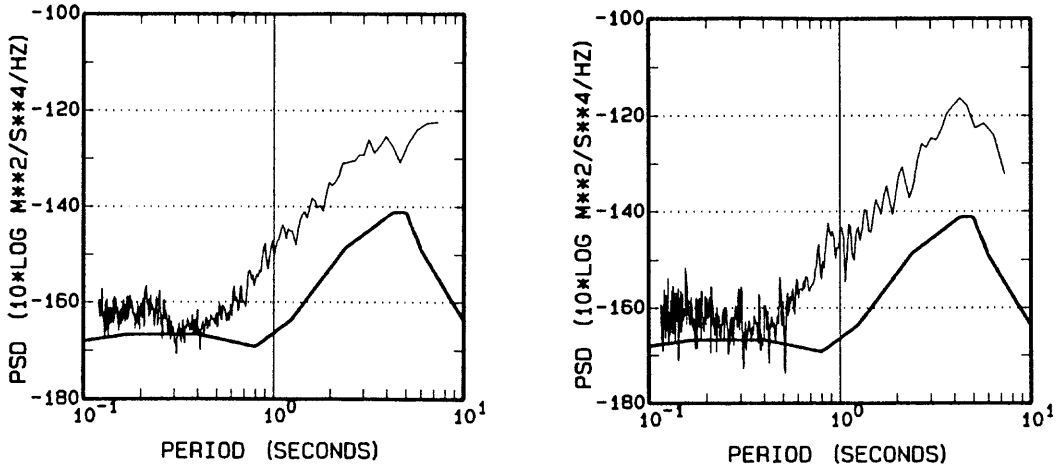

Figure 14.--Noise spectra computed from a 4096-sample time series from one element of the Alice Springs, Australia array (on left) recorded on September 28, 1991 beginning at 10 hours and 10 minutes, and spectra computed from a 4096-sample time series from Boshof, South Africa (on right) recorded on April 9, 1993 beginning at 19 hours, 8 minutes, and 20 seconds.

and seasons would produce a composite that included a reasonably good representation of quiet microseismic periods.

At long periods, the quiet spectral data obtained from STS-1 vertical-component seismometers at widely distributed stations (e.g., GSC, HIA, KIP, KONO, MAJO, TOL) are remarkably consistent, and this suggests that a global noise floor between 10 and 1,000 sec has been measured. There are vertical-component LP spectra from ZOBO that are lower in power than the NLNM at 50 - 100 sec period. However, the ZOBO spectra are not consistent with previous measurements (see Peterson, 1980) and may be distorted by seismometer misadjustment.

There also appears to be consistency in the spectra from quiet stations at very long periods (above 1000 sec), although the difference signal shown in Figure 3 would indicate a higher level of non-coherent noise in this band. The STS vertical-component seismometers are temperature sensitive, and it is in the VLP-ULP band that temperature cycling would be most likely to occur.

Like the original low-noise model (OLNM), the NLNM is a composite of station spectra obtained from many different instruments, vaults, geologic environments, and geographic regions. It is a hypothetical background spectrum that is unlikely to be duplicated at any single location on Earth.

The new high-noise model (NHNM) is a spectrum of *average* high background noise power in the network. Clearly, one can find sites that are noisier or periods of time at stations in the network that may be affected by microseismic storms or by increased local activities that disturb the instruments. The primary contributors to the NHNM are TOL, LZH, SBC, SPA, RPN, and RAR. TOL and LZH are inland stations situated on alluvium in very noisy locations, SBC is a coastal station with a combination of microseismic and cultural noise, SPA is situated on ice and subject to

$NLNM_{acc} = A + B \log_{10}(P)$ dB referred to 1 $(m/sec^2)^2/Hz$		
P	A	B
0.10 -	-162.36	5.64
0.17 -	-166.7	0.00
0.40 -	-170.00	-8.30
0.80 -	-166.40	28.90
1.24 -	-168.60	52.48
2.40 -	-159.98	29.81
4.30 -	-141.10	0.00
5.00 -	-71.36	-99.77
6.00 -	-97.26	-66.49
10.00 -	-132.18	-31.57
12.00 -	-205.27	36.16
15.60 -	-37.65	-104.33
21.90 -	-114.37	-47.10
31.60 -	-160.58	-16.28
45.00 -	-187.50	0.00
70.00 -	-216.47	15.70
101.00 -	-185.00	0.00
154.00 -	-168.34	-7.61
328.00 -	-217.43	11.90
600.00 -	-258.28	26.60
10000.00 - 100000.00	-346.88	48.75
$NLNM_{vel} = NLNM_{acc} + 20.0\log_{10}(P/2\pi)$ dB ref 1 $(m/sec)^2/Hz$		
$NLNM_{displ} = NLNM_{acc} + 20.0\log_{10}(P^2/4\pi^2)$ dB ref 1 m^2/Hz		

Table 3.--Line parameters for constructing the NLNM curve given the period (P).

$NHNM_{acc} = A + B \times \log_{10}(P)$ dB referred to 1 $(m/sec^2)^2/Hz$		
P	A	B
0.10 -	-108.73	-17.23
0.22 -	-150.34	-80.50
0.32 -	-122.31	-23.87
0.80 -	-116.85	32.51
3.80 -	-108.48	18.08
4.60 -	-74.66	-32.95
6.30 -	0.66	-127.18
7.90 -	-93.37	-22.42
15.40 -	73.54	-162.98
20.00 -	-151.52	10.01
354.80 - 100000.00	-206.66	31.63
$NHNM_{vel} = NHNM_{acc} + 20.0 \times \log_{10}(P/2\pi)$ dB ref 1 $(m/sec)^2/Hz$		
$NHNM_{displ} = NHNM_{acc} + 20.0 \times \log_{10}(P^2/4\pi^2)$ dB ref 1 m^2/Hz		

Table 4.--Line parameters for constructing the NHNM curve given the period (P).

severe local interference, and RPN and RAR are island stations with high amplitude microseisms.

The variables defining the PSD-axis intercepts and slopes of the NLNM and NHNM line segments are listed in Tables 3 and 4, respectively. For graphical presentation in this report, the noise model curves were generated by a C program that computes 100 points per decade. Both the original and new noise models are plotted together in Figure 15 to display the differences. The OHNM was based on SRO borehole data, which accounts for the large difference between the OHNM and NHNM curves at long periods.

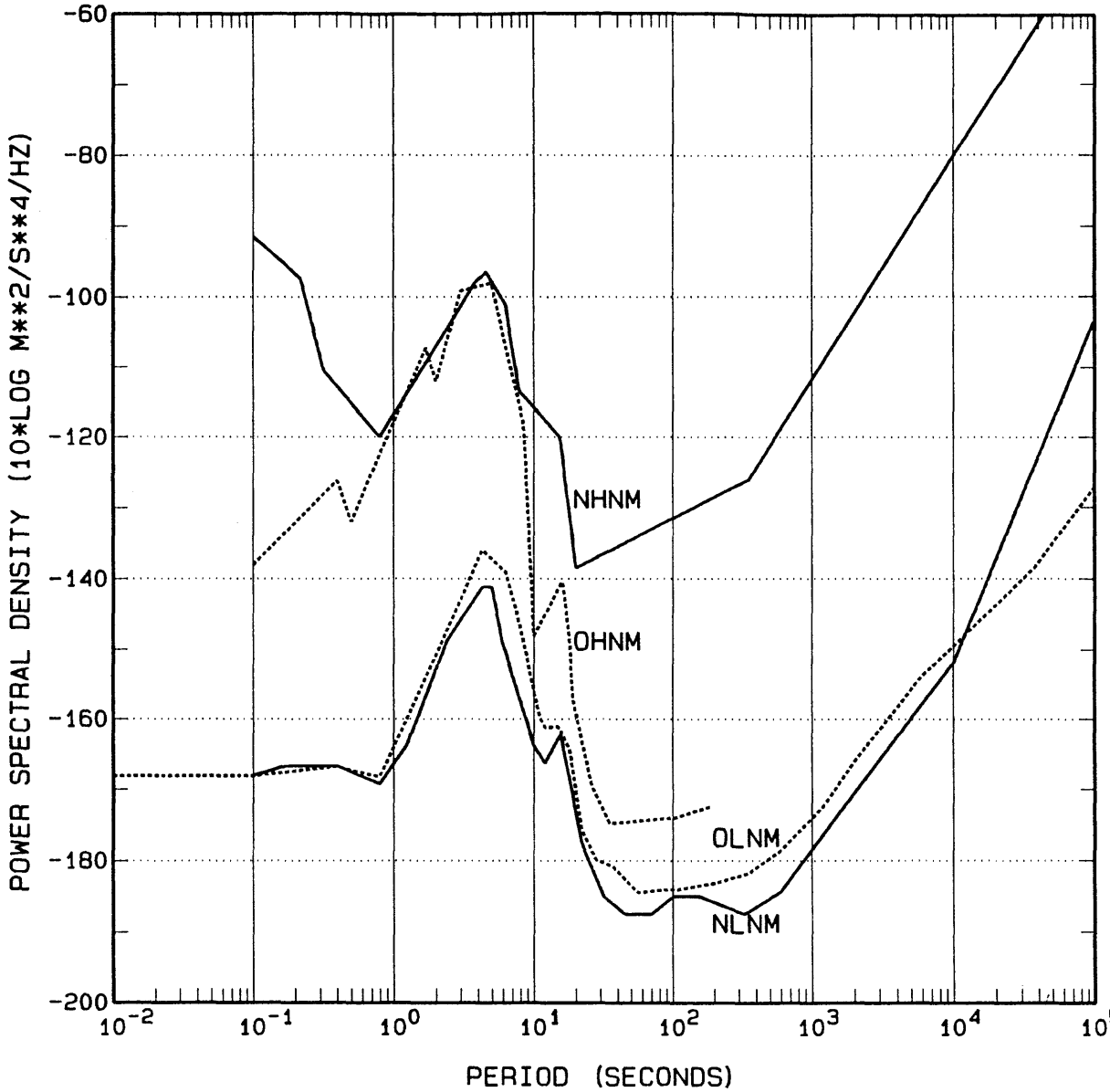

Figure 15.--Comparison of new and original noise models. The OHNM was based on SRO data, which accounts for the large difference between the OHNM and NHNM at long periods.

Amplitude Spectra

Occasionally it is necessary to compare the amplitude of background noise, as measured by an analyst, with the background noise that has been computed from a data record and given in units of power spectral density. The procedures used to convert PSD to units of peak or peak-to-peak amplitude are straightforward, but the results will vary depending on the integration bandwidth chosen to compute RMS values and the multiplier chosen to convert RMS amplitude to peak or peak-to-peak amplitude.

Several authors (Frantii and others, 1962; Fix, 1972; Melton, 1978) have used a 1/3-octave bandwidth in computing RMS amplitudes from PSD. Melton reasoned that the 1/3-octave band, which is nearly ±10% about the center period in width, is close to the tolerance that might be expected of an analyst when measuring the period of a signal on a seismogram. The errors are likely to be smaller today on work stations, but the 1/3-octave bandwidth is a reasonable convention. The differences in RMS values when using 1/4- or 1/2-octave bandwidths are less than 20%.

The conversion of RMS amplitudes to peak amplitudes is often based on the assumption that the sample amplitudes of the waveform have a Gaussian distribution and a multiplier is chosen to give a desired probability that the peak amplitudes lie within the range given by the product of the multiplier and RMS amplitude. For example, there is a 95% probability that the instantaneous peak amplitudes of a Gaussian waveform will lie within a range of twice its RMS value. However, having a 95% probability of lying below the specified peak amplitudes is not an appealing definition for a low-noise amplitude spectrum. The author prefers to convert RMS amplitudes to average peak or peak-to-peak amplitudes based on the following logic. When a Gaussian signal is passed through a narrow-band filter, the absolute peak amplitudes of the filtered signal *envelope* have a Rayleigh distribution (Bennett, 1960; Bell, 1960) with a probability density expressed as

$$|x_p| = \frac{|x_p|}{\sigma^2} e^{-\frac{x_p^2}{2\sigma^2}}$$

where x_p is the peak amplitude of the envelope and σ is the RMS amplitude of the sample values after the mean has been removed. The average value of the peak amplitudes (see Bennett, 1960) is

$$|\overline{x_p}| = \int_0^\infty \frac{x_p^2}{\sigma^2} e^{\left(-\frac{x_p^2}{2\sigma^2}\right)} dx_p$$

$$= \sqrt{\frac{\pi}{2}}\sigma = 1.253\sigma$$

and then the amplitude of the average peak-to-peak value is 2.506σ.

Figures 16 and 17 illustrate filtered VBB and LP signals used to compare measured average peak amplitudes with the theoretical average peak amplitude of 1.253σ. In each of the figures, the unfiltered waveform is shown at the top, and the distribution of sample amplitudes is plotted at the right together with a Gaussian probability density function. The four waveforms below were filtered through 1/3-octave, 6-pole bandpass filters, and the distribution of peak amplitudes for each filtered waveform is plotted on the right together with the Rayleigh probability density function. Each of the filtered waveforms is labeled with the filter center period and the measured ratio of average peak to RMS amplitude.

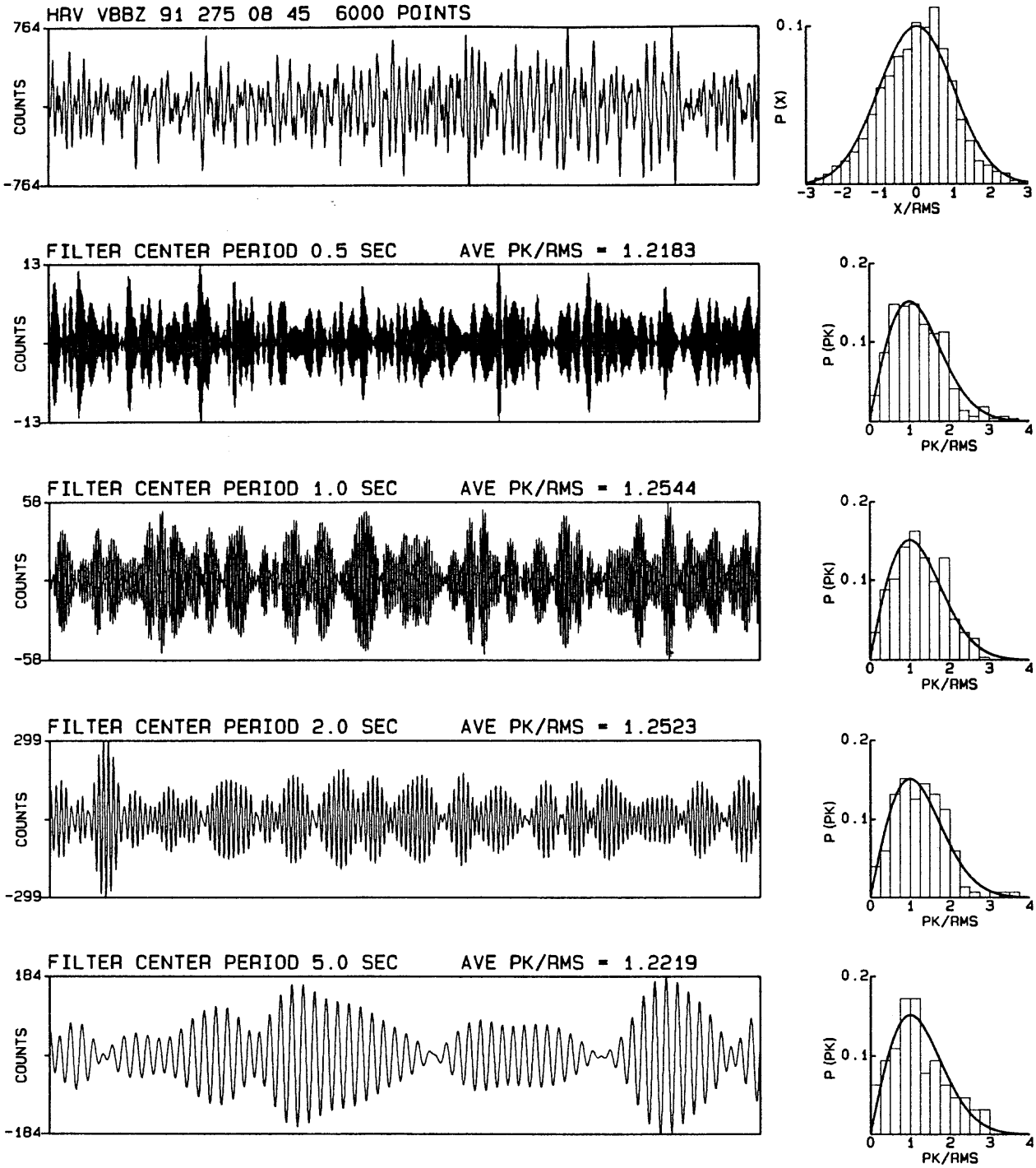

Figure 16.--An original VBBZ waveform at the top and four filtered waveforms derived from the original using 1/3-octave filters at the center periods listed. The distribution of sample amplitudes in the original time series is plotted to the right of the original waveform together with a Gaussian probability density function. The distributions of individual peak values in the filtered waveforms are shown plotted to the right of each the waveforms together with Rayleigh probability density functions. The ratios of average peak values to the RMS amplitude vary from 1.2183 to 1.2544. The theoretical value is 1.253.

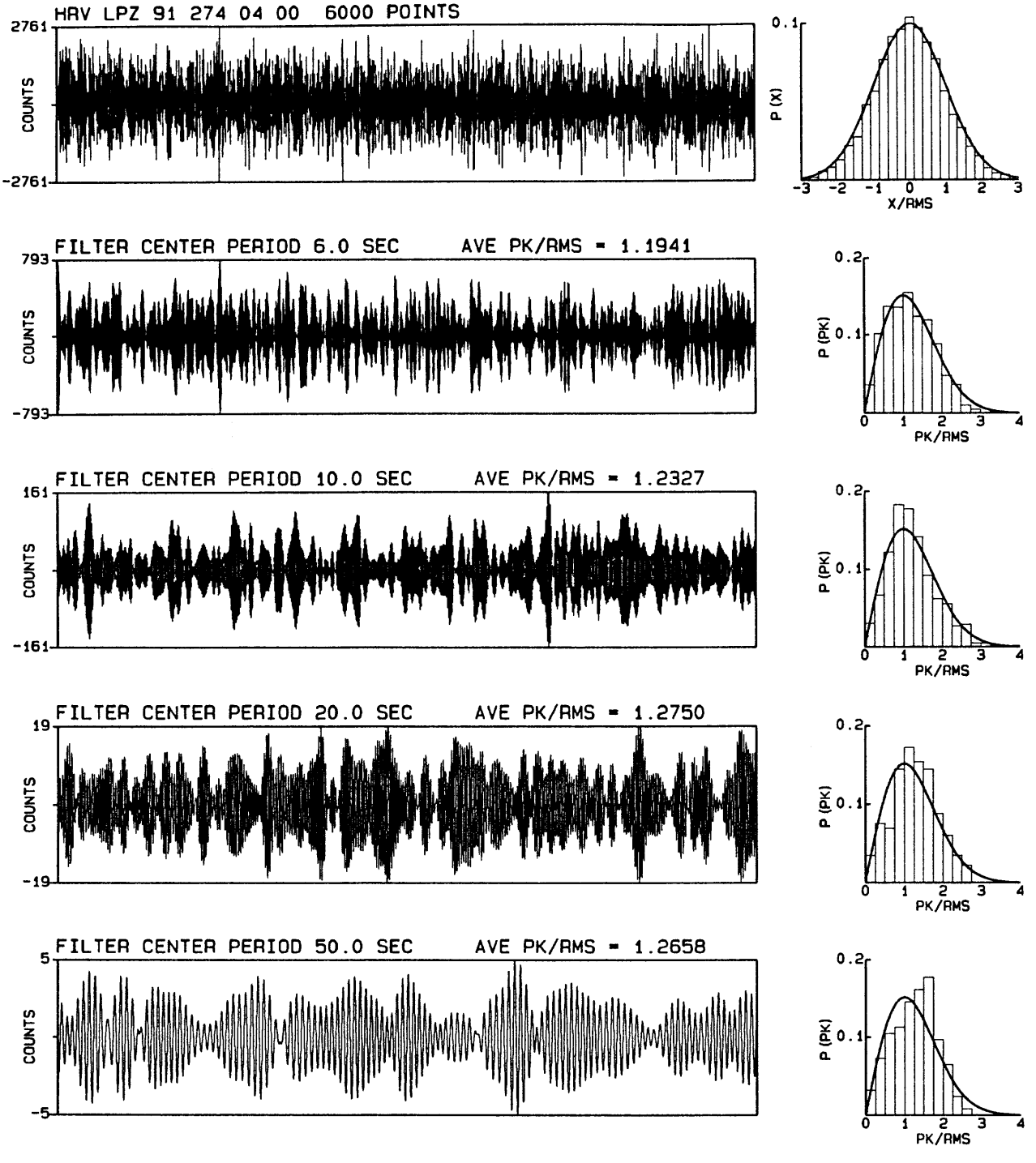

Figure 17.--An original LPZ waveform at the top and four filtered waveforms derived from the original using 1/3-octave filters at the center periods listed. The distribution of sample amplitudes in the original time series is plotted to the right of the original waveform together with a Gaussian probability density function. The distributions of individual peak values in the filtered waveforms are shown plotted to the right of each the waveforms together with Rayleigh probability density functions. The ratios of average peak values to the RMS amplitude vary from 1.1941 to 1.2750. The theoretical value is 1.253.

The NLNM and NHNM spectra, converted to units of average peak-to-peak acceleration using the procedures described above, are plotted in Figure 18. The NLNM and NHNM curves can now be compared directly with the Brune and Oliver noise curves which are also plotted in Figure 18. The differences between the NHNM curve and the Brune and Oliver maximum curve are most likely due to the methods used to select the data. The Brune and Oliver maximum noise curve is based on the maximum amplitudes that may be expected over a one year interval of time (Brune and Oliver, 1959), whereas the NHNM peak-to-peak amplitudes represent the typical rather than maximum background levels expected at noisy sites. The differences between the Brune and Oliver minimum and the NLNM most likely result from evolving technology, especially improvements in the resolution of seismometers and processors. Technological improvements are certain to continue, and the noise models are very likely to evolve as well.

ACKNOWLEDGEMENTS

The author has benefited immensely by years of productive collaboration and discussions with Bob Hutt and Gary Holcomb, which included helpful comments and suggestions during the preparation and review of this report. Bob Hutt provided all of the test data used in this report as well. The author thanks Holly Given and Jon Berger for information on the IRIS/IDA stations and suggestions that improved the accuracy of the report. The author also thanks John Claassen for the Alice Springs data and thoughtful suggestions during review and Peter Rodgers for his helpful comments and suggestions upon reviewing the report.

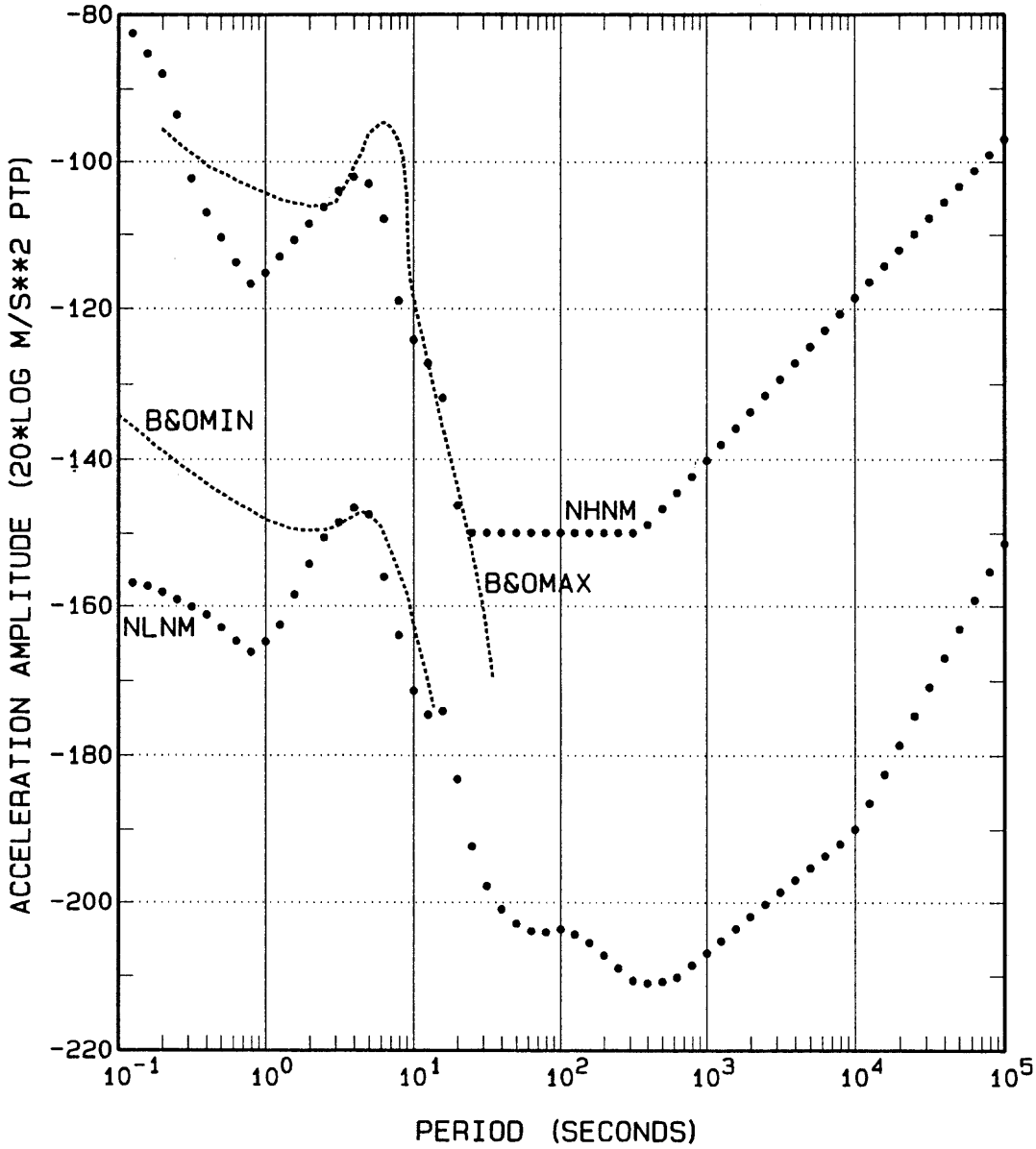

Figure 18.--The new high- and low-noise models (NLNM and NHNM) plotted as peak-to-peak acceleration amplitude spectra and compared with the Brune and Oliver maximum and minimum (B&OMAX and B&OMIN) curves published in 1959.

REFERENCES

Agnew, D.C., J. Berger, R. Buland, W. Farrell, and F. Gilbert, 1976. International deployment of accelerometers: a network for very long period seismology, *EOS Trans. Am. Geophys. Union*, 57, 180-188.

Agnew, D.C. and J. Berger, 1978. Vertical seismic noise at very low frequencies, *J. Geophys. Res.*, 83, 5420-5424.

Bell, R.B., 1960. *Electrical Noise*, D. Van Nostrand Company, London, 342 p.

Bendat, J.S. and A.G. Piersol, 1971. *Random Data: Analysis and Measurement Procedures*, John Wiley and Sons, New York, 407 p.

Bennett, W.R., 1960. *Electrical Noise*, McGraw-Hill Book Company, New York, 280 p.

Breding, D.R., 1983. Data users' guide for the regional seismic test network (RSTN), *Sandia Report Sand82-2935*, Albuquerque, New Mexico, 85 p.

Breding, D.R., 1987. Seismic background noise at the Norwegian regional seismic array, *Sandia Report Sand87-1188*, Albuquerque, New Mexico, 56 p.

Brune, J.N. and J. Oliver, 1959. The seismic noise of the Earth's surface, *Bull. Seism. Soc. Am.*, 49, 349-353.

Butler, R. and C.R. Hutt, 1992. Seismic noise on Rarotonga: surface versus downhole, *EOS Trans. Am. Geophys. Union.*, 73, 548-549.

Fix, J.E., 1972. Ambient Earth motion in the period range from 0.1 to 2560 sec, *Bull. Seism. Soc. Am.*, 62, 1753-1760.

Frantii, G.E., D.E. Willis, and J.T. Wilson, 1962. The spectrum of Earth noise, *Bull. Seism. Soc. Am.*, 52, 113-121.

Given, H.K., 1990. Variations in broadband seismic noise at IRIS/IDA stations in the USSR with implications for event detection, *Bull. Seism. Soc. Am.*, 80 Part B, 2072-2088.

Given, H.K., J. Berger, J-F Fels, D. Horwitt, and C. Winther, 1992. The IRIS-3 high resolution data acquisition system, *Scripps Institution of Oceanography Reference Series 92-32*, University of California, San Diego, 60 p.

Holcomb, L.G., 1989. A direct method for calculating instrument noise levels in side-by-side seismometer evaluations, *U.S. Geological Survey Open-File Report*, 89-214 35 p.

Joint Report, 1987. The China digital seismograph network, A Joint Report by the Institute of Geophysics, State Seismological Bureau and the Albuquerque Seismological Laboratory, Beijing, China, 91 p.

Kanamori, H., E. Haukson, and T. Heaton, 1991. TERRAscope and CUBE project at Caltech, *EOS Trans. Am. Geophys. Union*, 72, 564.

Li, T.M.C., 1981. Lajitas quiet site noise study, *Teledyne-Geotech Technical Report 81-10*, Garland, Texas, 31 p.

Li, T.M.C., J.F. Ferguson, E. Herrin, and H.B. Durham, 1984. High-frequency seismic noise at Lajitas, Texas, *Bull. Seism. Soc. Am.*, 74, 2015-2033.

Melton, B.S., 1978. The sensitivity and dynamic range of inertial seismographs, *Rev. Geophys. Space Phys.*, 14, 93-116.

Otnes, R.K. and L. Enochson, 1972. *Digital Time Series Analysis*, John Wiley and Sons, New York, 467 p.

Peterson, J. 1980. Preliminary observations of noise spectra at the SRO and ASRO stations, *U.S. Geological Survey Open-File Report* 80-992, 25 p.

Peterson, J., C.R. Hutt, and L.G. Holcomb, 1980. Test and calibration of the seismic research observatory, *U.S. Geological Survey Open-File Report 80-187*, 85 p.

Peterson, J. and C.R. Hutt, 1982. Test and calibration of the digital world-wide standardized seismograph, *U.S. Geological Survey Open-File Report 82-1087*, 170 p.

Peterson, J. and E.E. Tilgner, 1985. Description and preliminary testing of the CDSN seismic sensor systems, *U.S. Geological Survey Open-File Report 85-288*, 60 p.

Peterson, J. and C.R. Hutt, 1992. IRIS/USGS plans for upgrading the global seismograph network, *U.S. Geological Survey Open-File Report 89-471*, 42 p.

Pomeroy, P.W., G. Hade, J. Savino, and R. Chander, 1969. Preliminary results from the high-gain wideband long-period electomagnetic seismograph systems, *J. Geophys. Res.* 74, 3295-3298.

Rodgers, P.W., 1968. The response of the horizontal pendulum seismometer to Rayleigh and Love waves, tilt, and free oscillations of the Earth, *Bull. Seism. Soc. Am.*, 58, 1384-1406.

Rodgers, P.W., S.R. Taylor, and K.K. Nakanishi, 1987. System and site noise in the regional seismic test network from 0.1 to 20 Hz, *Bull. Seism. Soc. Am.*, 77, 663-678.

Sorrells, G.G., 1971. A preliminary investigation into the relationship between long-period seismic noise and local fluctuations in the atmospheric pressure field, *Geophys. J.* 26, 71-82.

Sorrells, G.G., J.A. McDonald, Z.A. Der, and E. Herrin, 1971. Earth motion caused by local atmospheric pressure changes, *Geophys. J.*, 26, 83-98.

Stearns, S.D., 1975. *Digital Signal Analysis*, Hayden Book Company, Rochelle Park, New Jersey, 280 p.

Steim, J.M., 1986. The very-broad-band seismograph. Doctoral Thesis, Harvard University, Cambridge, Massachusetts.

APPENDIX

STATION NOISE SPECTRA

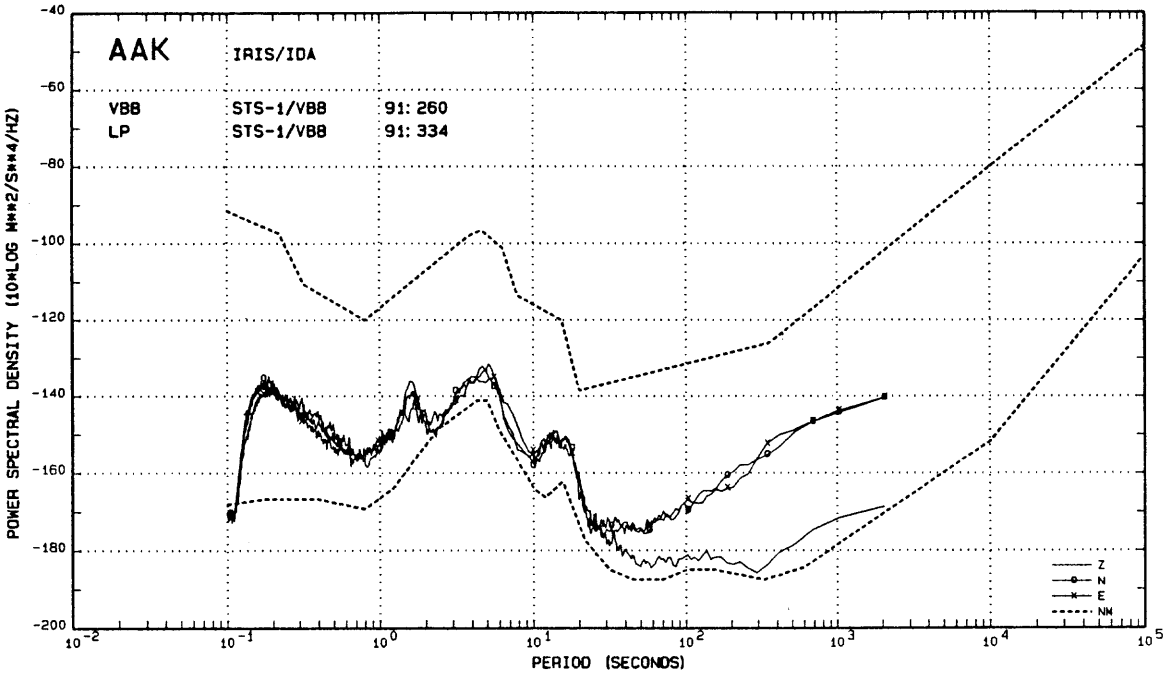

Figure A1.--Noise spectra from the Ala Archa, Kyrgyzstan IRIS/IDA station. The peak at 1.6 seconds is not always present and may be caused by lake microseisms.

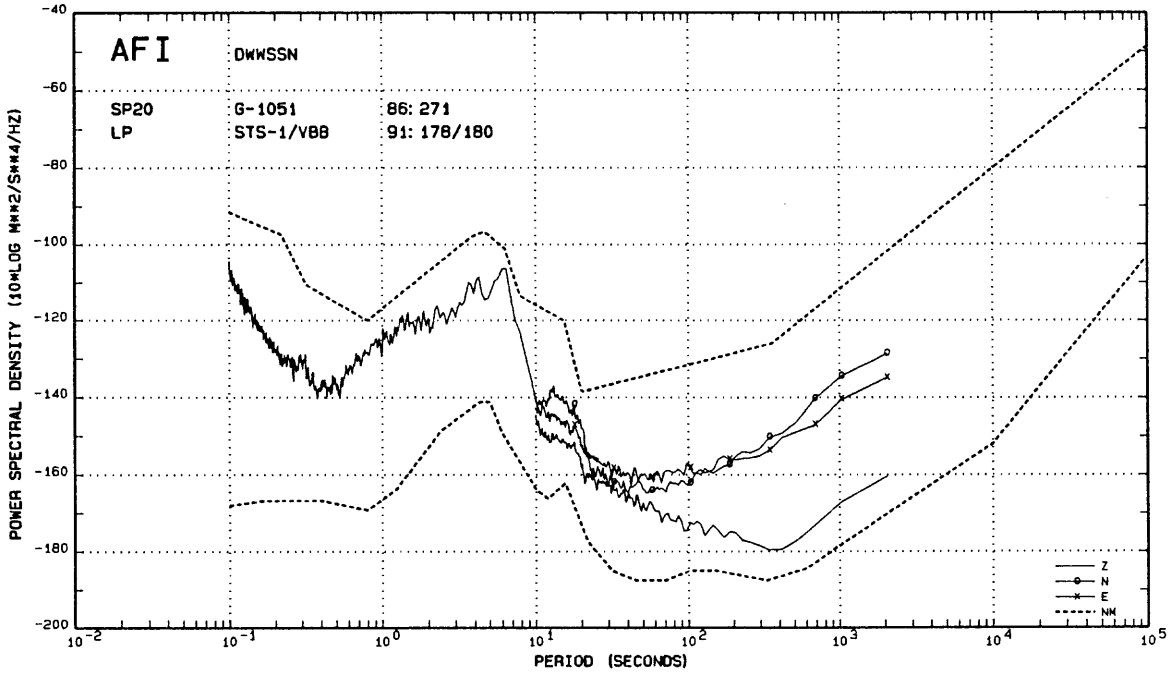

Figure A2.--Noise spectra from the Afiamalu, Western Samoa DWWSSN station. The system is equipped with STS seismometers. Aliasing noise could be present in the LP signals because of the high amplitude microseisms.

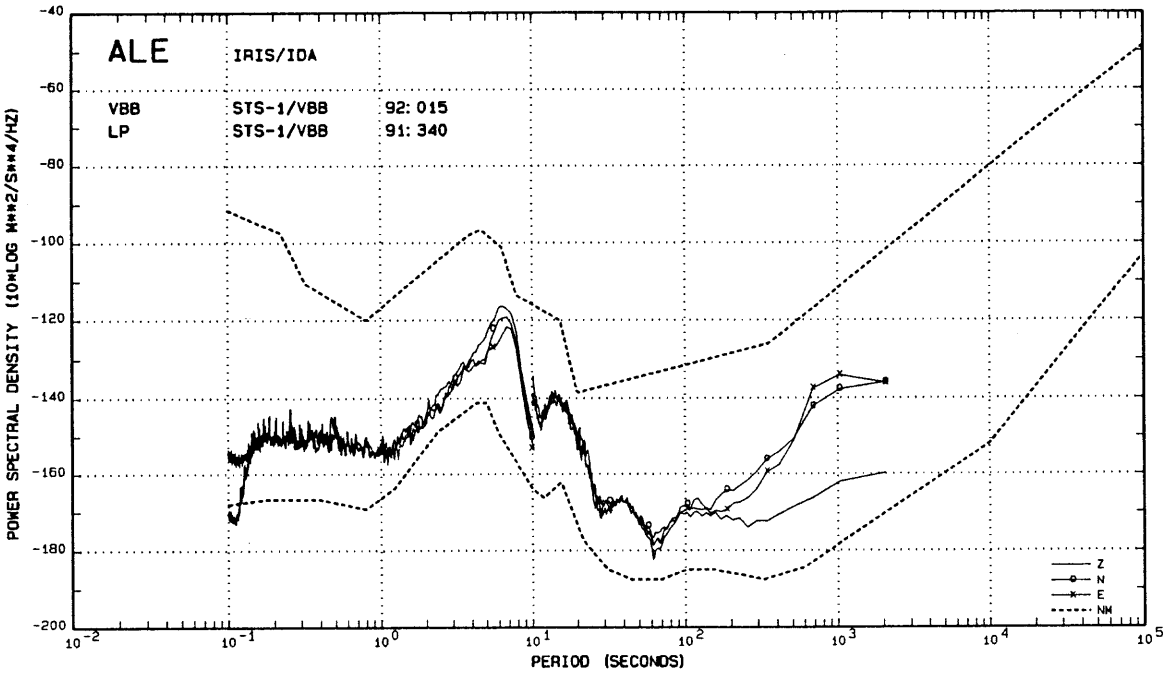

Figure A3.--Noise spectra from the Alert, Canada IRIS/IDA station.

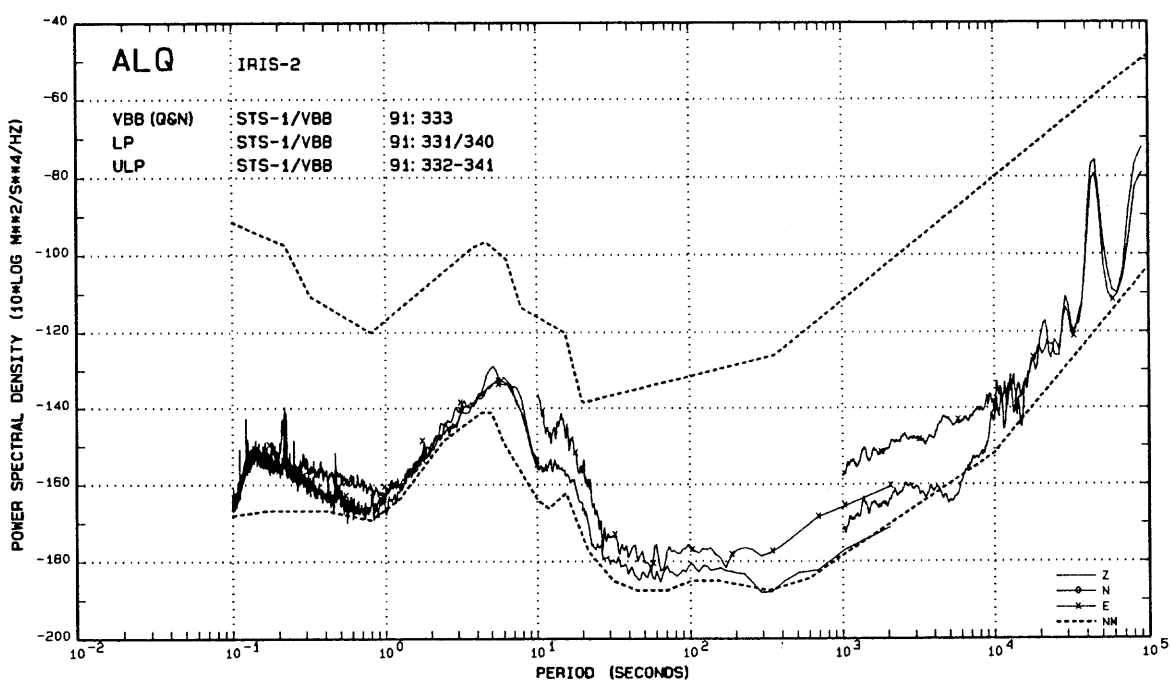

Figure A4.--Noise spectra from the Albuquerque, New Mexico IRIS-2 test system. The test system is installed in the ASL subsurface vault. The LP component signals shown here were recorded at different times.

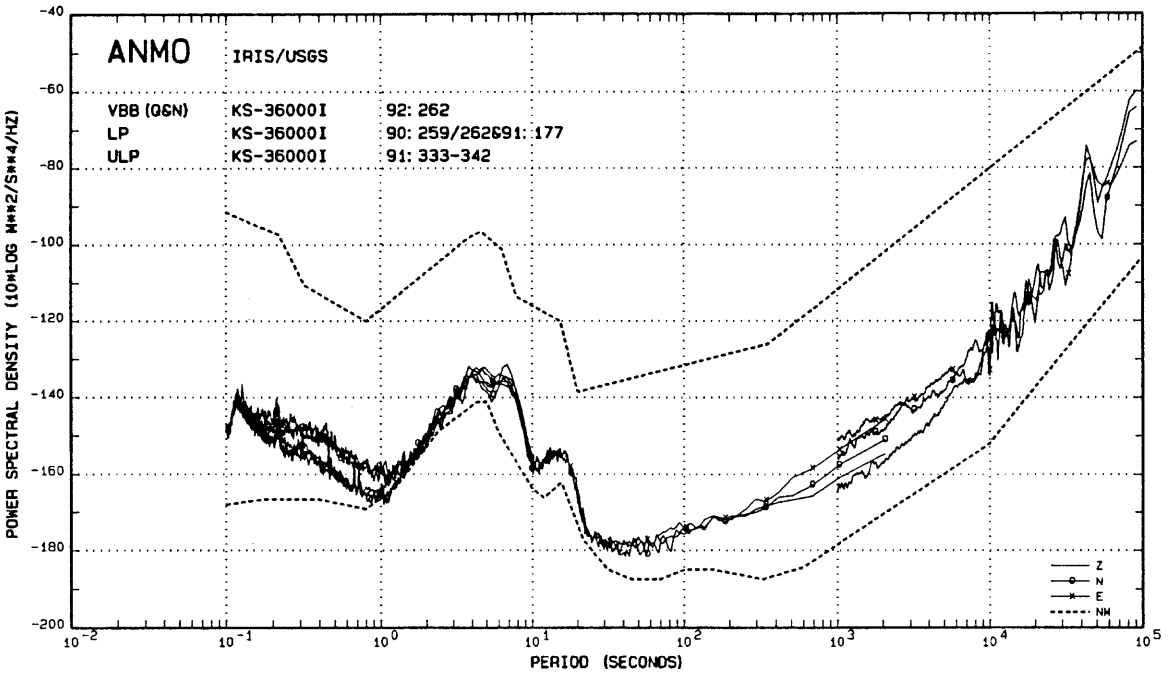

Figure A5.--Noise spectra from the Albuquerque, New Mexico IRIS-2 station.

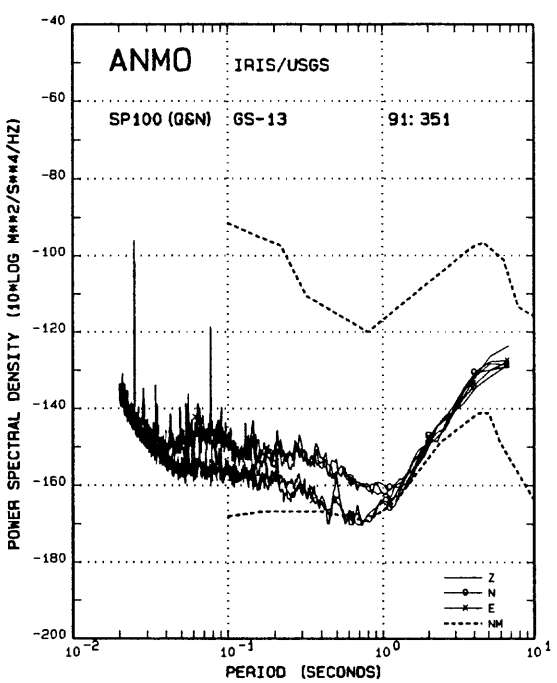

Figure A6.--Noise spectra from the Albuquerque, New Mexico IRIS-2 station. The ANMO SP data shown here were derived from SP seismometers operated in the ASL subsurface vault. The seismometers have since been moved to a site closer to the recording equipment located near the borehole seismometer.

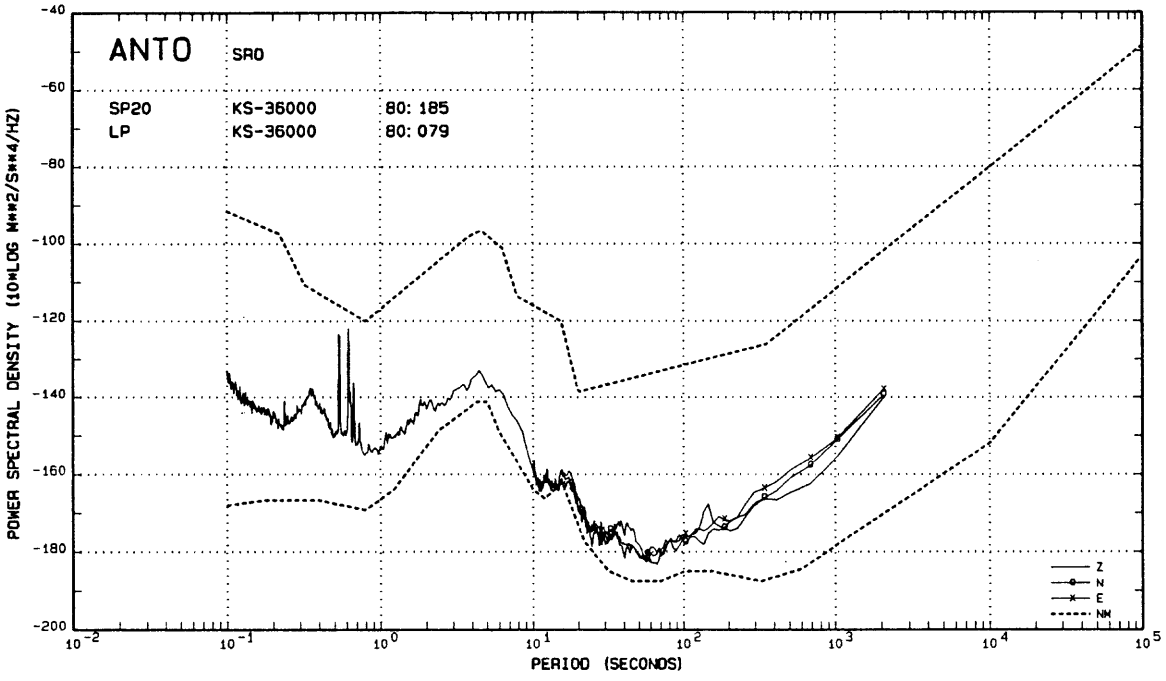

Figure A7.--Noise spectra from the Ankara, Turkey SRO station. The ANTO SRO system has recently been replaced by an IRIS-2 system.

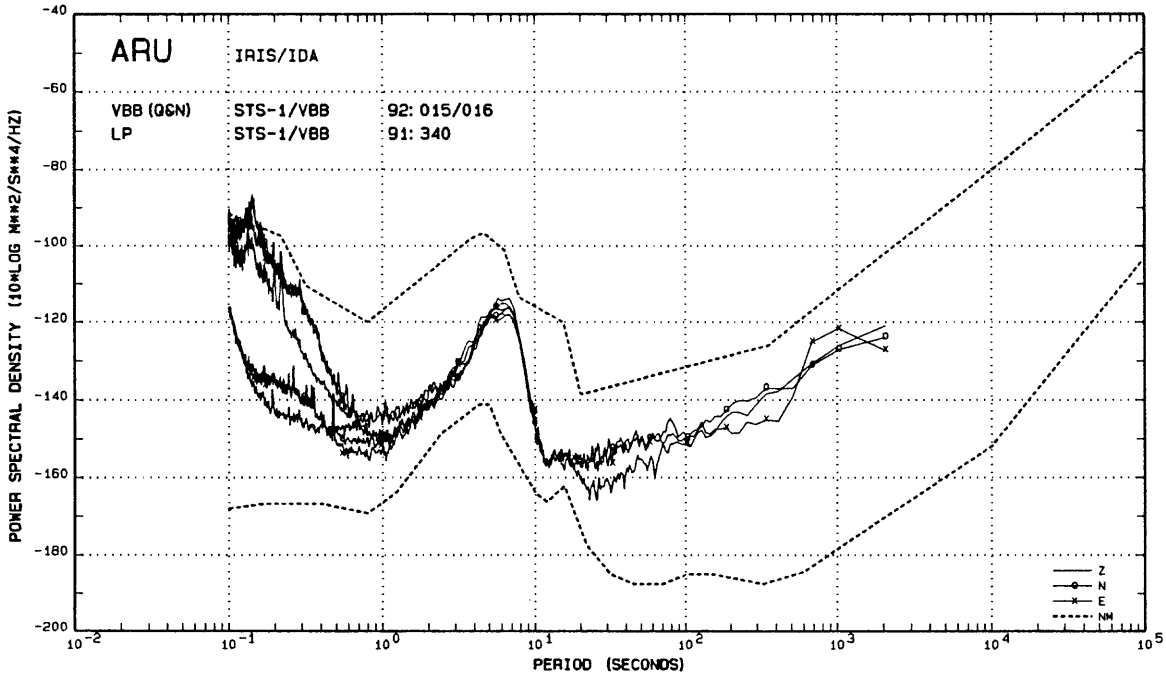

Figure A8.--Noise spectra from the Arti, Russian Federation IRIS/IDA station..

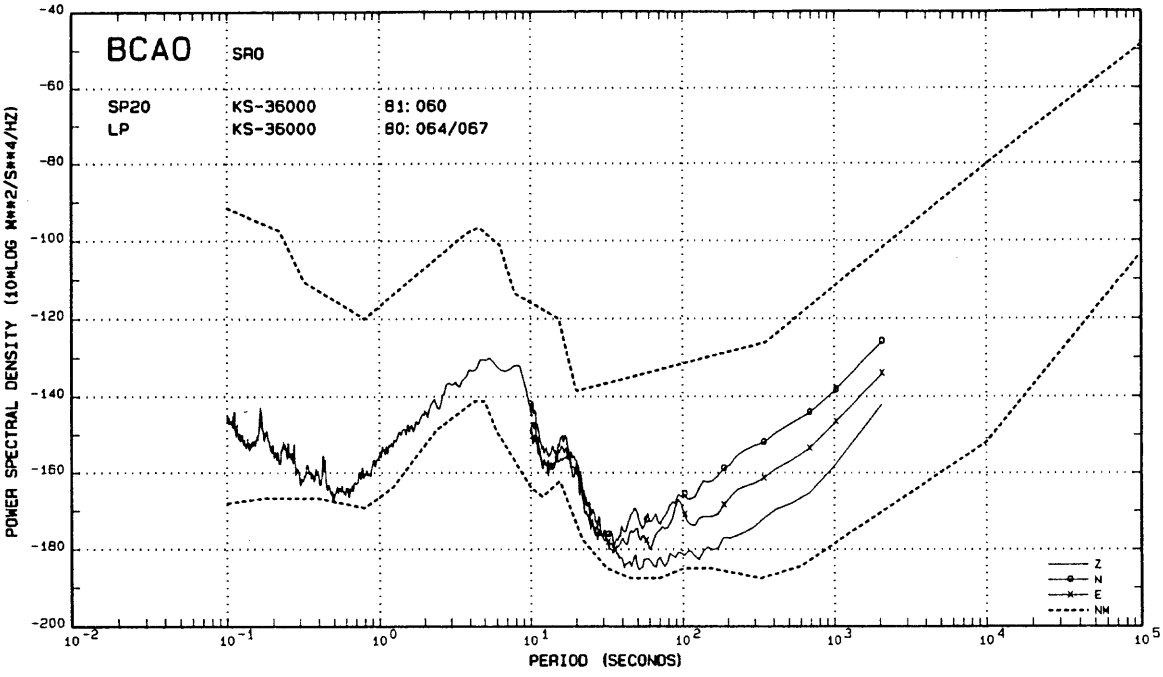

Figure A9.--Noise spectra from the Bangui, Central African Republic SRO station.

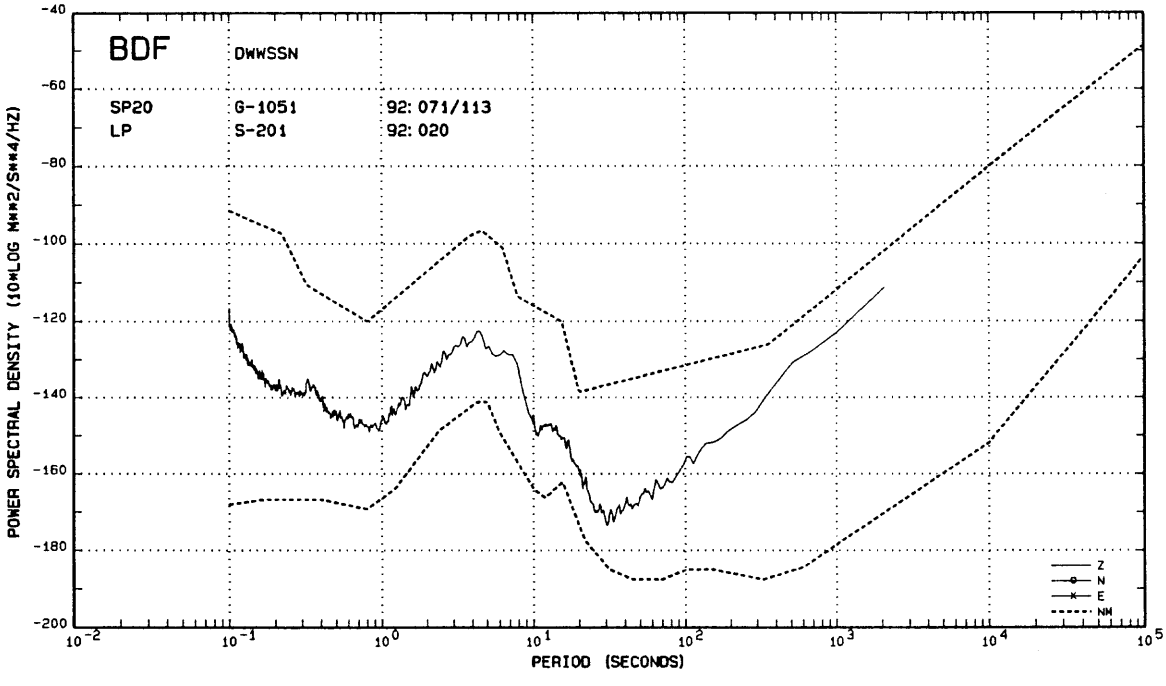

Figure A10.--Noise spectra from the Brasilia, Brazil DWWSSN station. Good data from the LP horizontal components were not available.

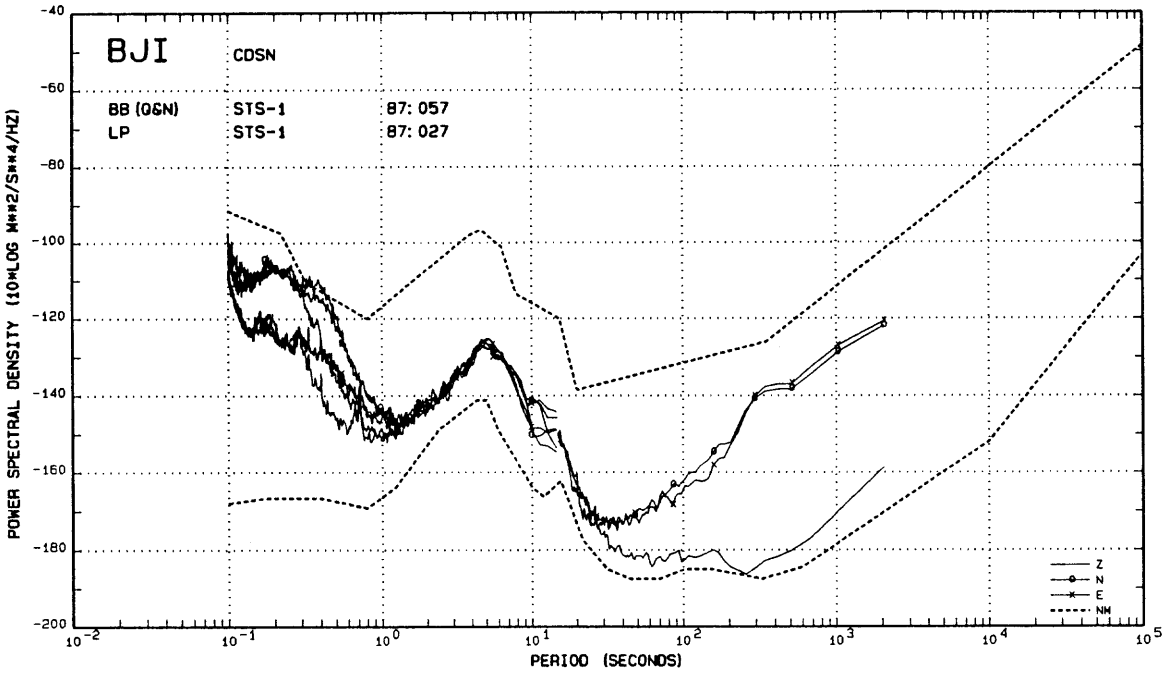

Figure A11.--BB and LP noise spectra from the Baijatuan, China CDSN station. Data shown above were obtained from the STS-1 seismometers located in a subsurface vault dug into alluvium.

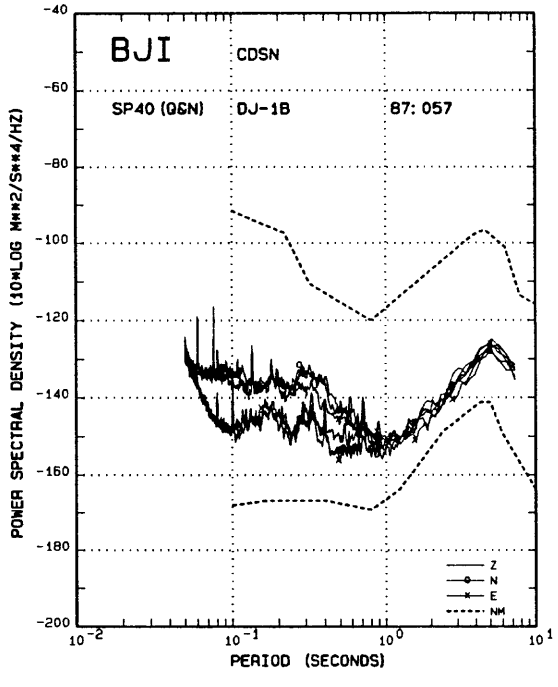

Figure A12.--BJI SP noise spectra derived from the borehole version of the DJ-1 seismometers installed in limestone at a depth of 150 meters. Noise improvement is at least 20 dB compared to the surface spectra shown in Figure A11.

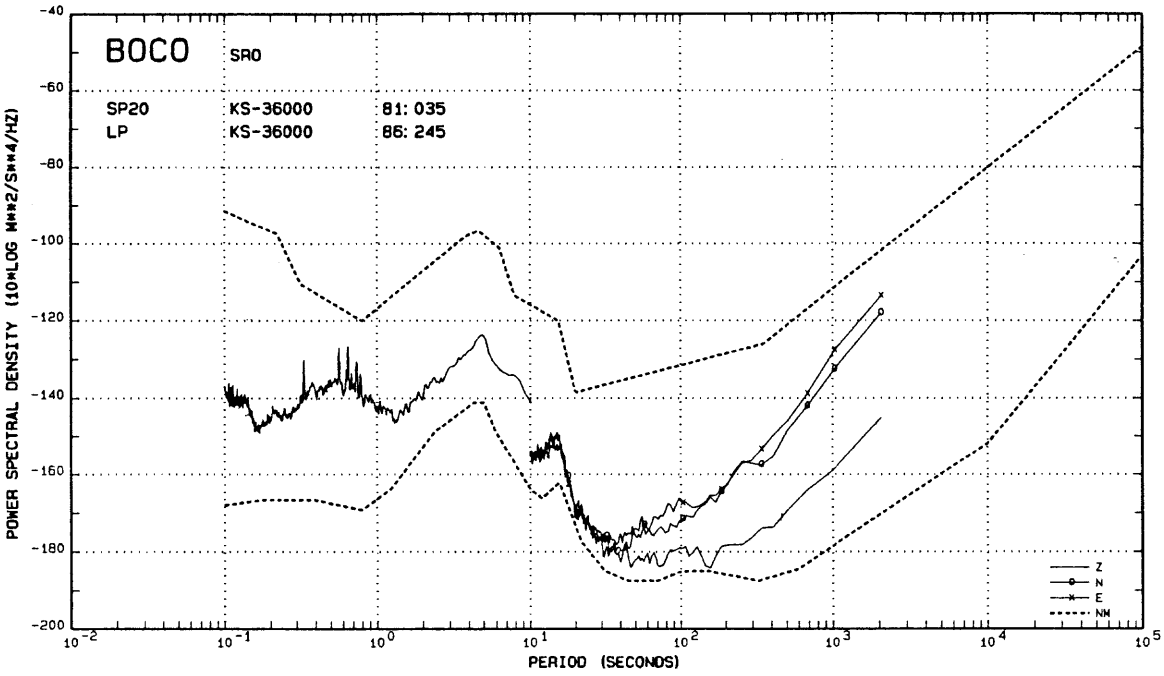

Figure A13.--Noise spectra from the Bogota, Columbia SRO station.

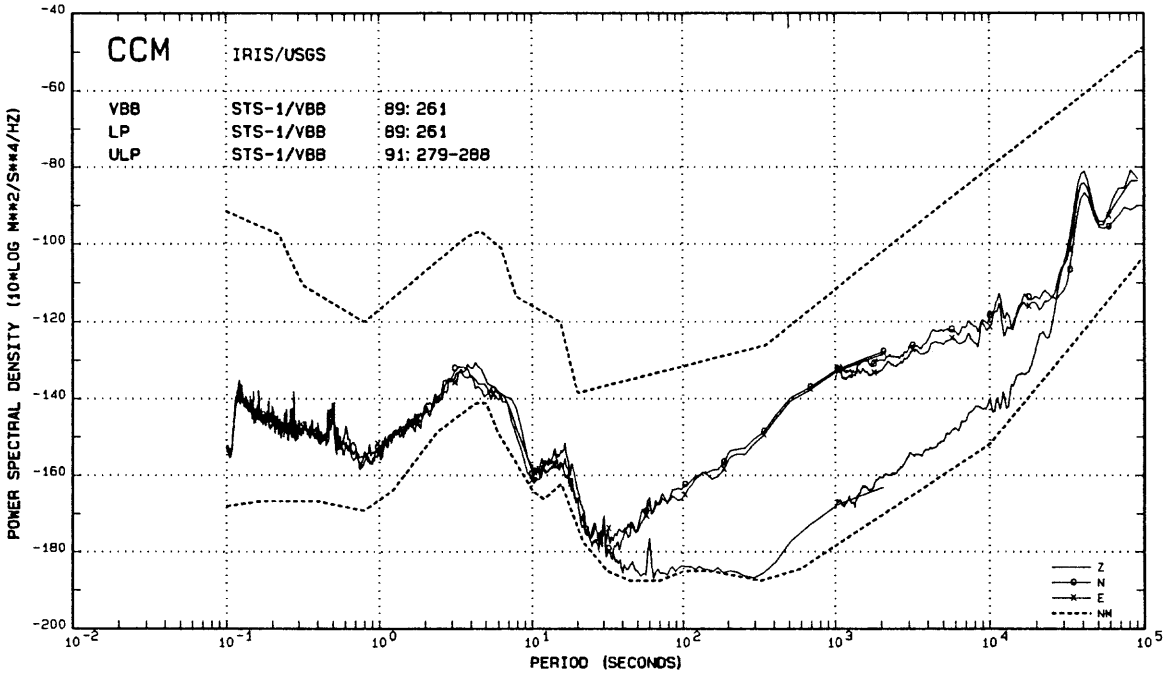

Figure A14.--Noise spectra from the Cathedral Caves, Missouri IRIS-1 station.

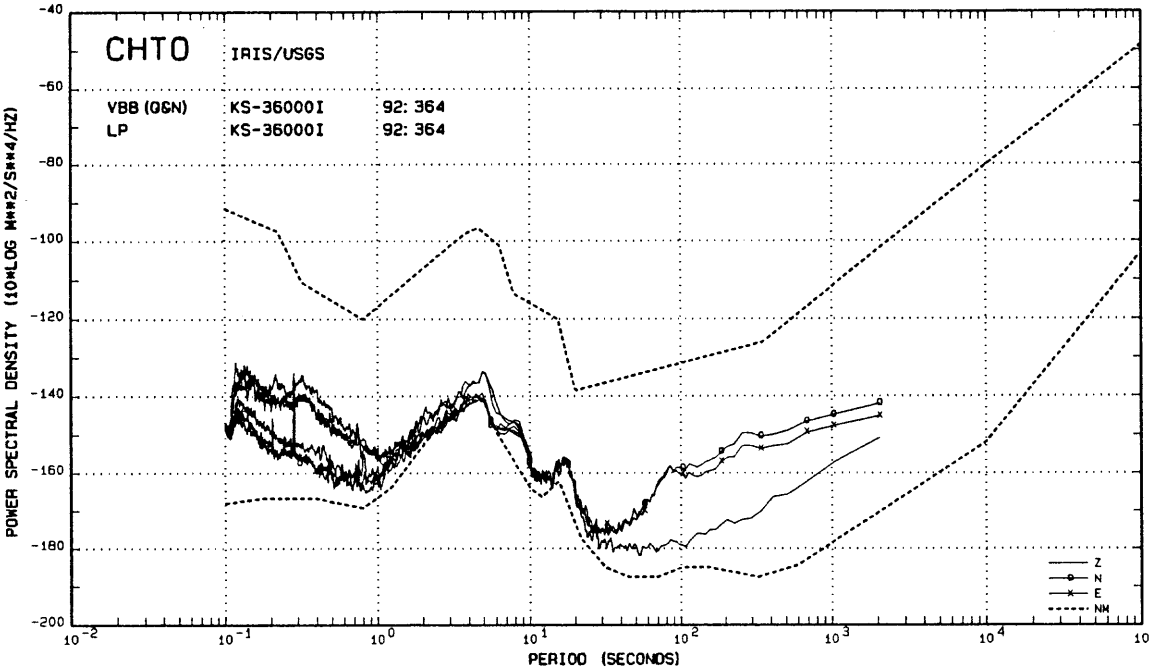

Figure A15.--Noise spectra from the Chiangmai, Thailand IRIS-2 station.

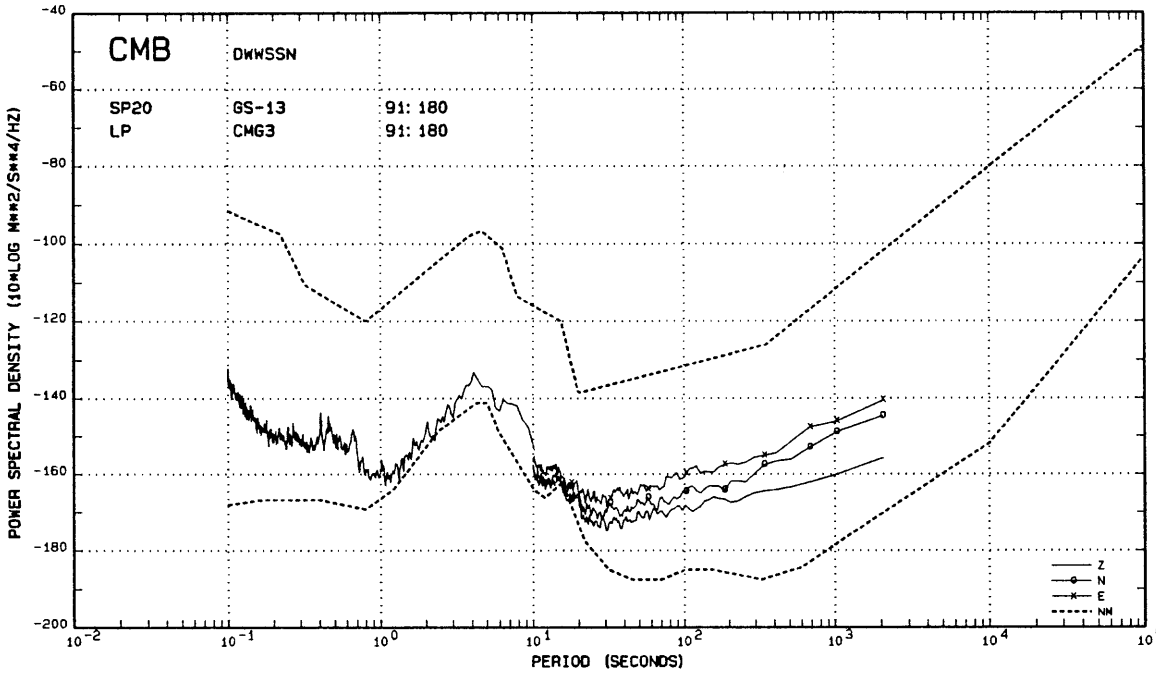

Figure A16.--Noise spectra from the Columbia College, California station.

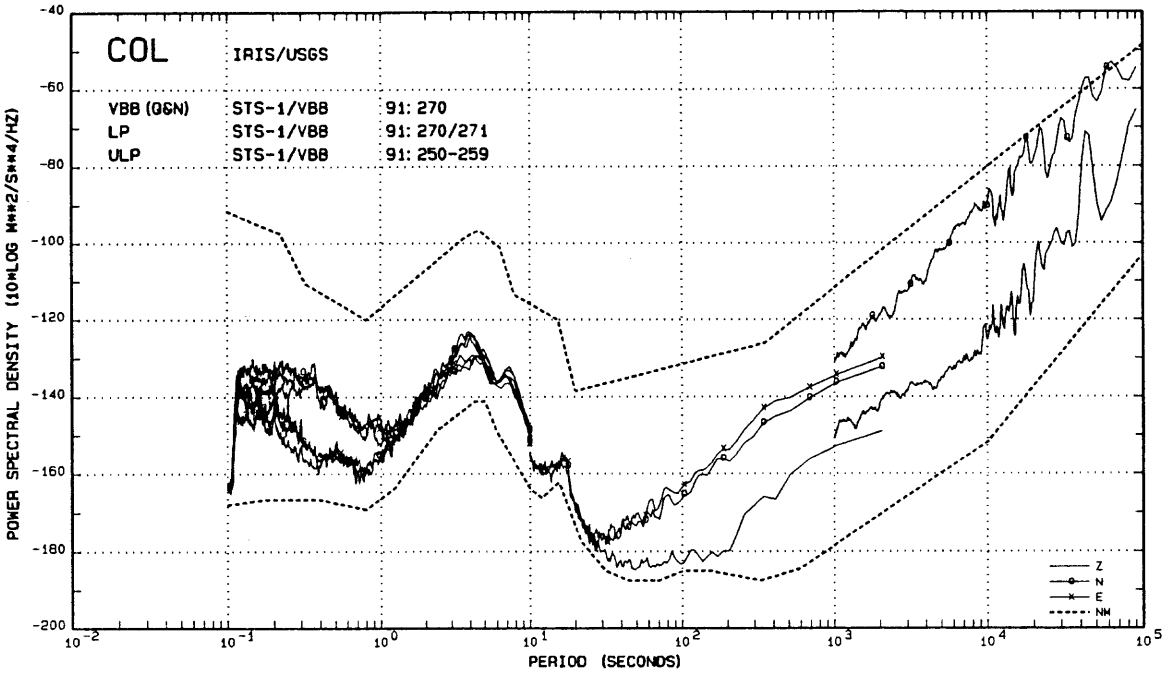

Figure A17.--Noise spectra from the College, Alaska IRIS-2 station. The high level of LP noise in the vertical component at 1000 sec suggests temperature cycling.

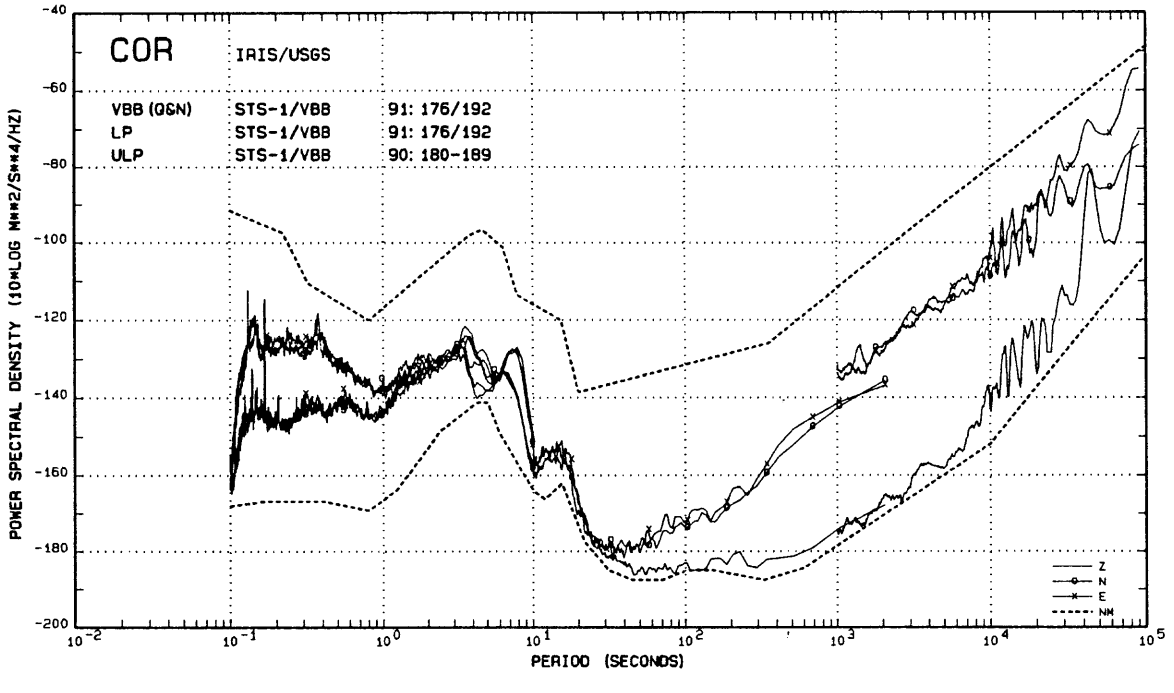

Figure A18.--Noise spectra from the Corvallis, Oregon IRIS-1 station.

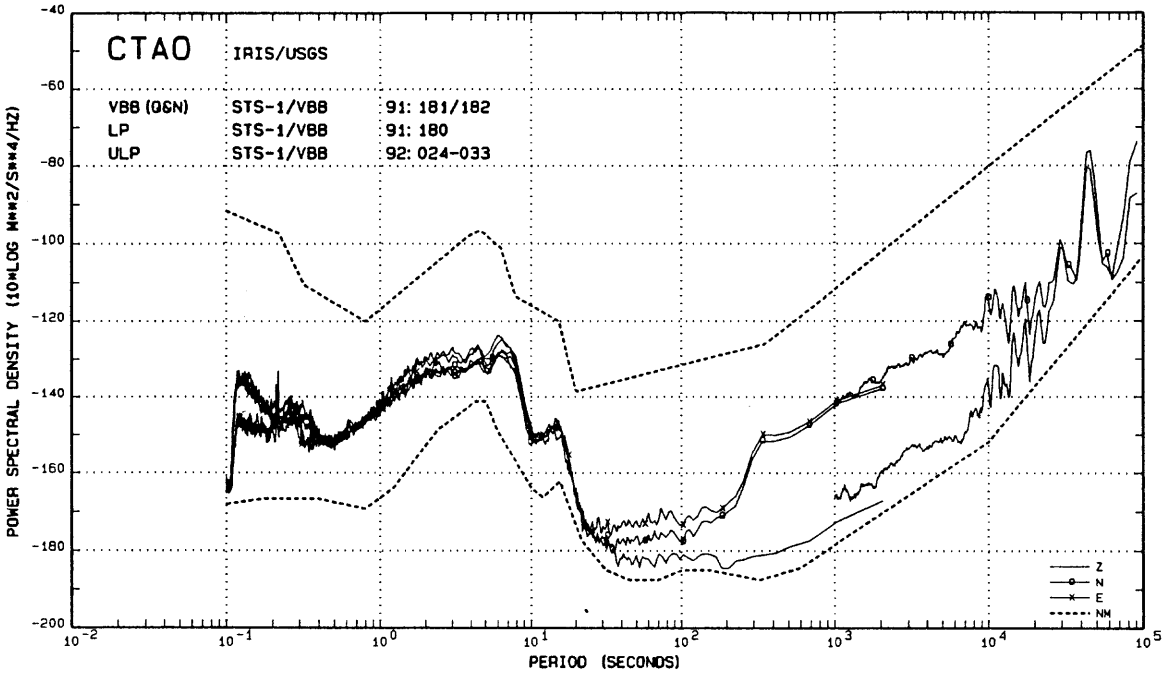

Figure A19.--Noise spectra from the Charters Towers, Australia IRIS-2 station.

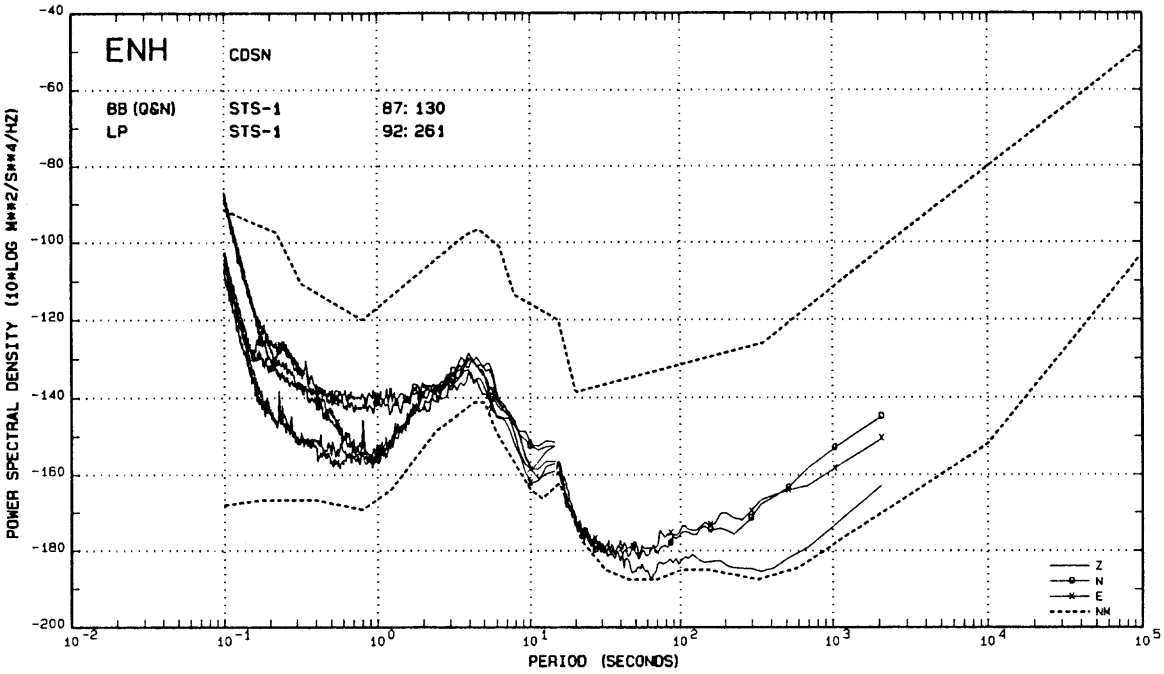

Figure A20.--BB and LP noise spectra from the Enshi, China CDSN station.

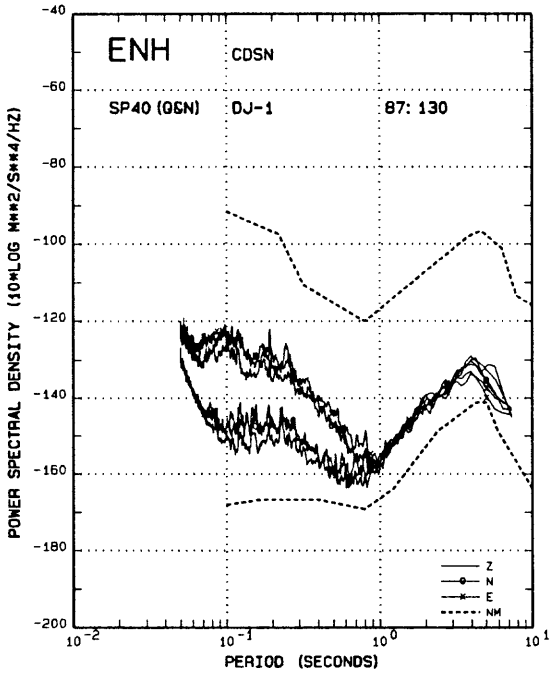

Figure A21.--SP noise spectra from the Enshi station.

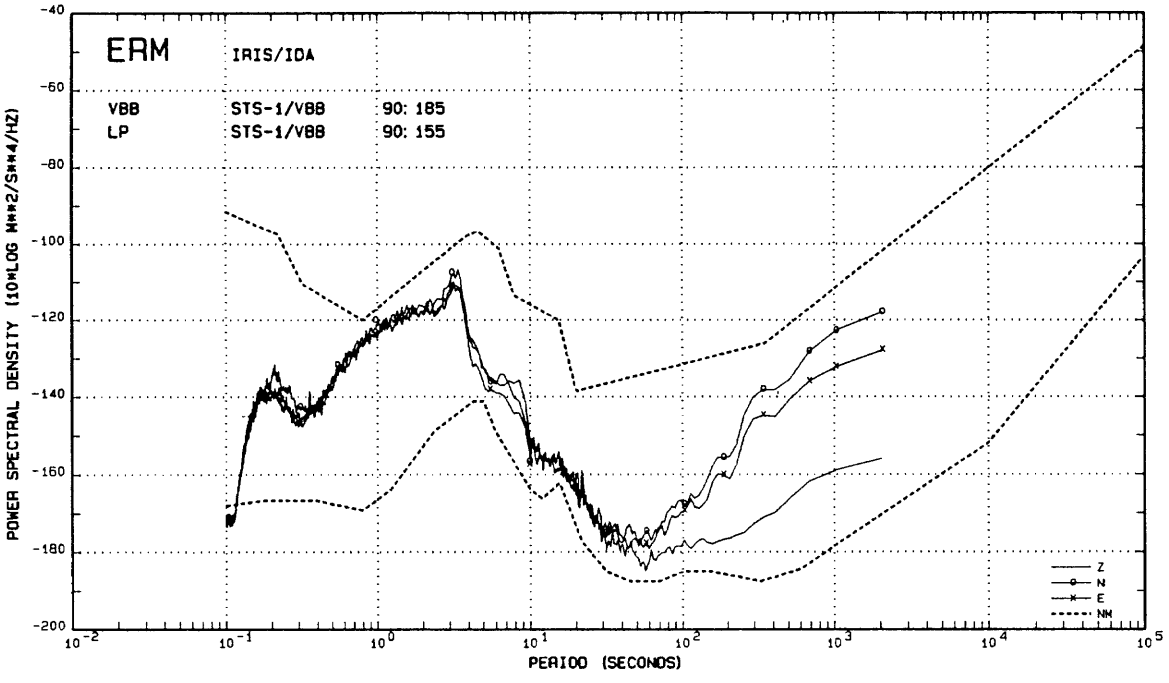

Figure A22.--Noise spectra from the Erimo, Japan IRIS/IDA station.

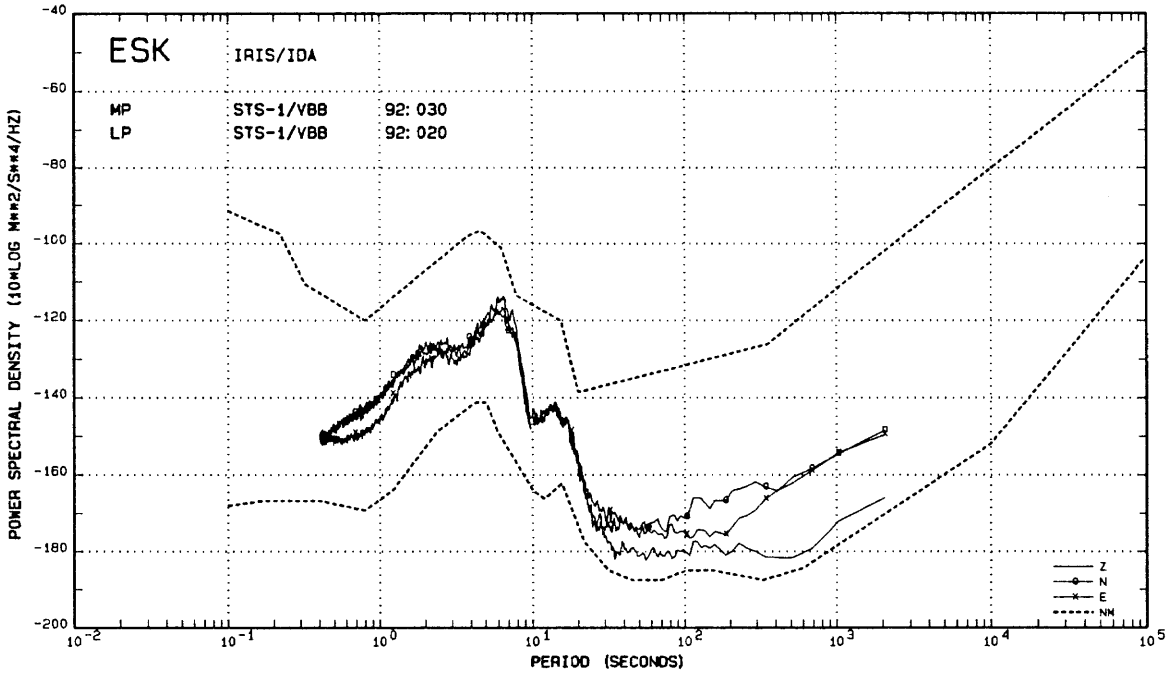

Figure A23.--Noise spectra from the Eskdalemuir, Scotland IRIS/IDA station.

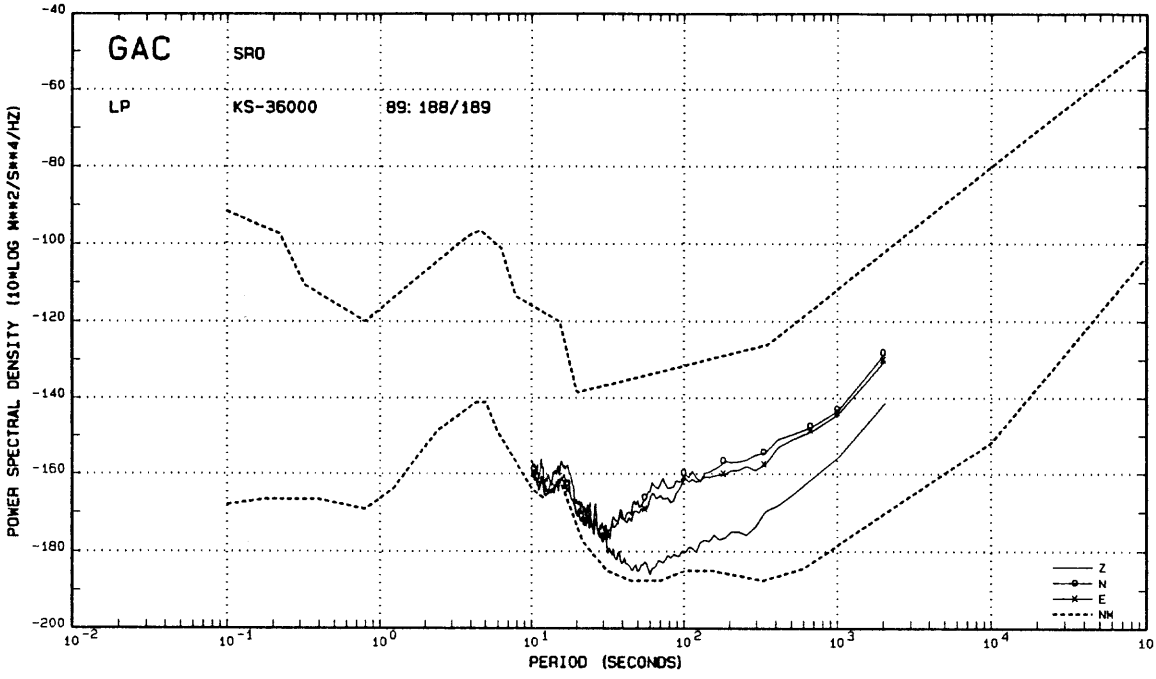

Figure A24.--Noise spectra from the Glen Almond, Canada station. Only LP data are recorded on this SRO-type system.

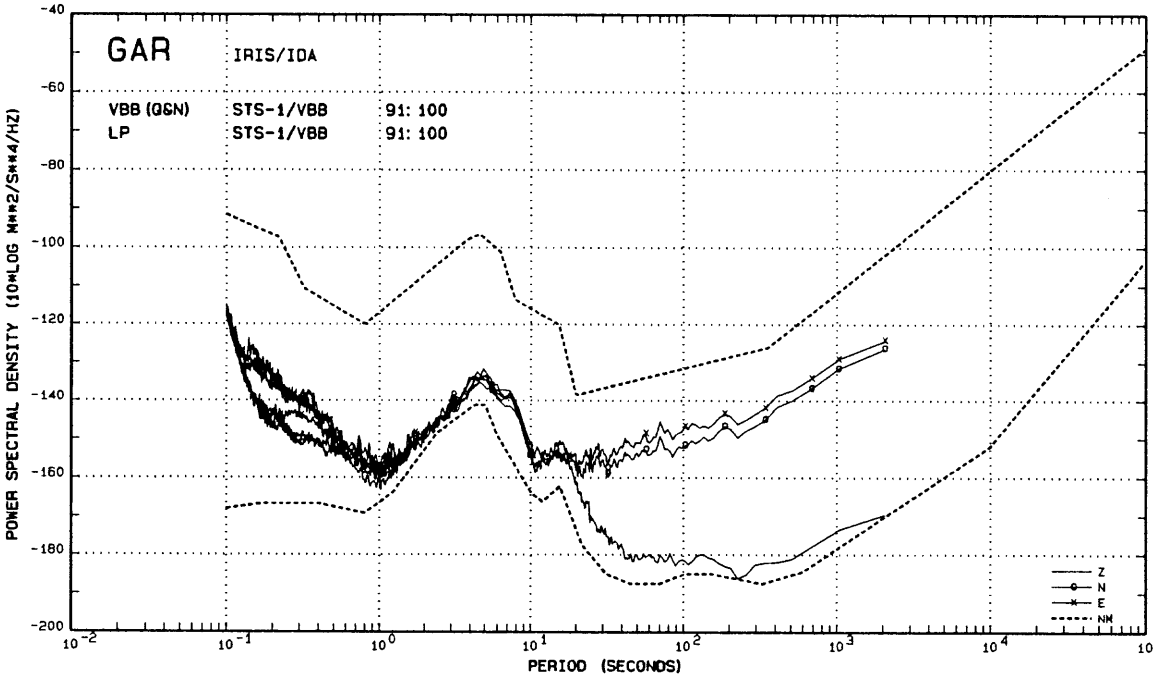

Figure A25.--Noise spectra from the Garm, Tajikistan IRIS/IDA station.

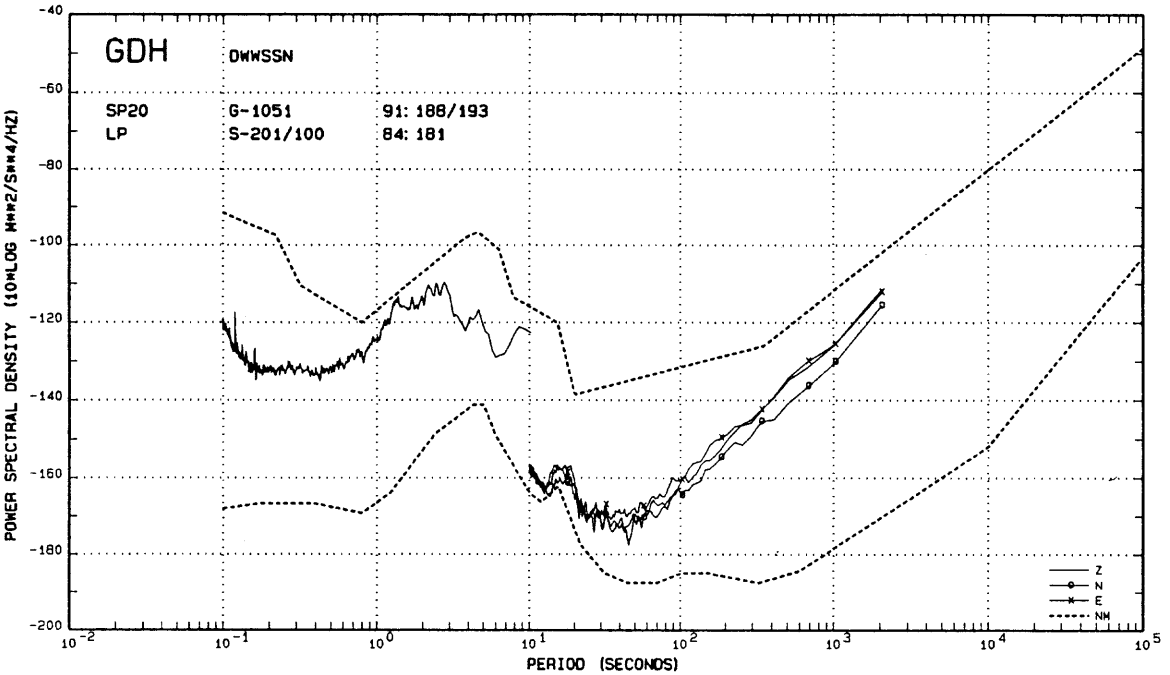

Figure A26.--Noise Spectra from the Godhavn, Greenland DWWSSN station.

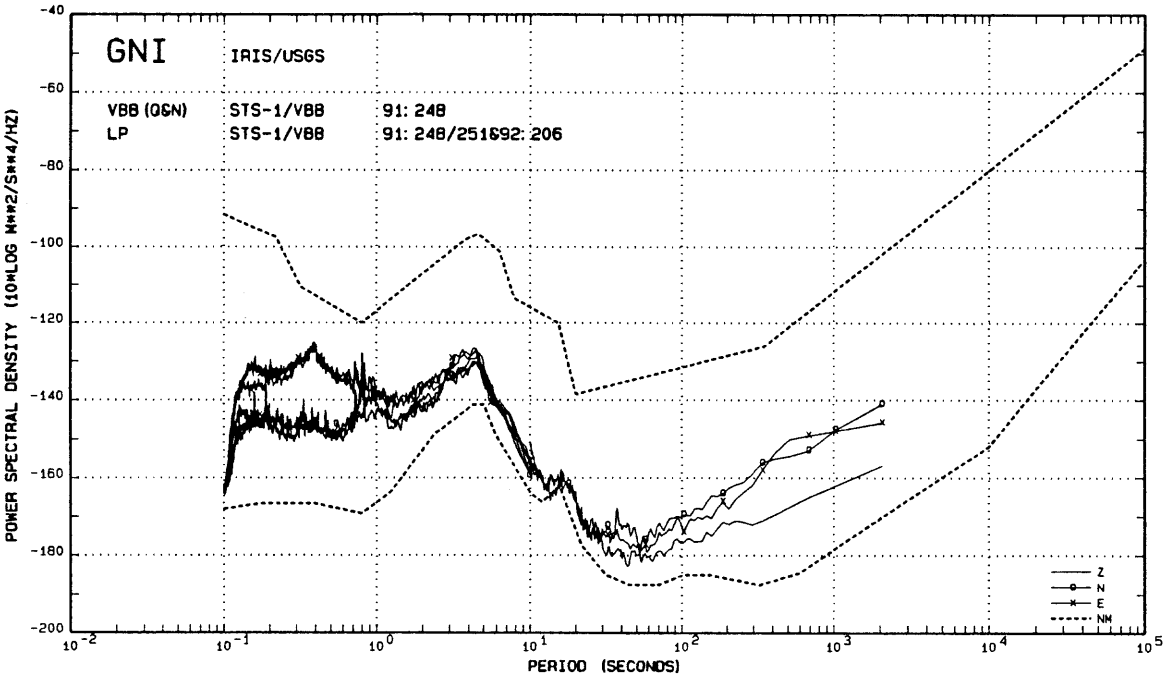

Figure A27.--VBB and LP noise spectra from the Garni, Armenia IRIS-2 station.

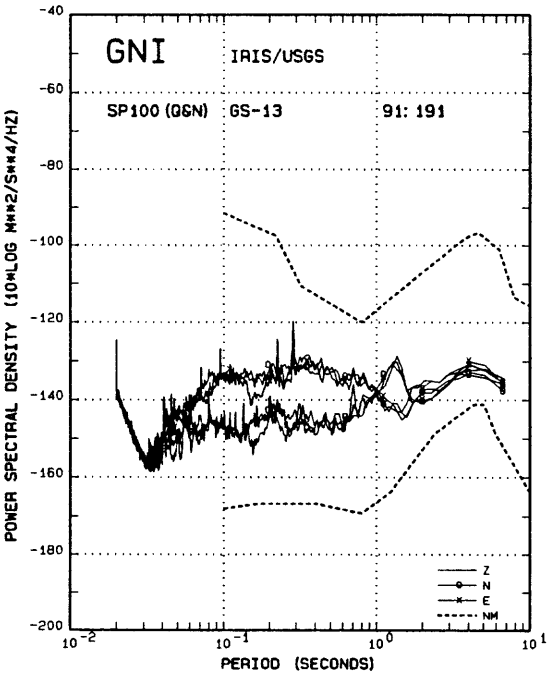

Figure A28.--SP noise spectra from Garni. The peak at 1.3 seconds in the noisy data set is intermittent, probably caused by lake-generated microseisms.

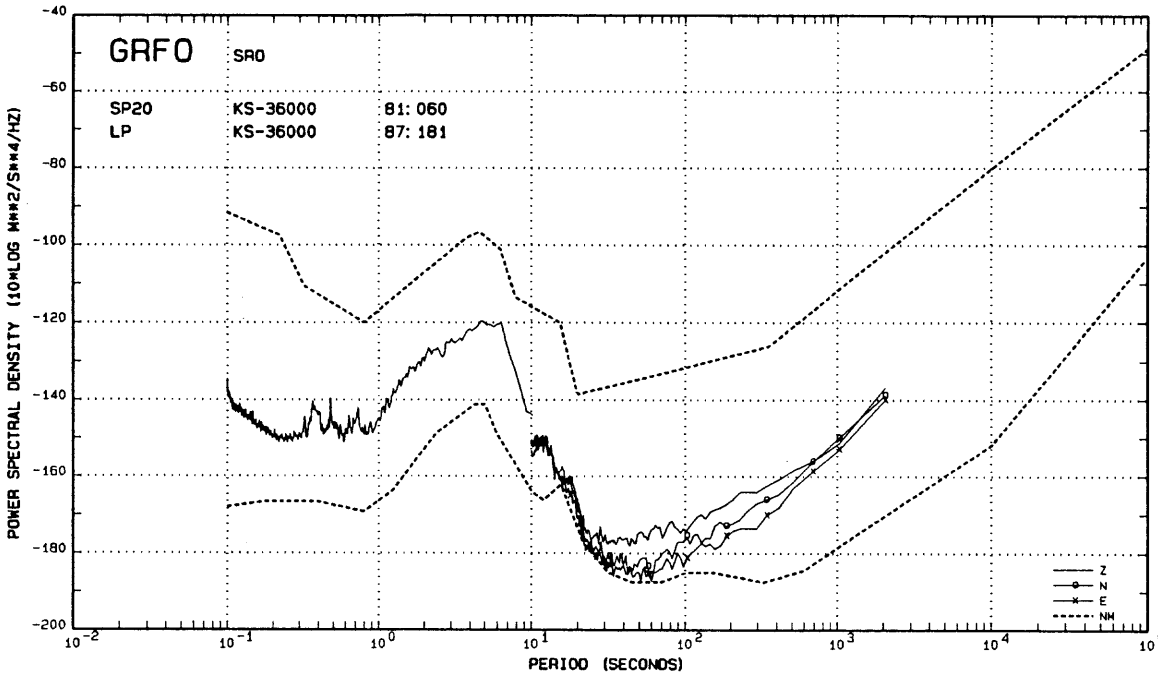

Figure A29.--Noise spectra from the Grafenburg, Germany SRO station.

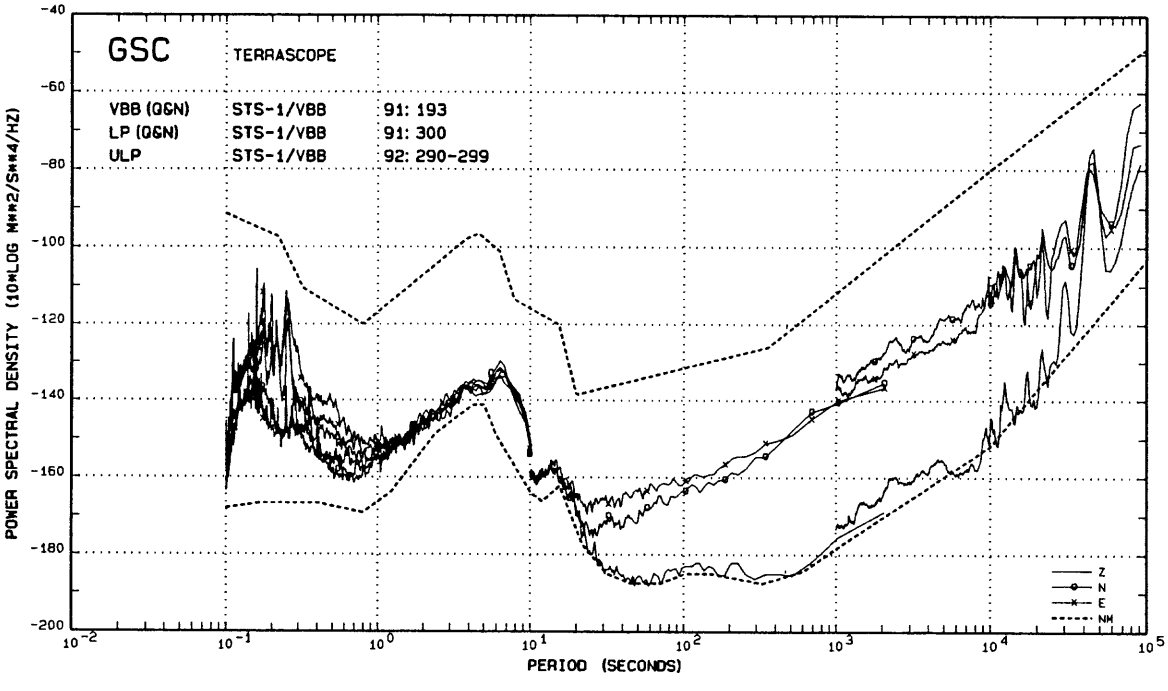

Figure A30.--Noise spectra from the Goldstone, California TERRAscope station.

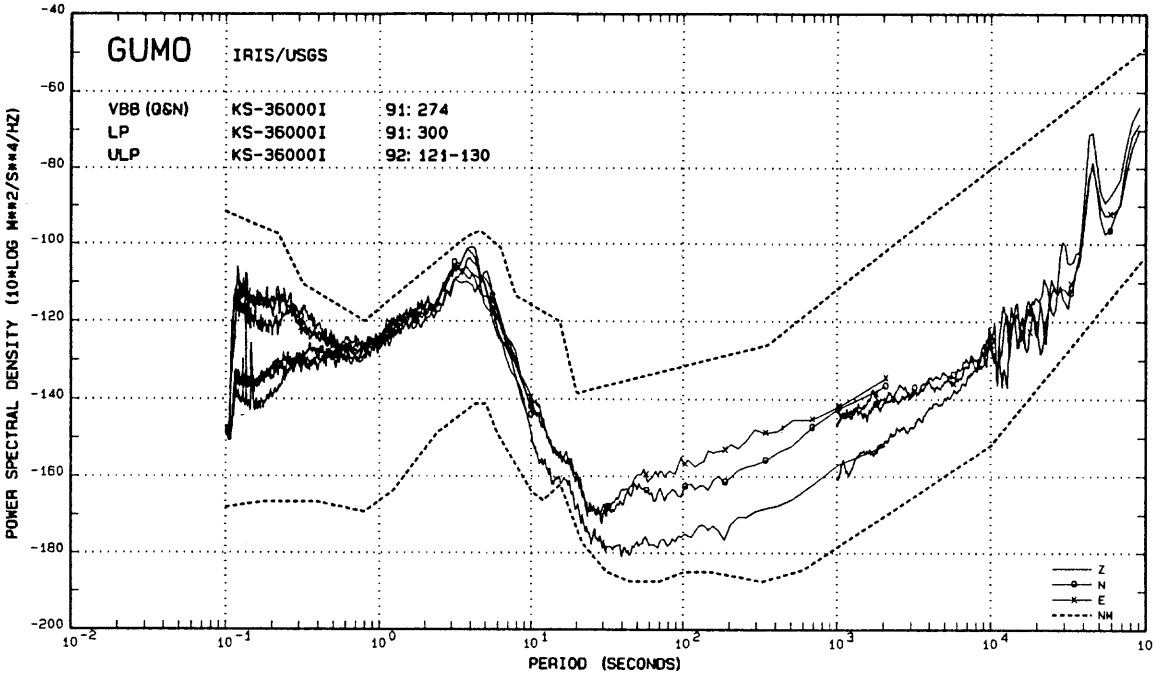

Figure A31.--Noise spectra from the Guam IRIS-2 station.

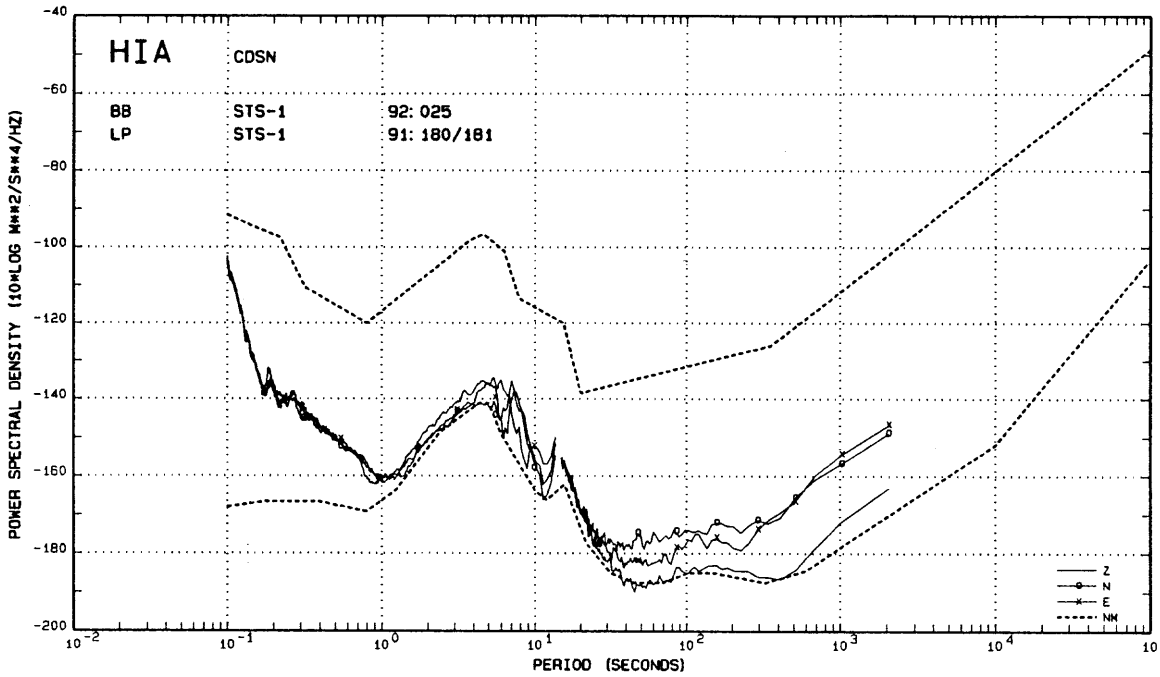

Figure A32.--BB and LP noise spectra from the Hailar, China CDSN station.

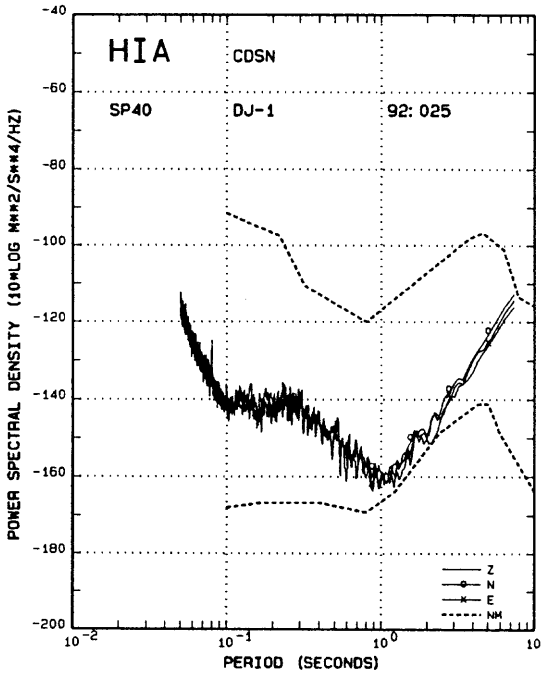

Figure A33.--SP noise spectra from the Hailar station.

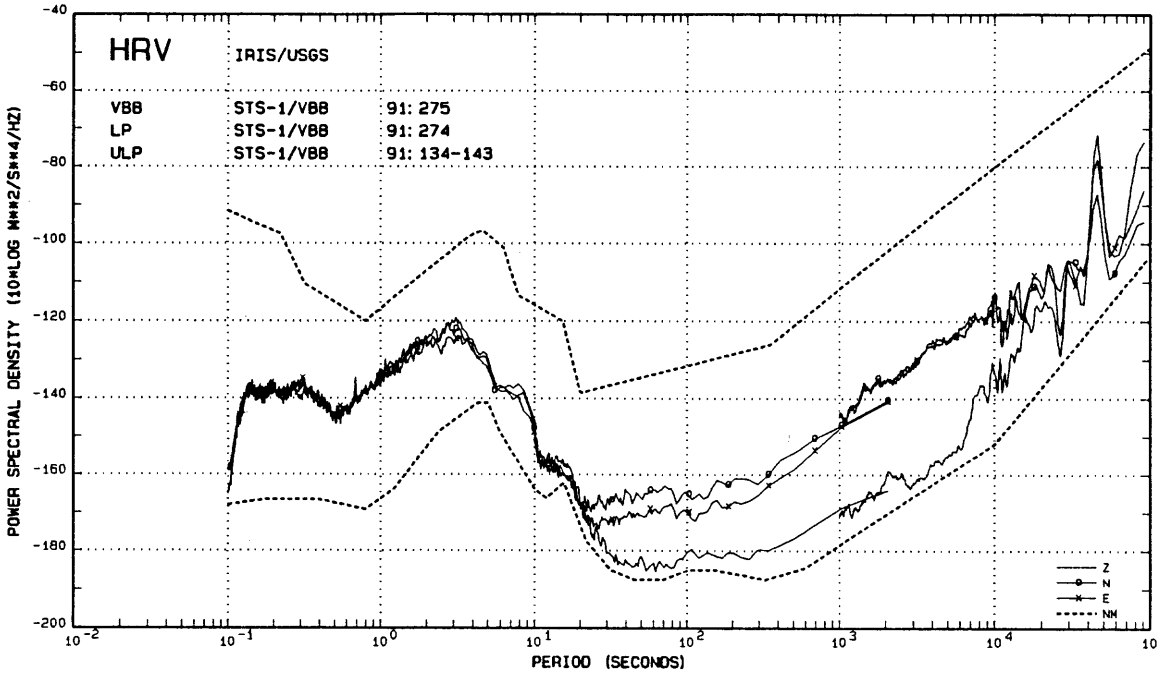

Figure A34.--Noise spectra from the Harvard, Massachusetts IRIS-1 station.

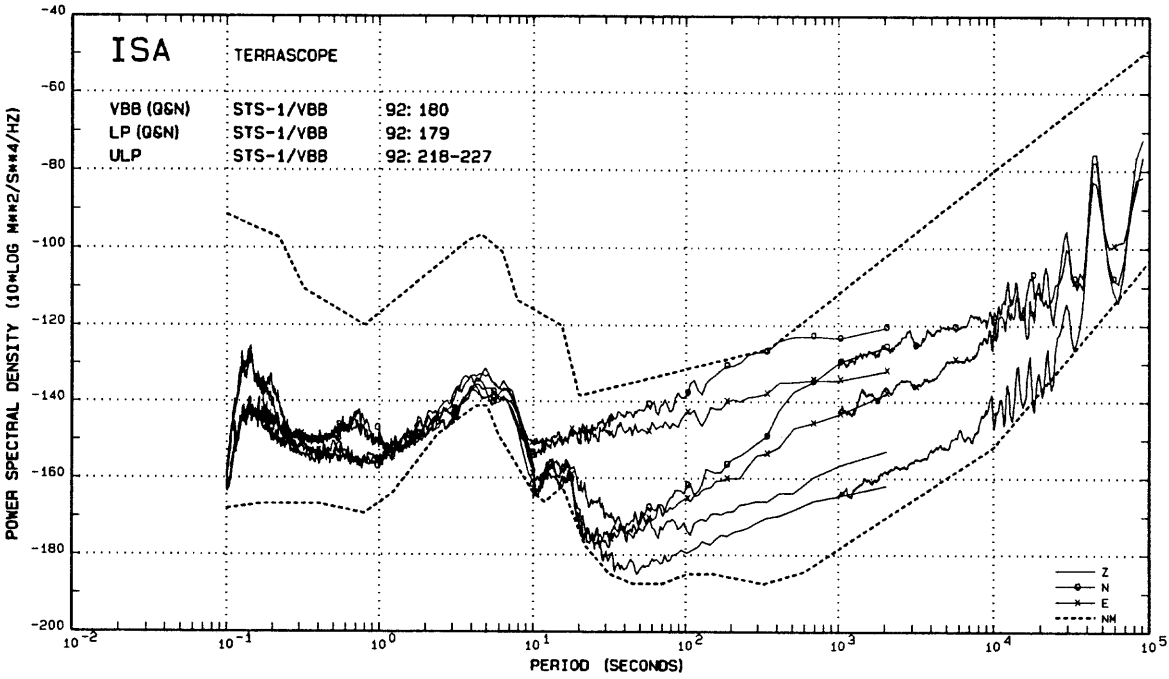

Figure A35.--Noise spectra from the Isabella, California TERRAscope station. Both quiet and noisy LP spectra are shown.

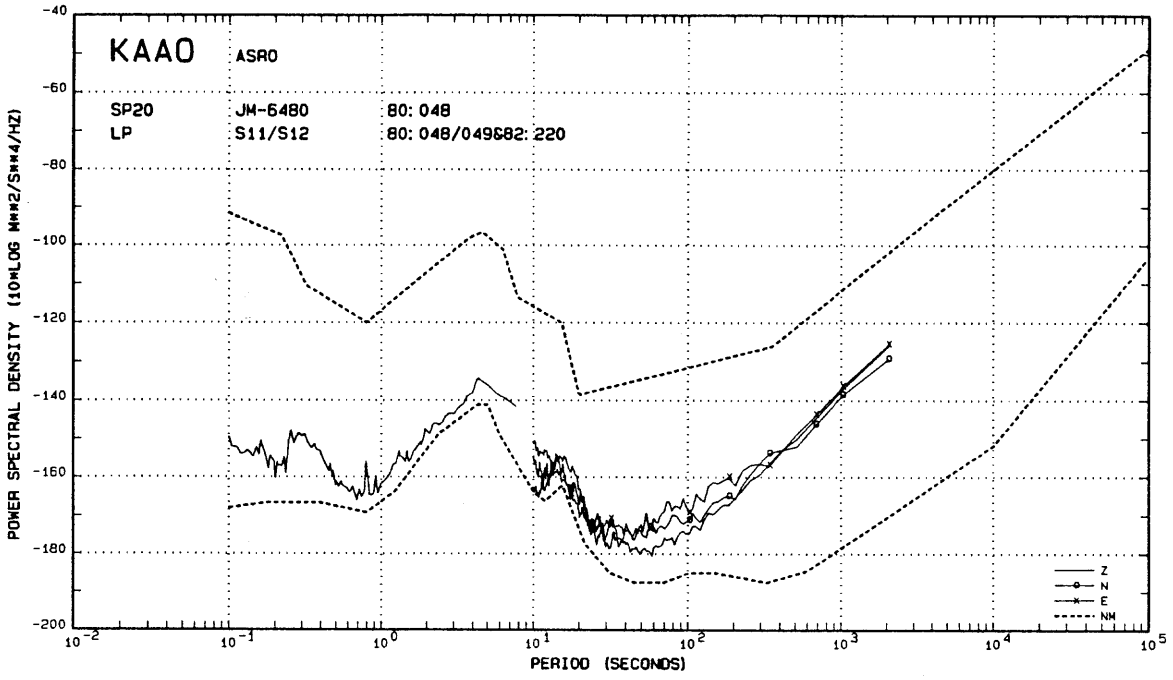

Figure A36.--Noise spectra from the Kabul, Afghanistan ASRO station. The ASRO system is no longer in operation. The SP20 spectra were adopted from a previous report (Peterson, 1980).

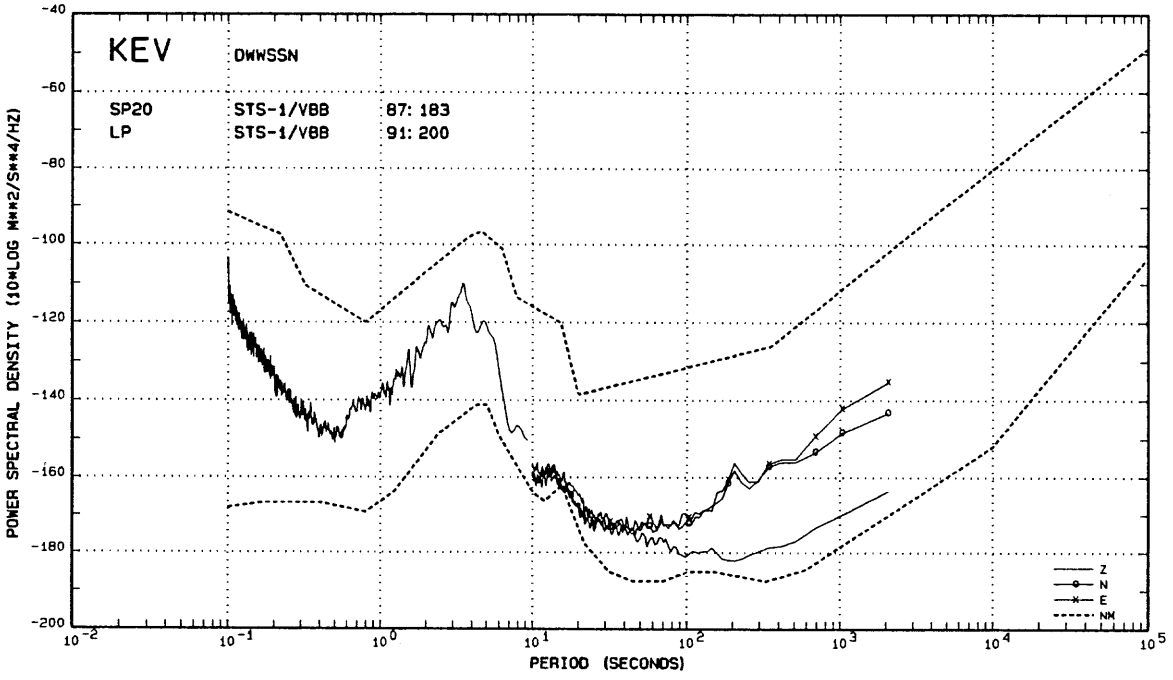

Figure A37.--Noise spectra from the Kevo, Finland DWWSSN station that has been equipped with STS-1/VBB seismometers.

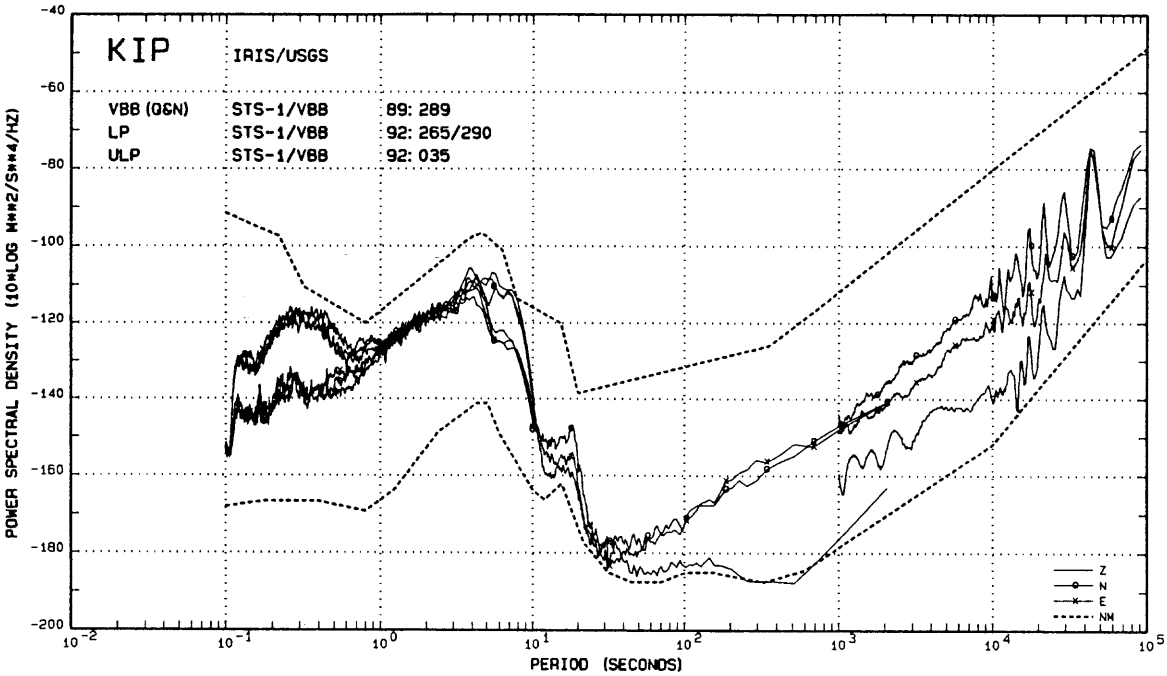

Figure A38.--VBB, LP, and ULP noise spectra from the Kipapa, Hawaii IRIS-2 station.

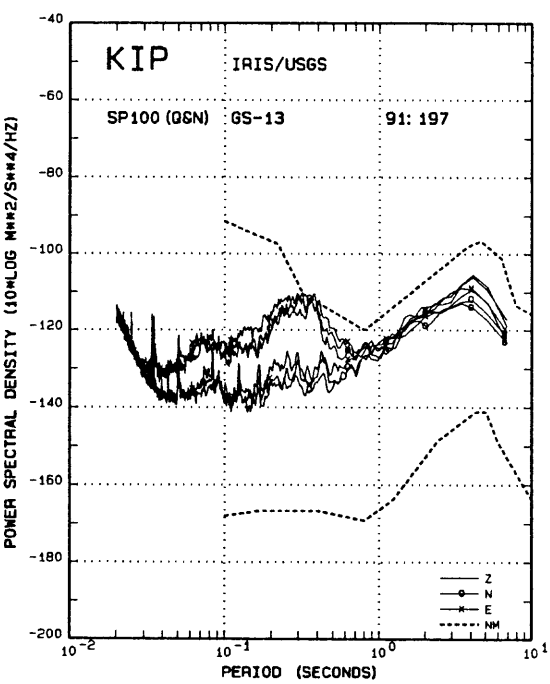

Figure A39.--SP noise spectra from the Kipapa station.

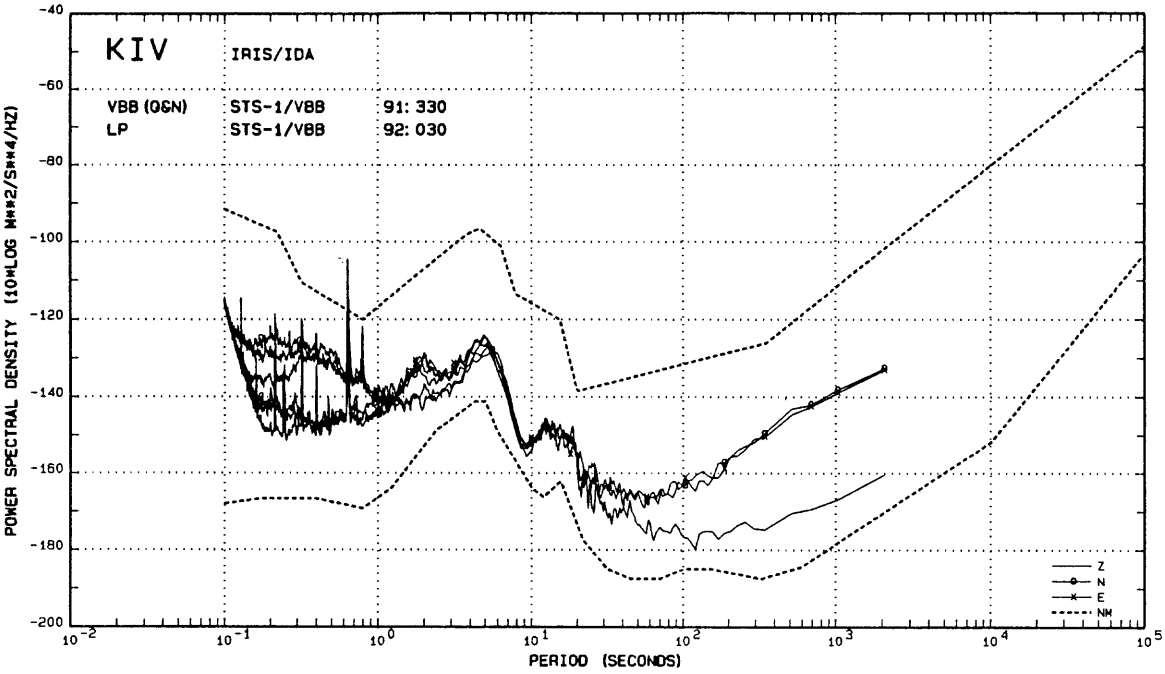

Figure A40.--Noise spectra from the Kislovodsk, Russia IRIS/IDA station.

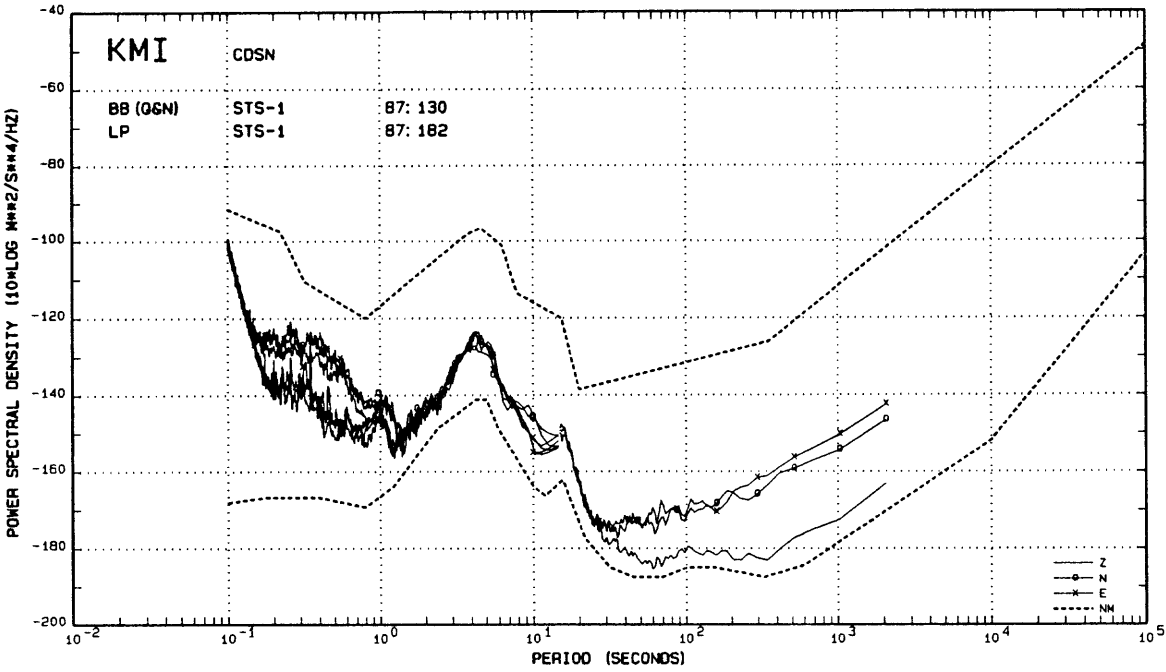

Figure A41.--BB and LP noise spectra from the Kunming, China CDSN station.

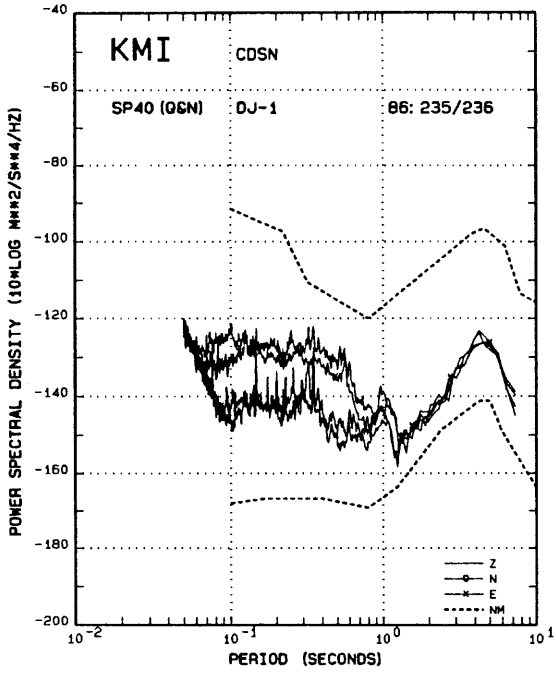

Figure A42.--SP noise spectra from the Kunming station.

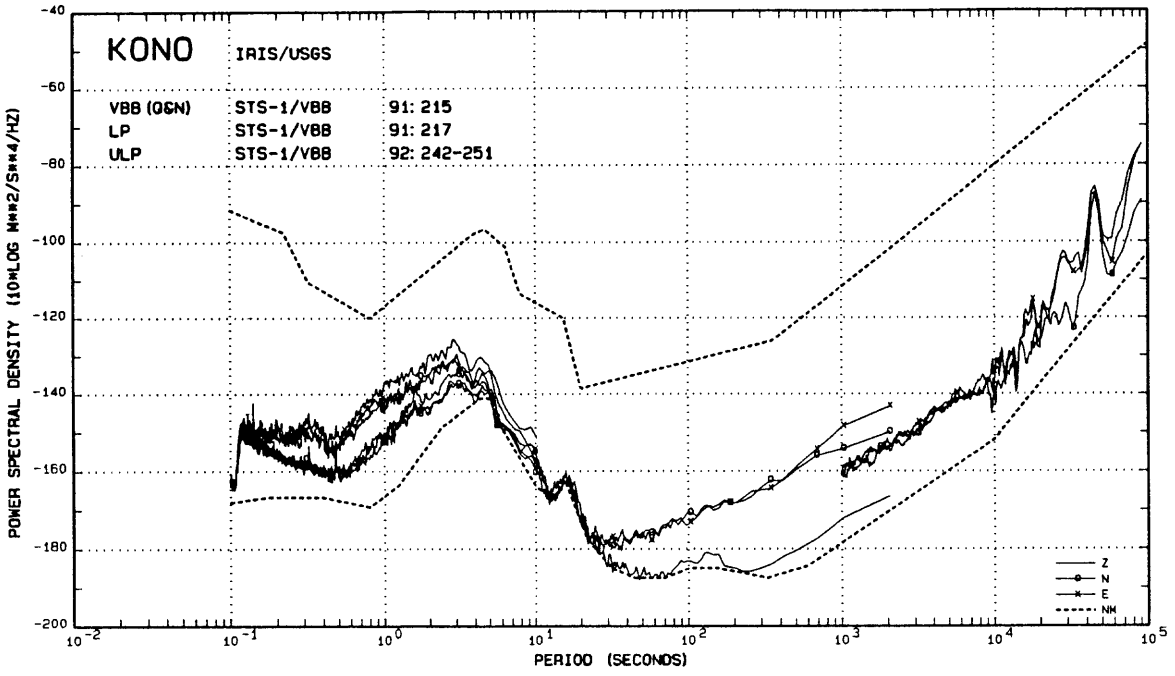

Figure A43.--Noise spectra from the Kongsberg, Norway IRIS-2 station.

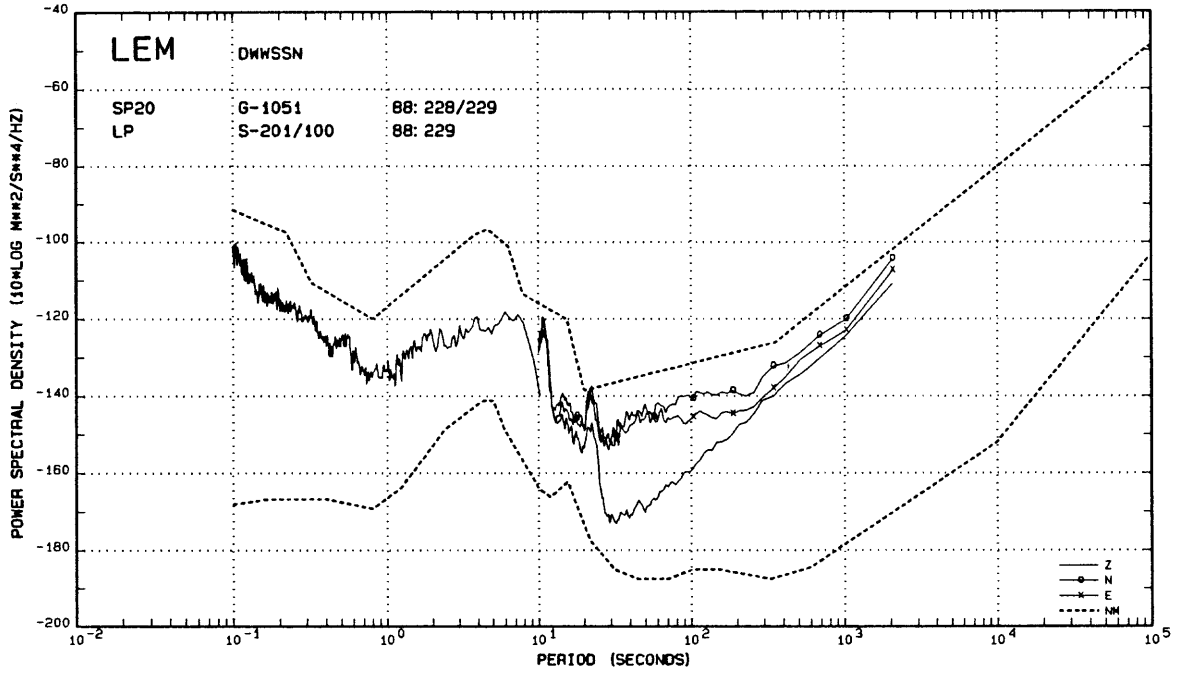

Figure A44.--Noise spectra from the Lembang, Indonesia DWWSSN station.

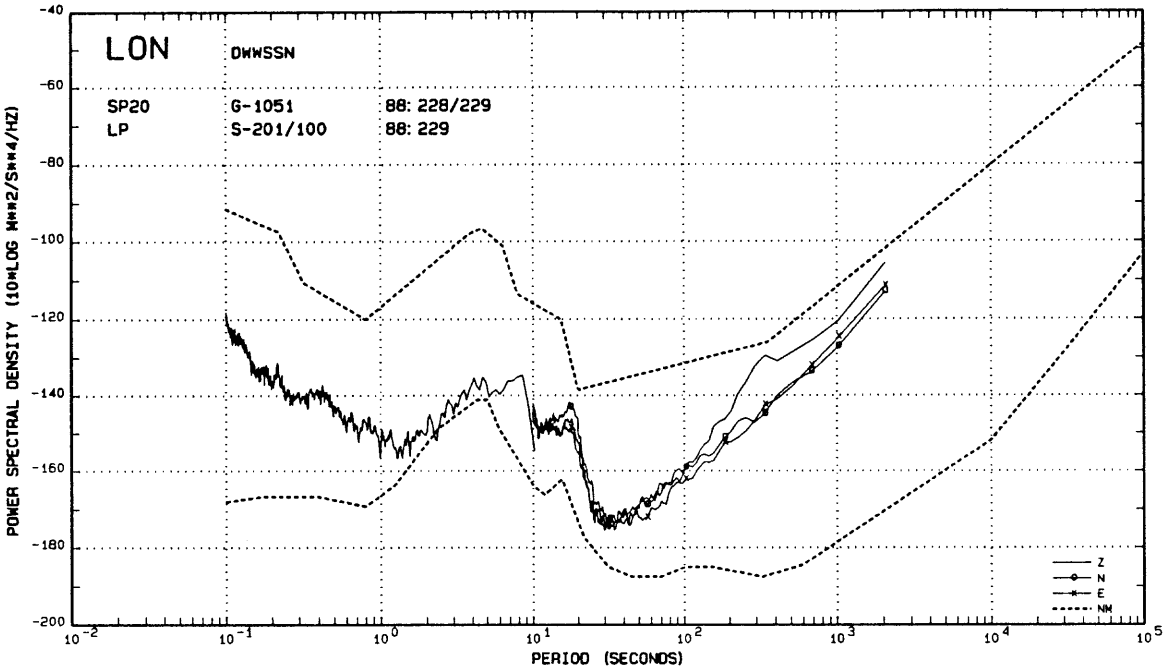

Figure A45.--Noise spectra from the Longmire, Washington DWWSSN station.

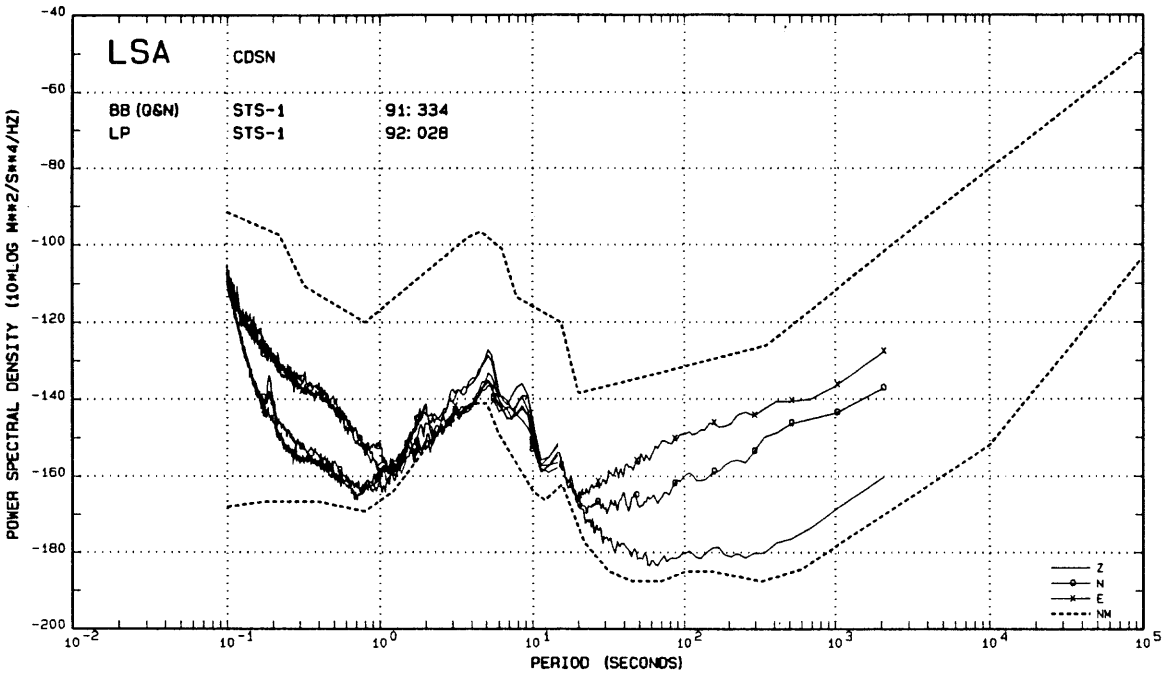

Figure A46.--BB and LP noise spectra from the Lhasa, Tibet CDSN station.

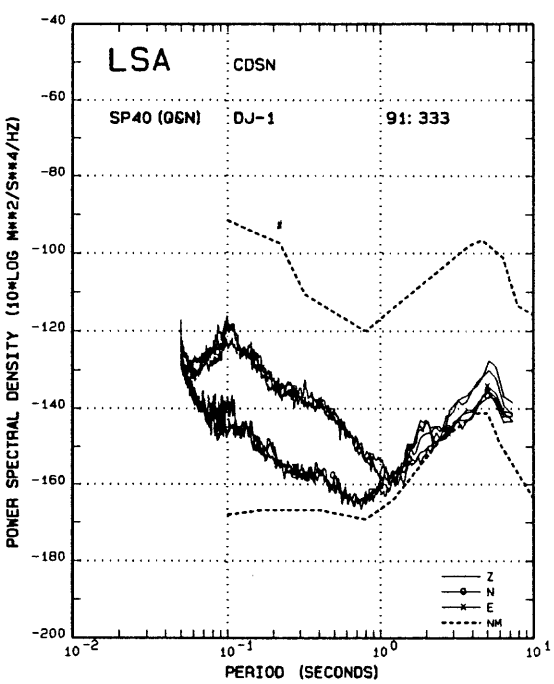

Figure A47.--SP noise spectra from the Lhasa station.

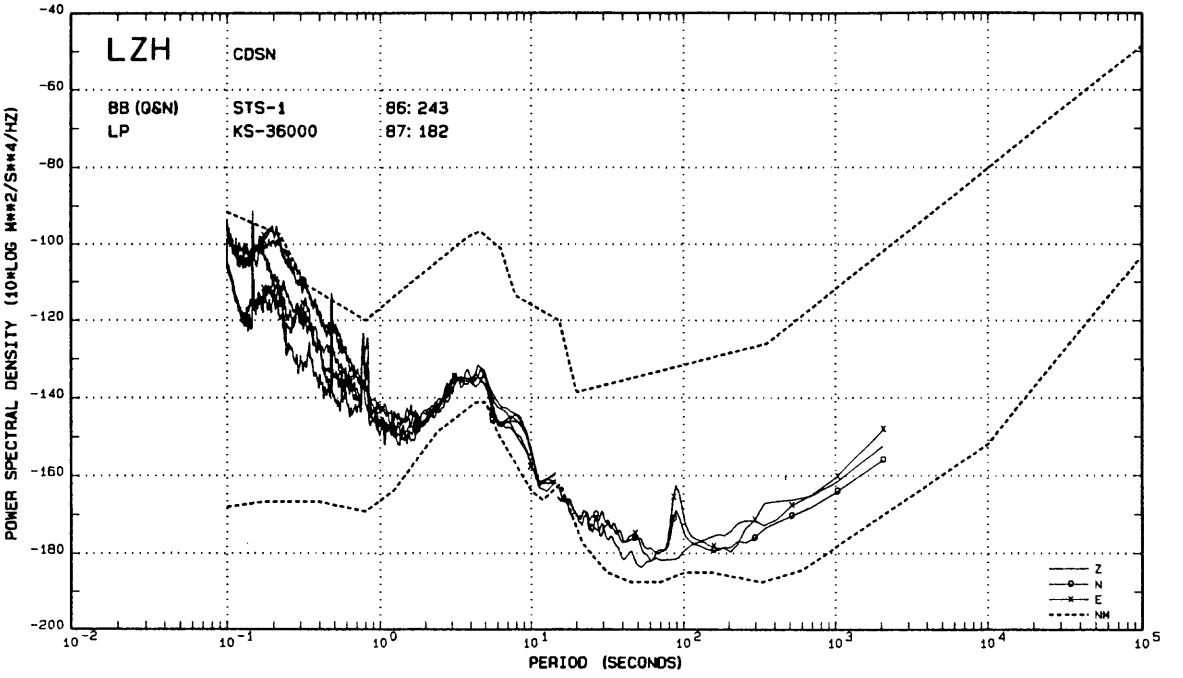

Figure A48--Noise spectra from the Lanzhou, China CDSN station. BB signals are obtained from STS-1 seismometers located in a surface vault, LP signals from a KS-36000 borehole seismometer.

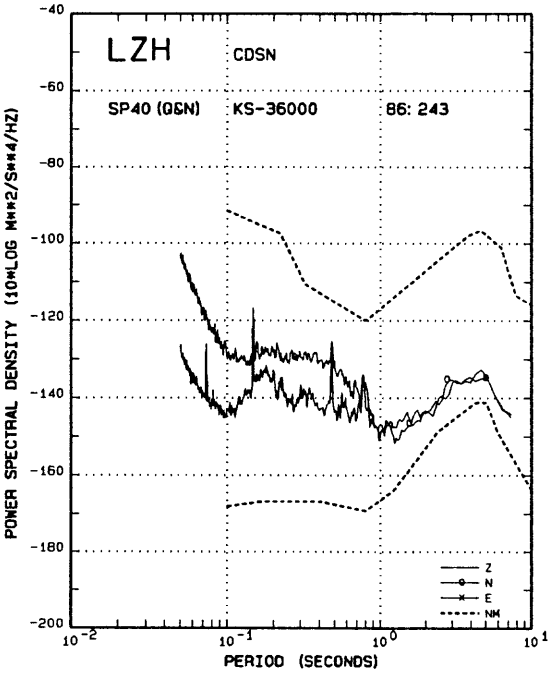

Figure A49.--SP noise spectra from the Lanzhou borehole seismometer installed at 120 meters in sandstone. There is 20 dB of noise improvement compared to the BB signals shown in Figure A48.

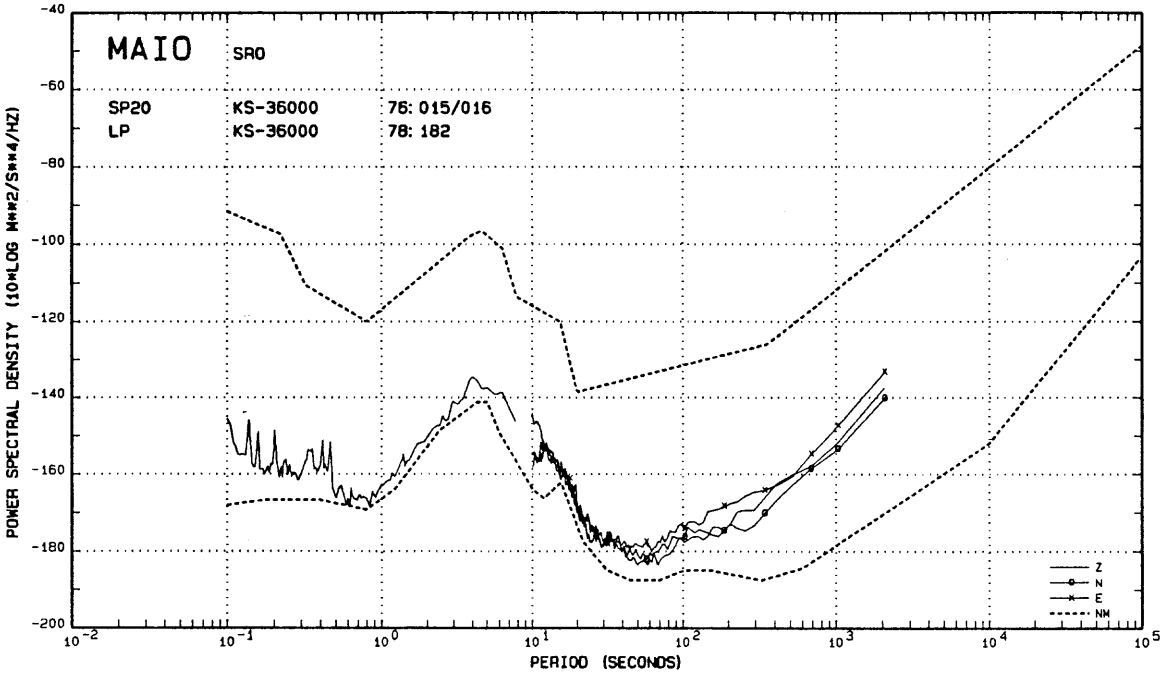

Figure A50.--Noise spectra from the Mashhad, Iran SRO station. The SRO system is no longer in operation. The SP20 spectra were adopted from a previous report (Peterson, 1980).

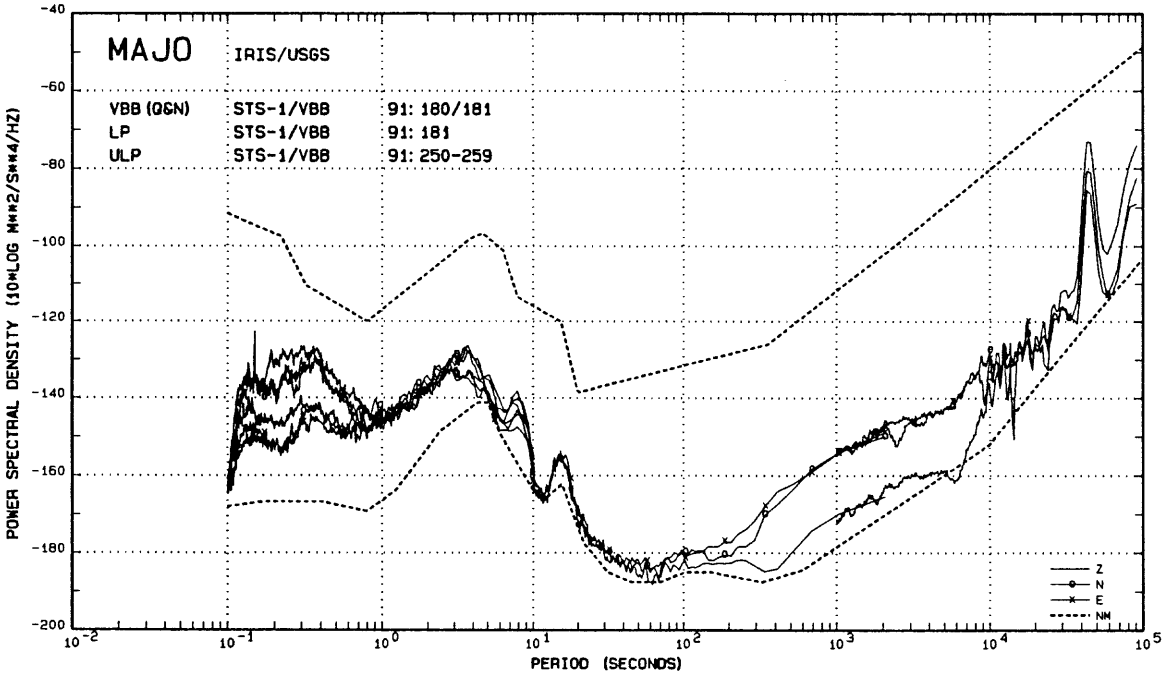

Figure A51.--Noise spectra from the Matsushiro, Japan IRIS-2 station.

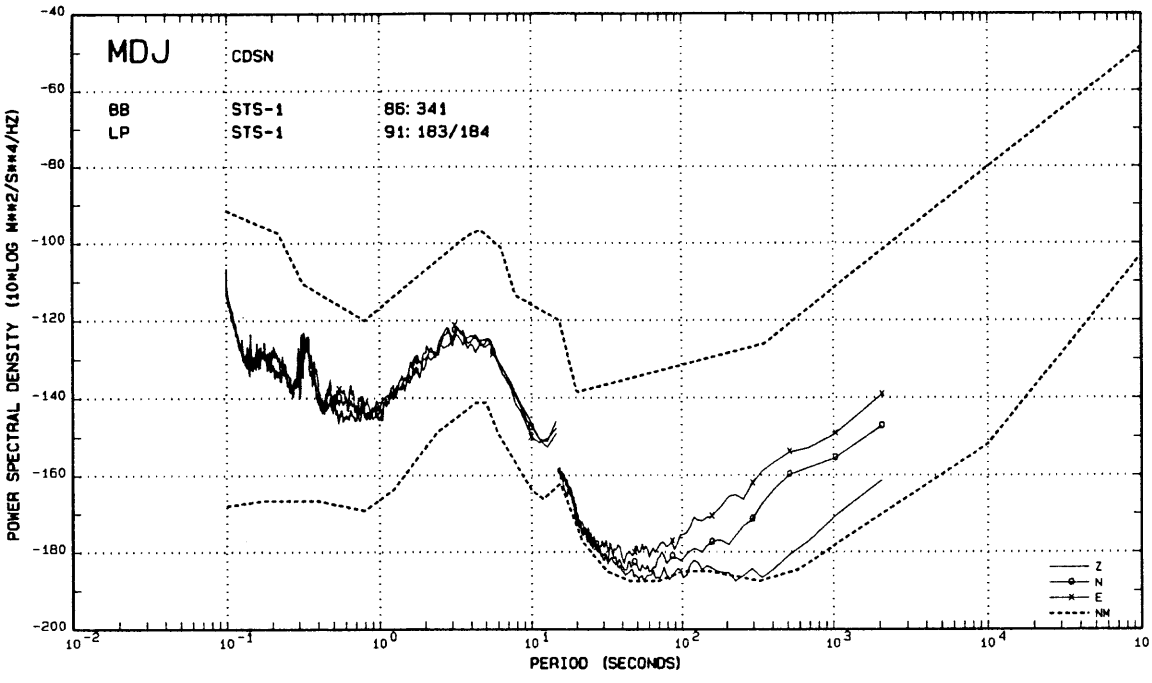

Figure A52.--BB and LP noise spectra from the Mudanjiang, China CDSN station.

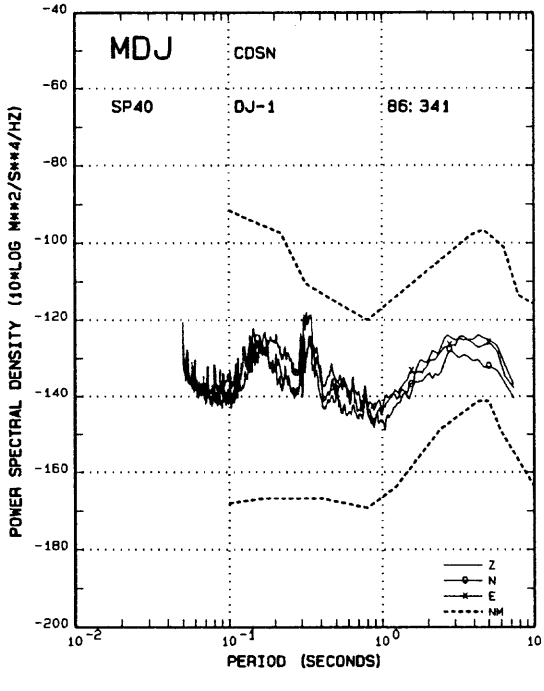

Figure A53.--SP noise spectra from the Mudanjiang station.

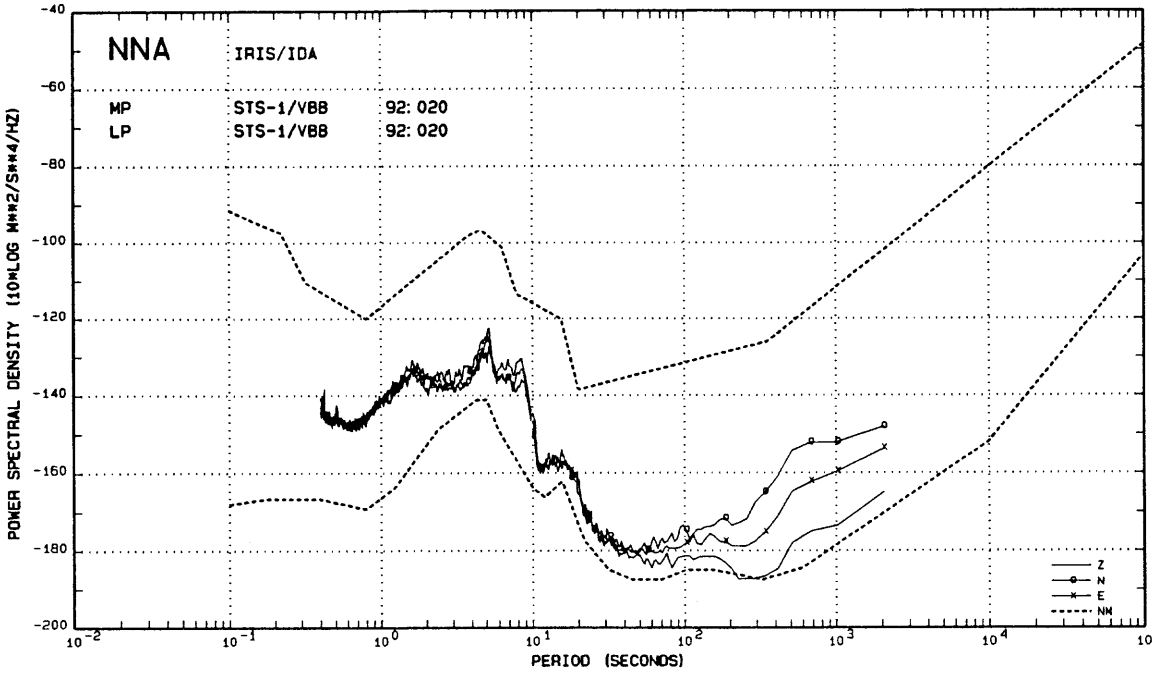

Figure A54.--Noise spectra from the Nana, Peru IRIS/IDA station.

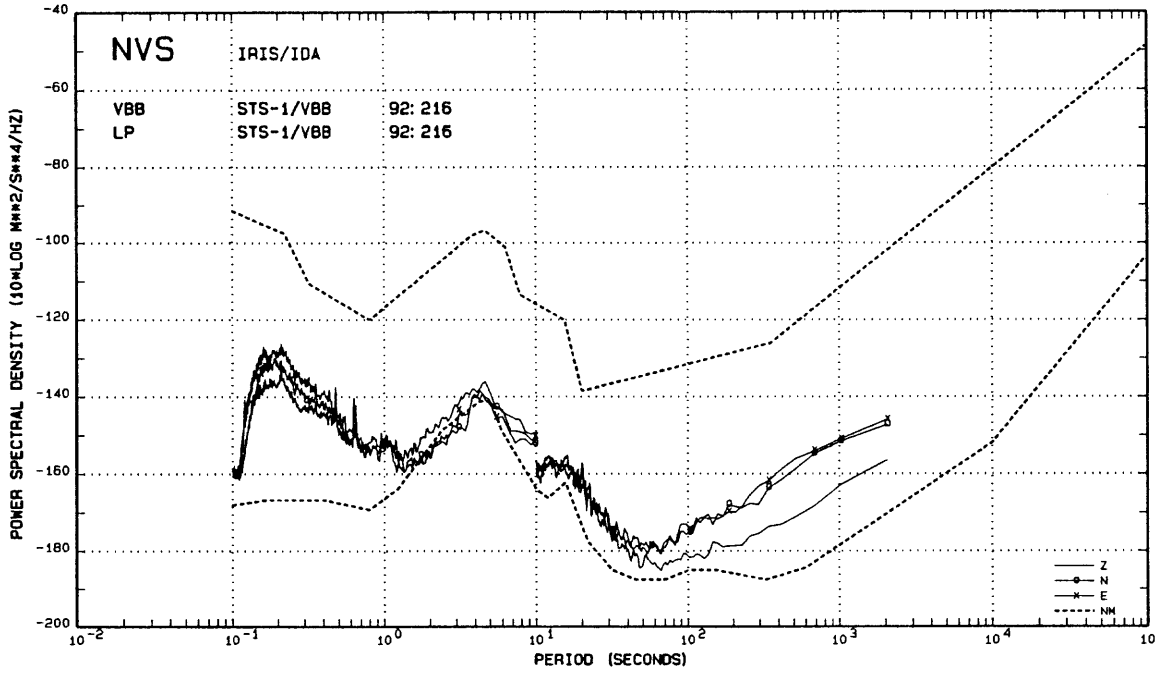

Figure A55.--Noise spectra from the Novosibirsk, Russia IRIS/IDA station.

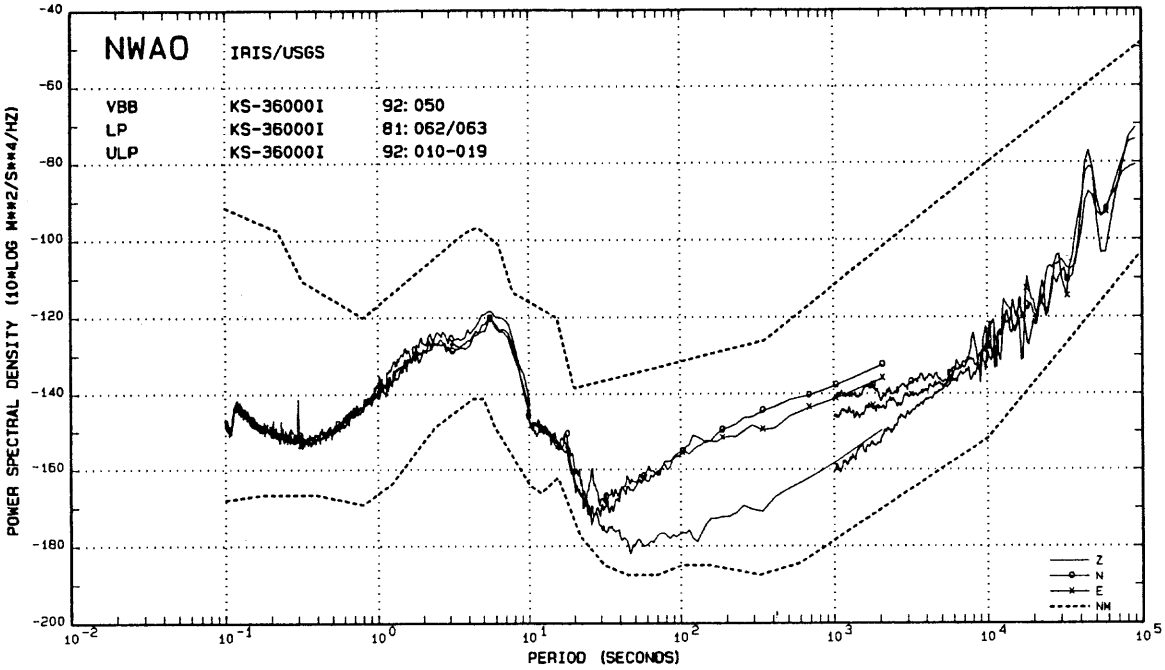

Figure A56.--Noise spectra from the Narrogin, Australia IRIS-2 station.

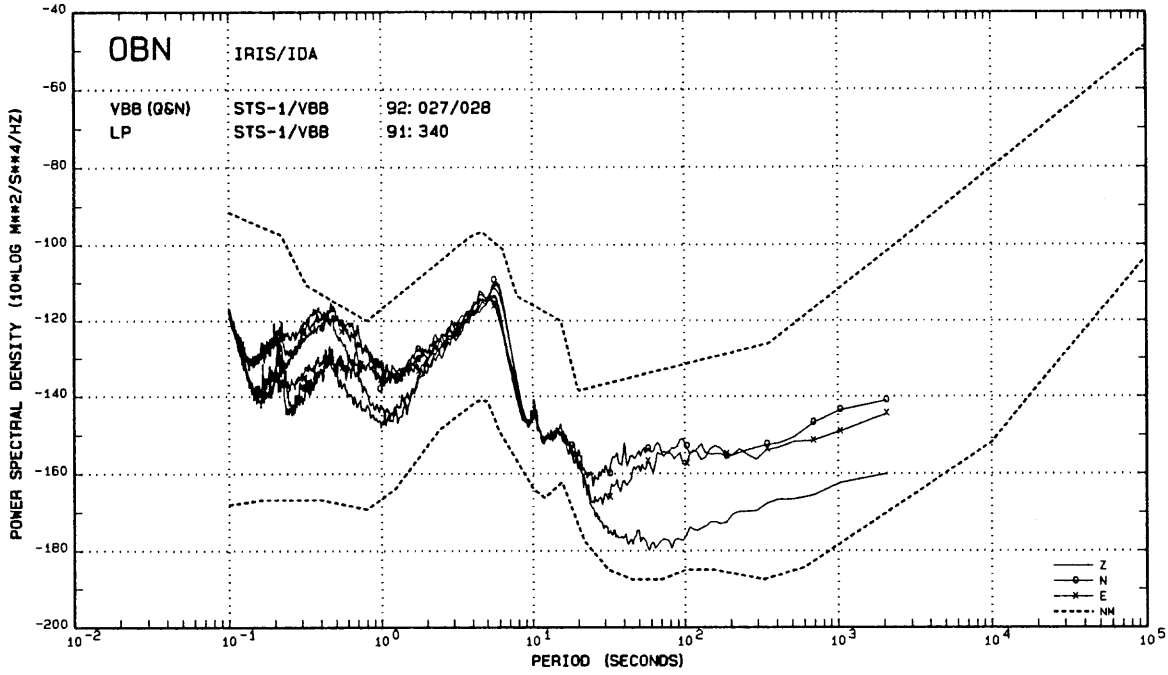

Figure A57.--Noise spectra from the Obninsk, Russia IRIS/IDA station.

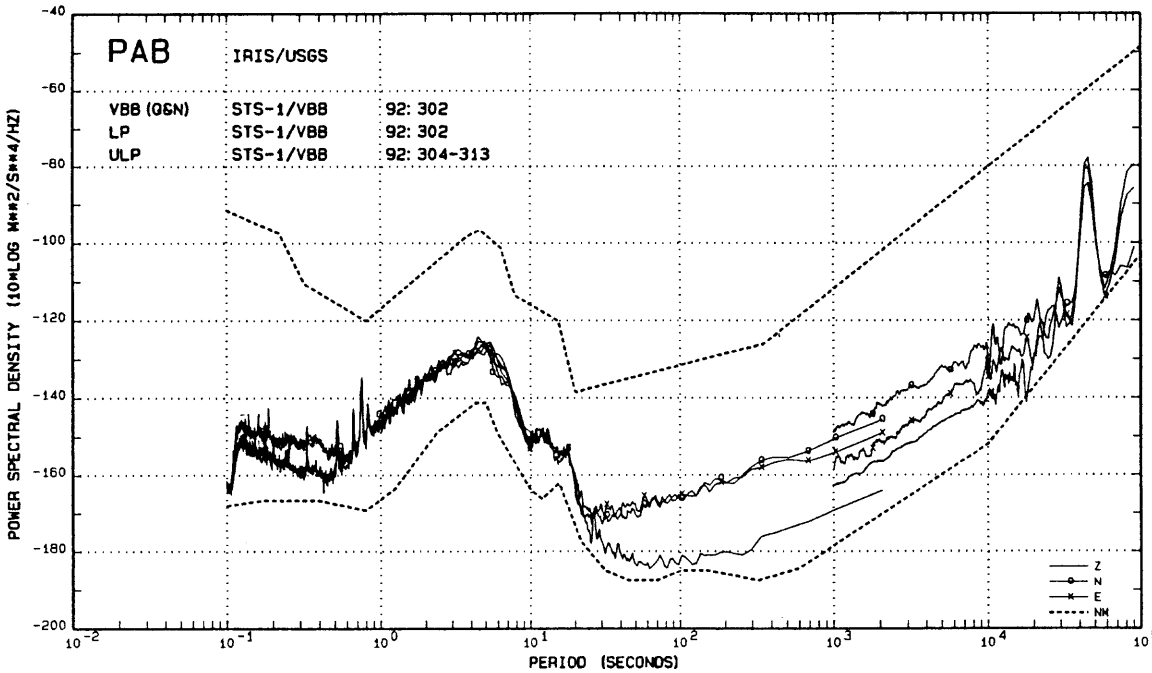

Figure A58.--Noise spectra from the San Pablo, Spain IRIS-2 station. Moving a system a relatively short distance (less than 50 km in this case) can make a dramatic improvement in background noise. Compare with the Toledo, Spain VBB noise spectra (Figure A83).

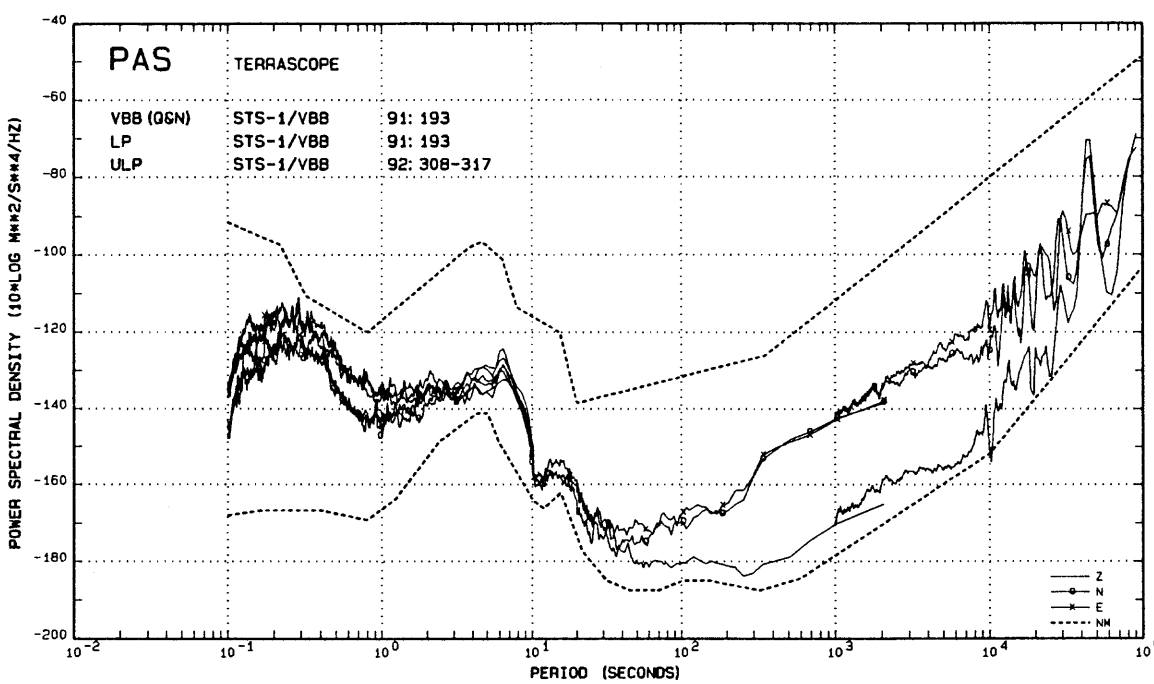

Figure A58.--Noise spectra from the Pasadena, California TERRAscope station.

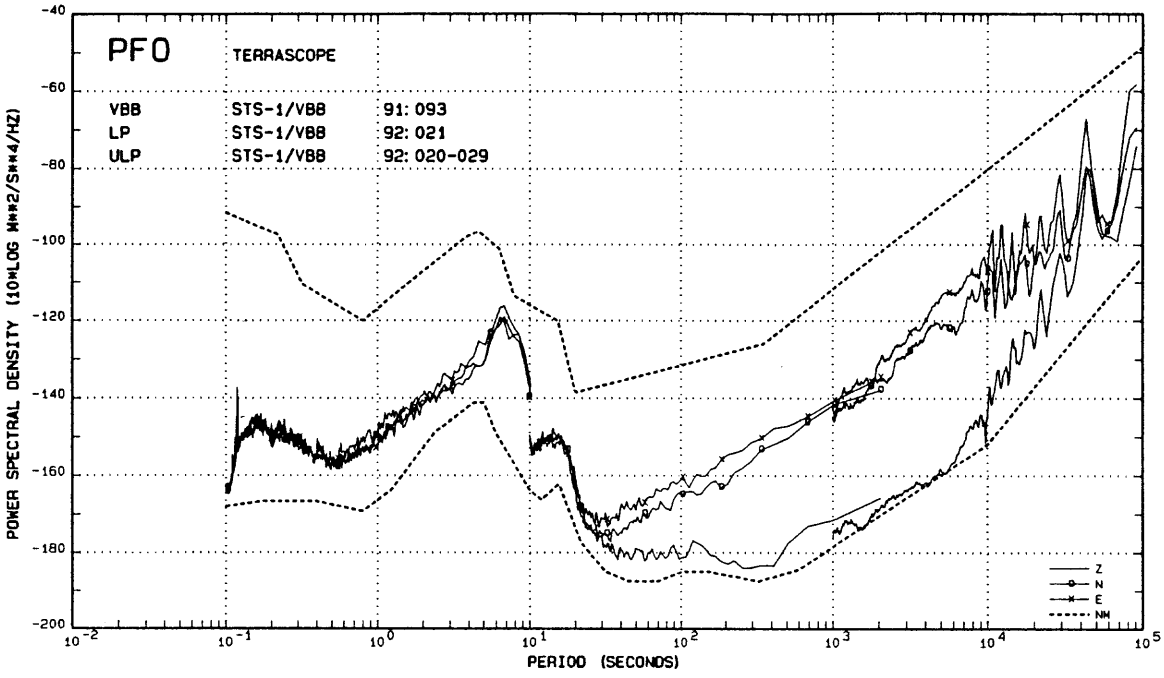

Figure A60.--Noise spectra from the Pinon Flat, California IRIS/IDA-TERRAscope station.

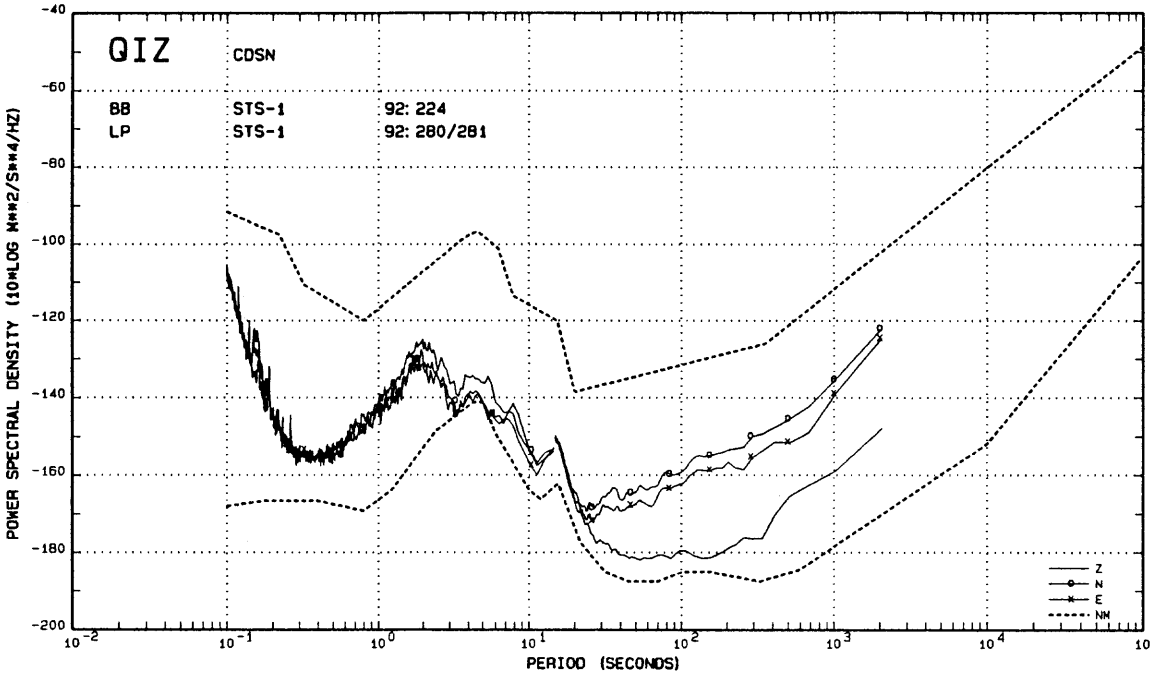

Figure A61.--BB and LP noise spectra from the Qiongshong, China CDSN station.

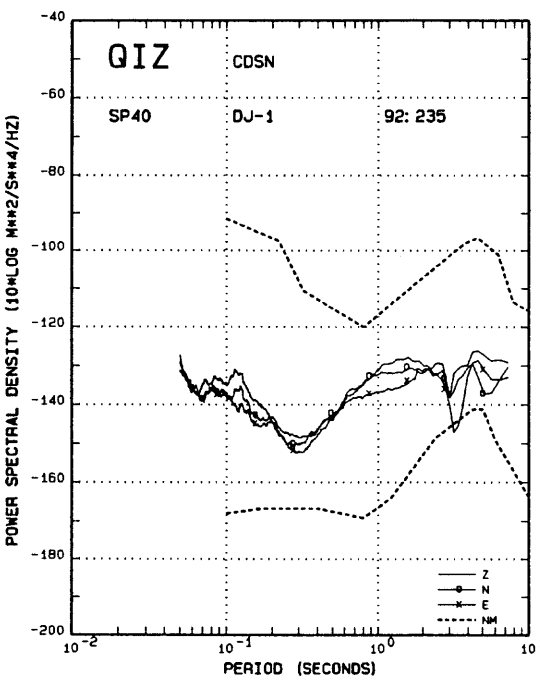

Figure A62.--SP noise spectra from the Qiongshong station.

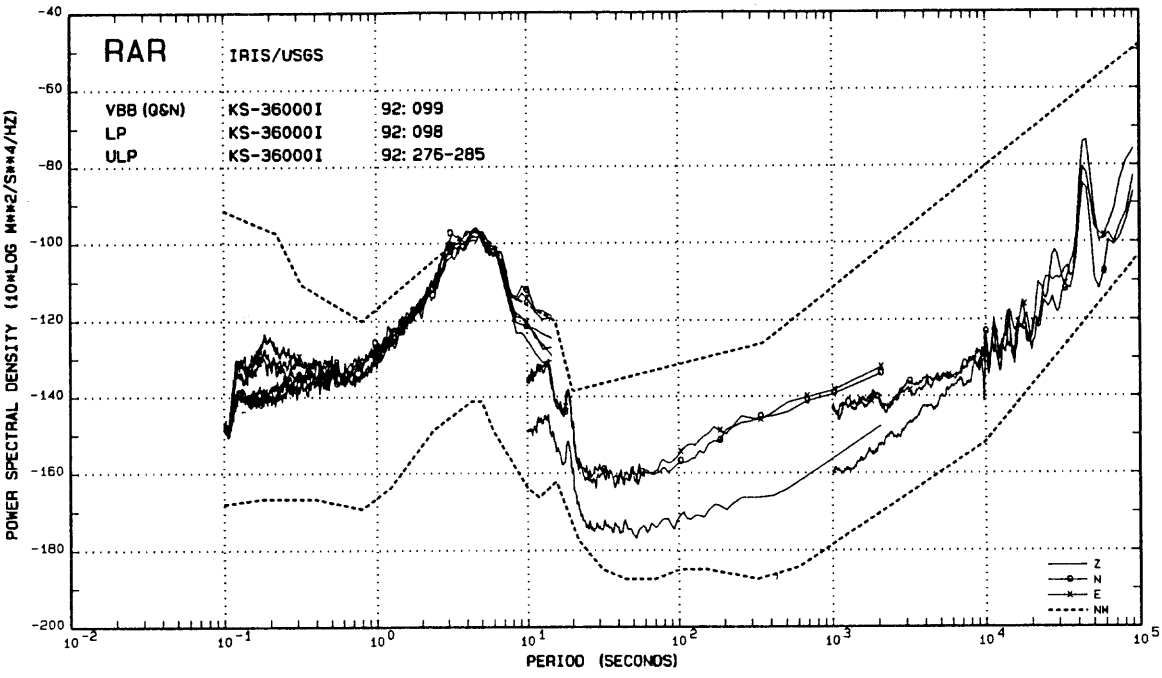

Figure A63.--Noise spectra from the Rarotonga, Cook Islands IRIS-2 station. This station and the Easter Island station shown below are important contributors to the high-noise model.

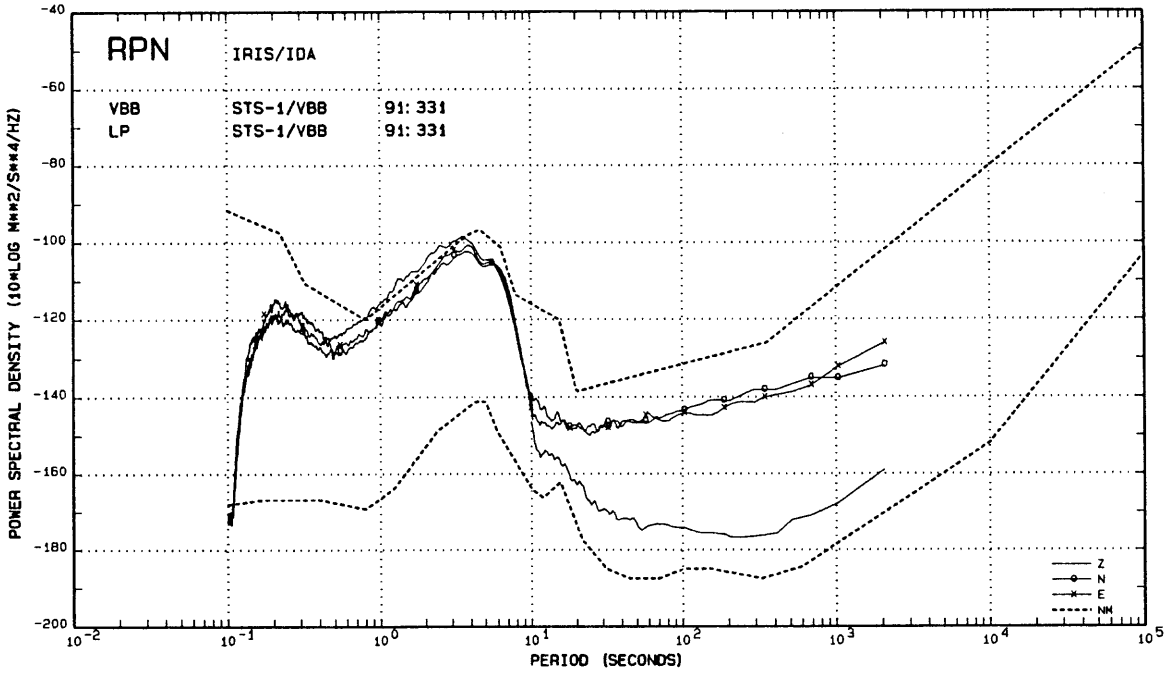

Figure A64.--Noise spectra from the Rapanui, Easter Island, Chile IRIS/IDA station.

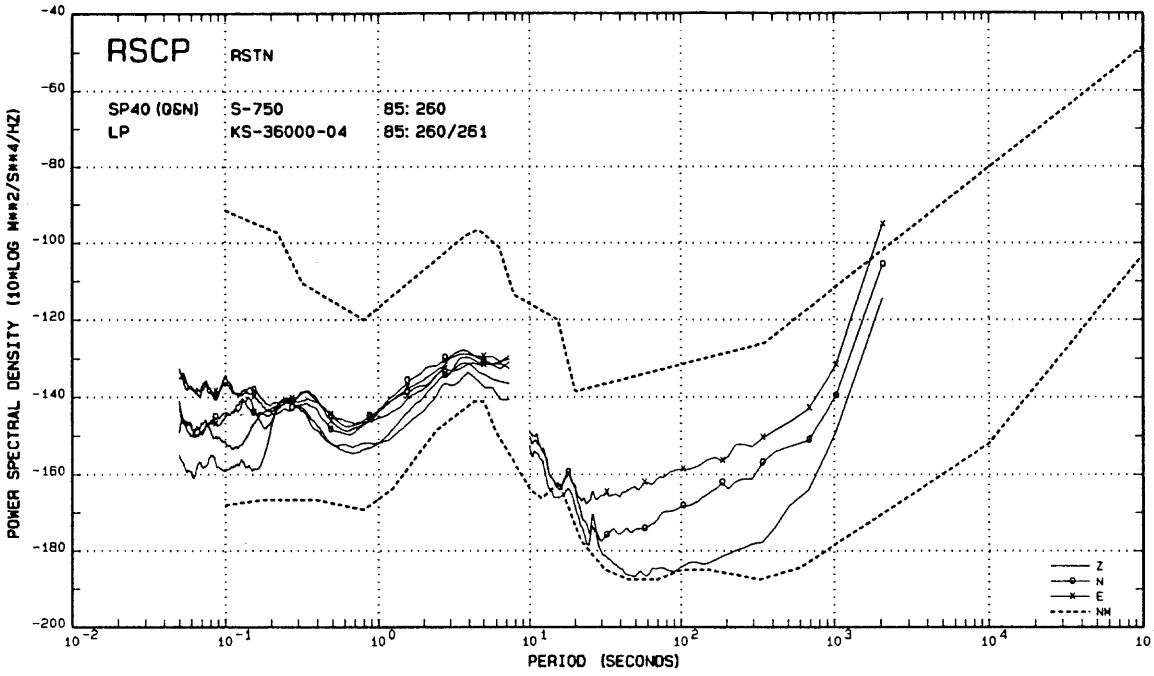

Figure A65.--Noise spectra from the Cumberland Plateau, Tennessee RSTN station.

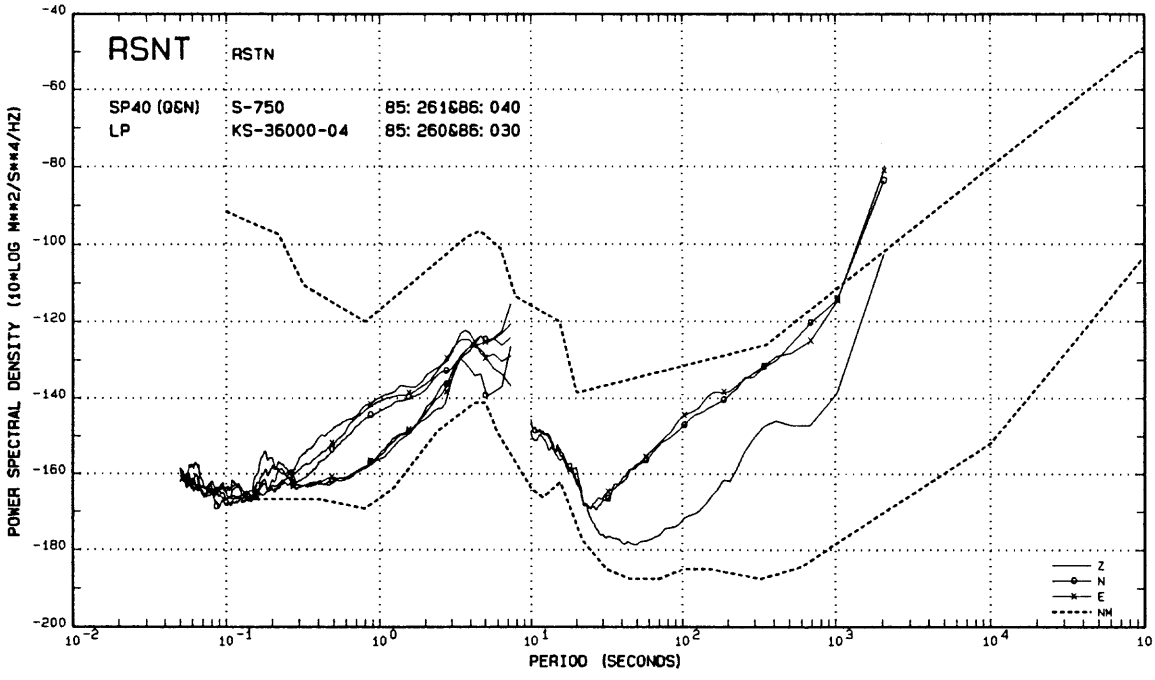

Figure A66.--Noise spectra from the Yellowknife, Canada RSTN station. In this figure the quiet and noisy SP spectra are from winter and summer seasons, respectively, possibly because of the effect of lake ice in reducing the amplitude of lake-generated microseisms.

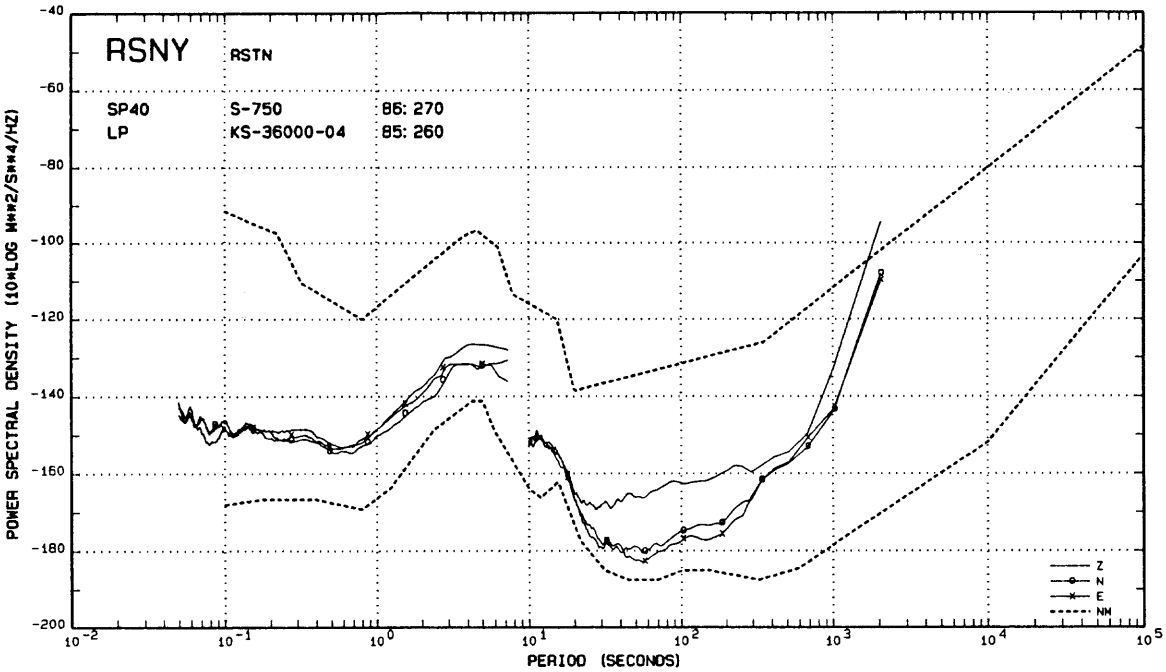

Figure A67.--Noise spectra from the Adirondack, New York RSTN station.

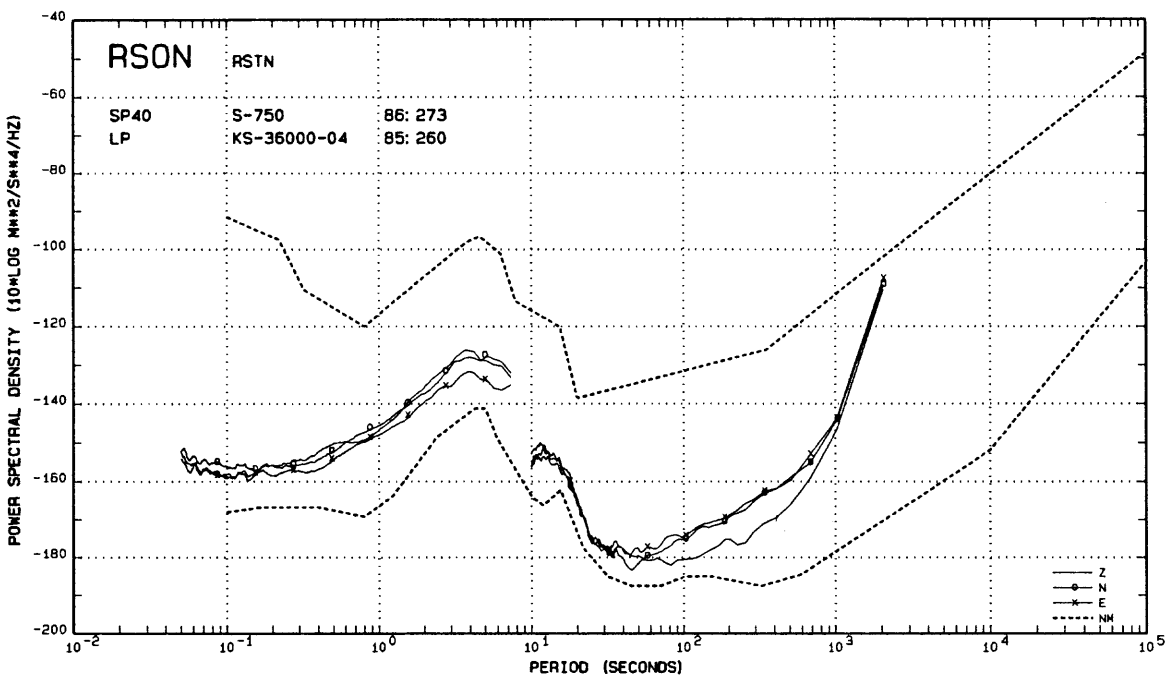

Figure A68.--Noise spectra from the Red Lake, Ontario, Canada RSTN station

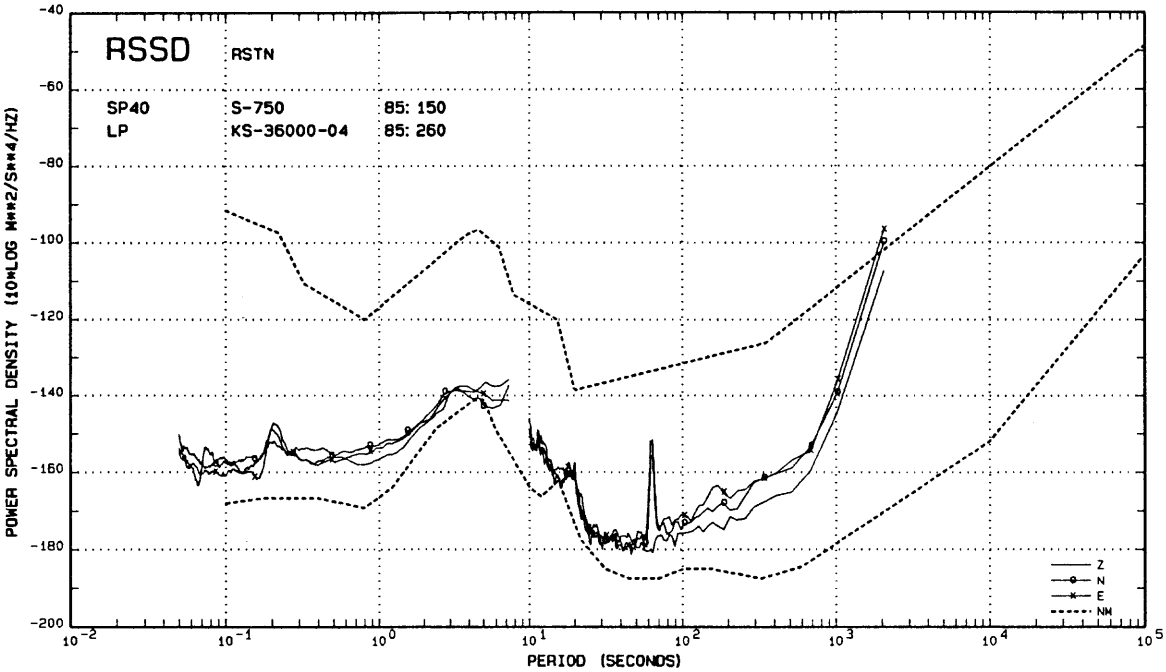

Figure A69.--Noise spectra from the Black Hills, South Dakota RSTN station.

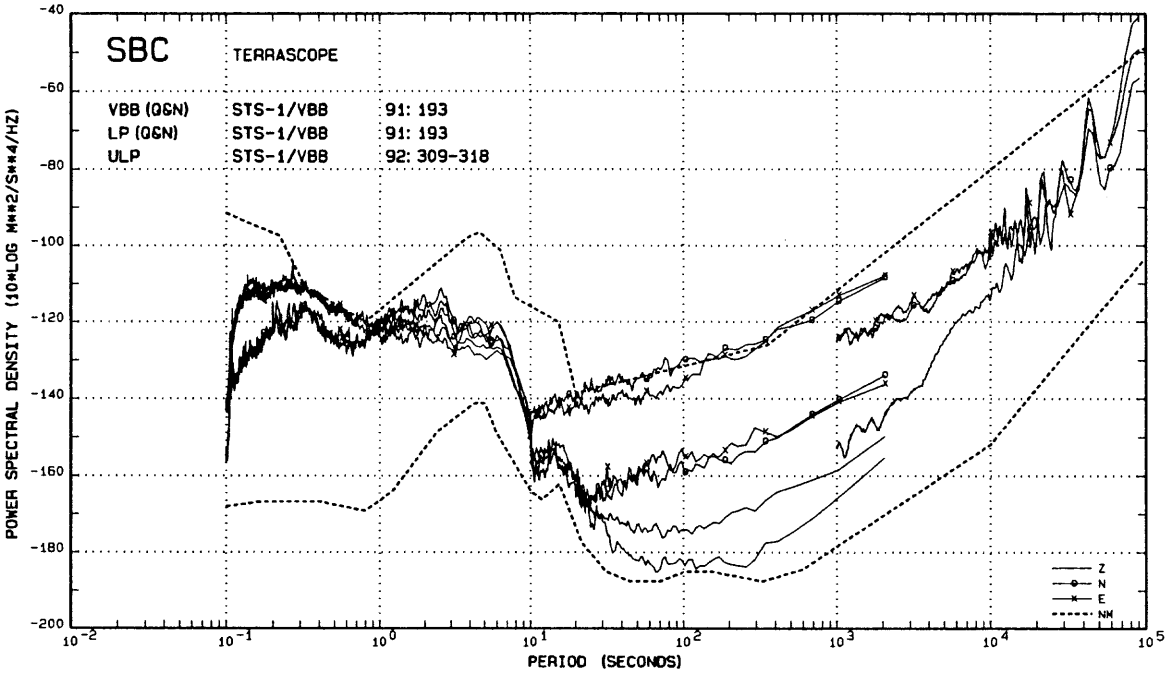

Figure A70.--Noise spectra from the Santa Barbara, California TERRAscope station. Both noisy and quiet LP spectra are shown.

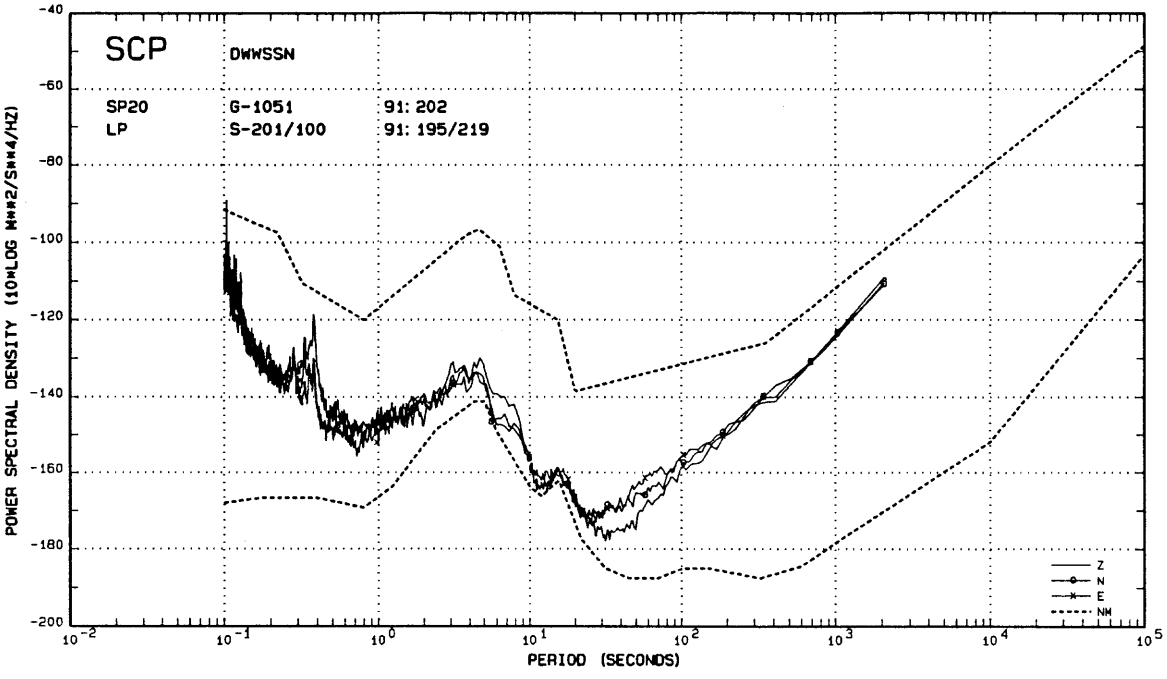

Figure A71.--Noise spectra from the State College, Pennsylvania DWWSSN station.

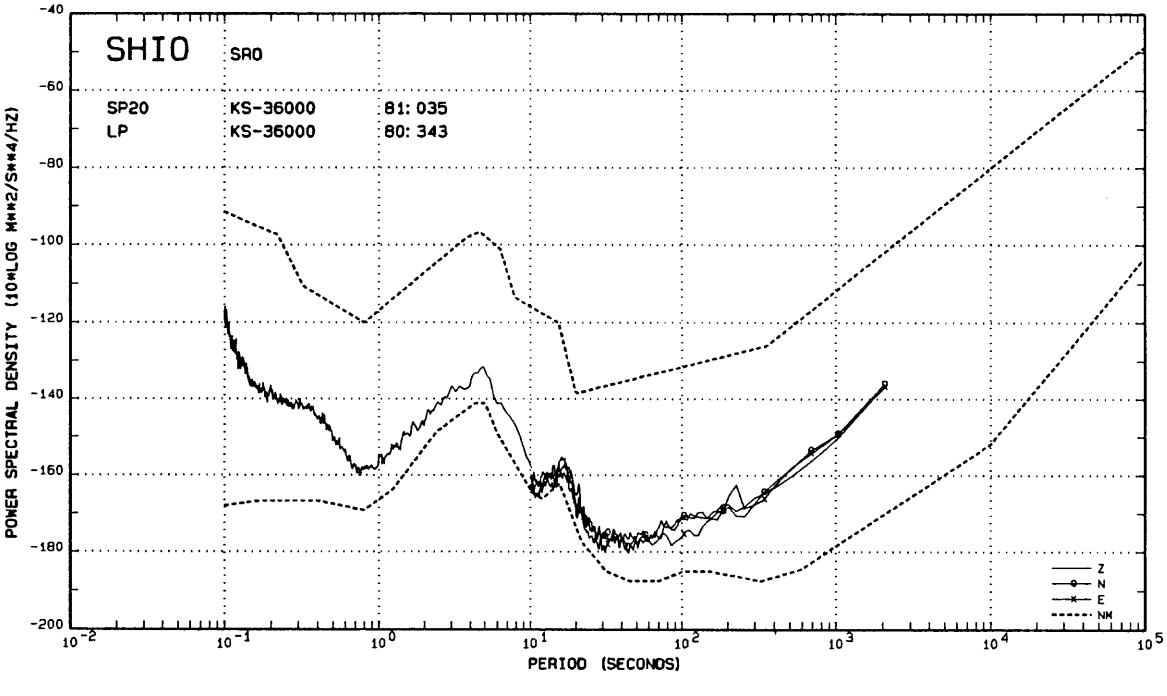

Figure A72.--Noise spectra from the Shillong, India SRO station. This SRO system is no longer in operation.

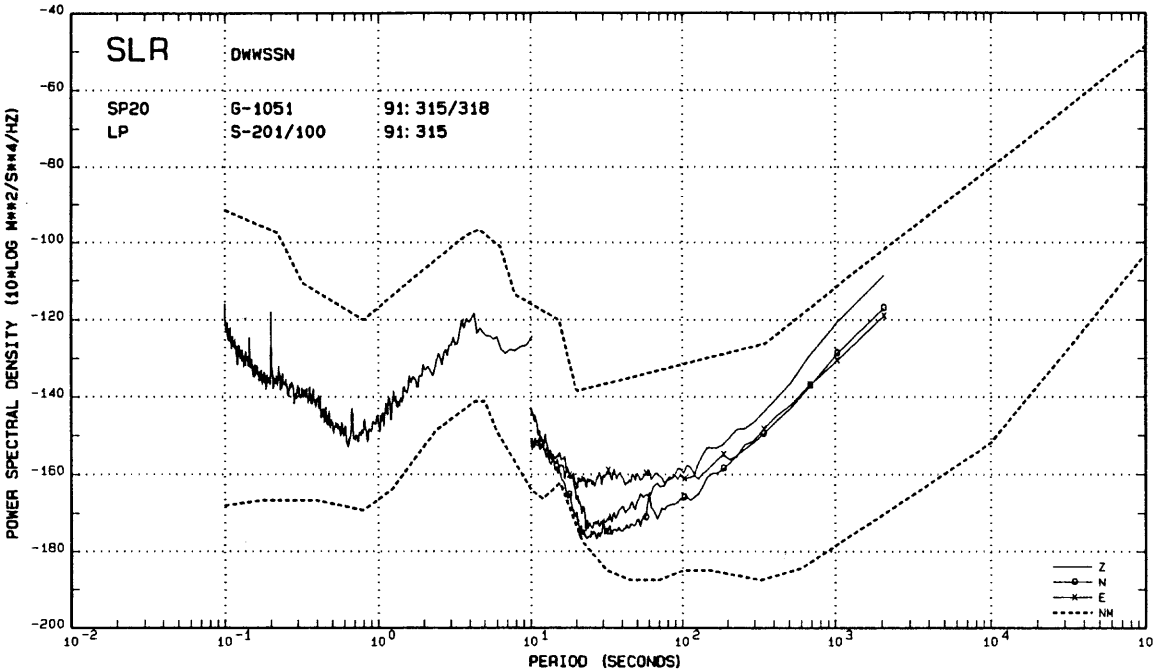

Figure A73.--Noise spectra from the Silverton, South Africa DWWSSN station.

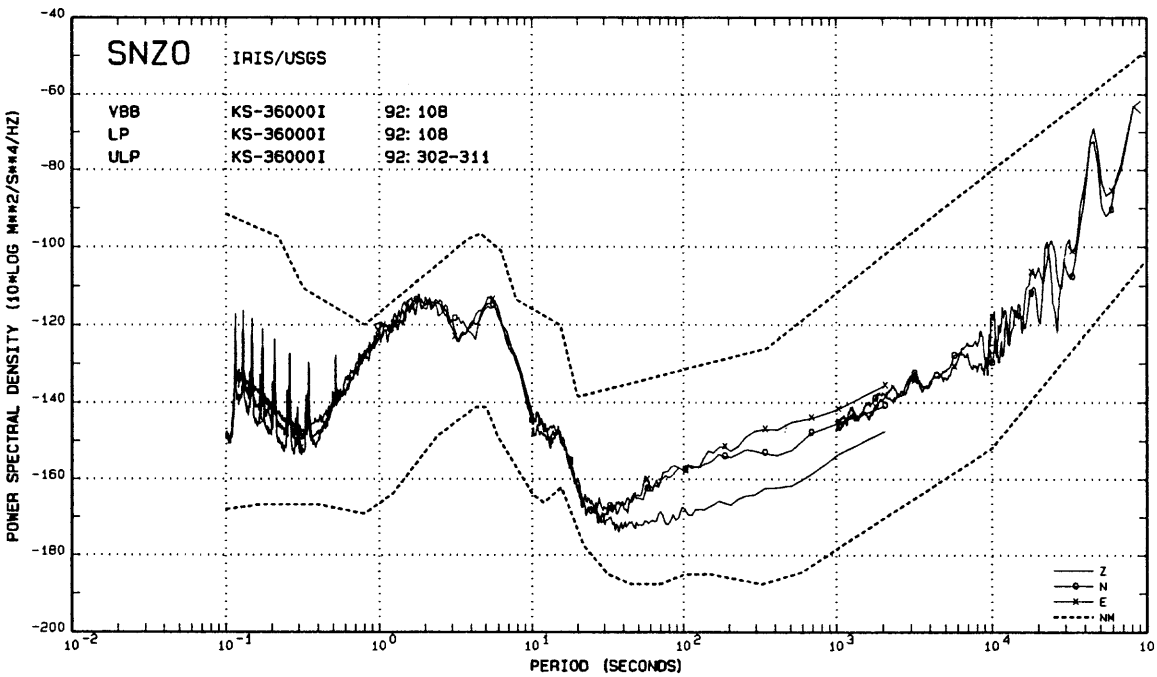

Figure A74.--Noise spectra from the South Karori, New Zealand IRIS-2 station. The source of the harmonic disturbances in the SP band is unknown but possibly instrumental.

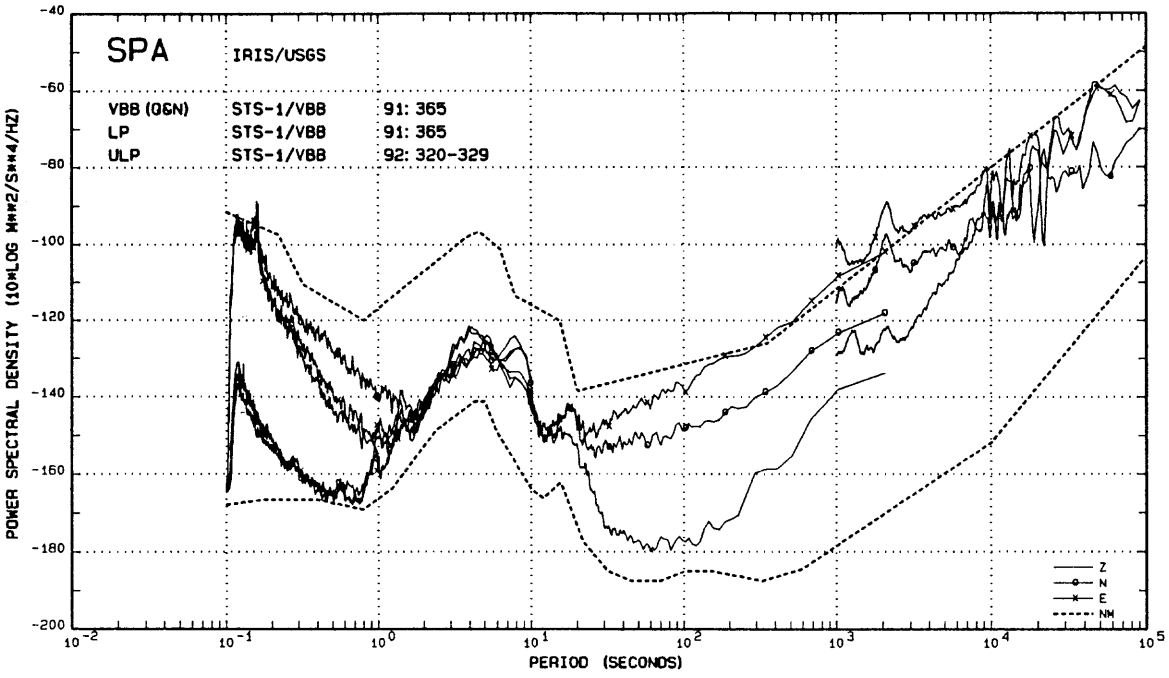

Figure A75.-- Noise spectra from the South Pole IRIS-2 station. This is a potentially very quiet site in the SP band. Unfortunately, there are local disturbances that adversely affect station operation much of the time. A separate short-period seismometer at an outlying telemetered site might be quite useful.

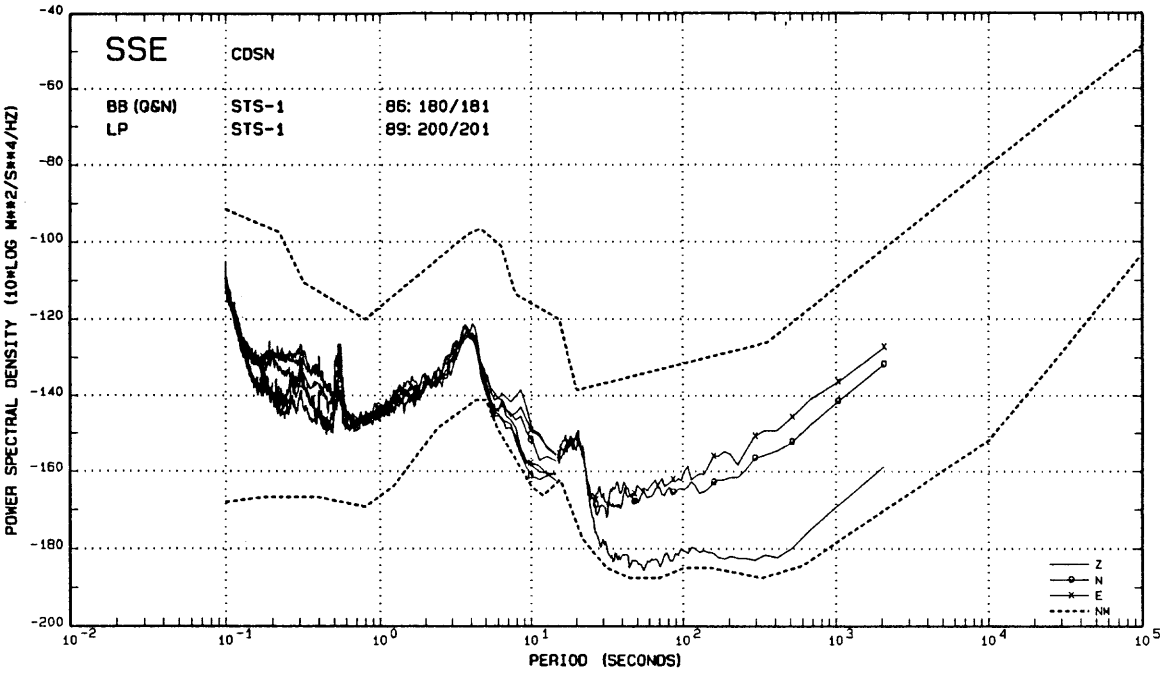

Figure A76.--BB and LP noise spectra from the Shanghai, China CDSN station.

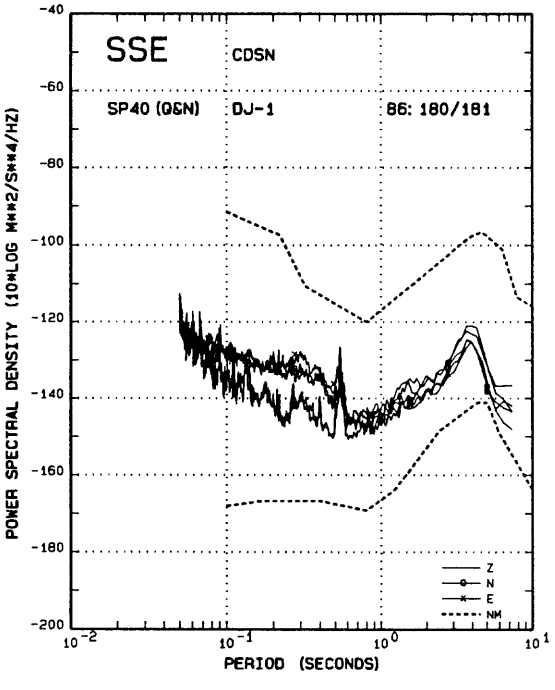

Figure A77.--SP noise spectra from the Shanghai station.

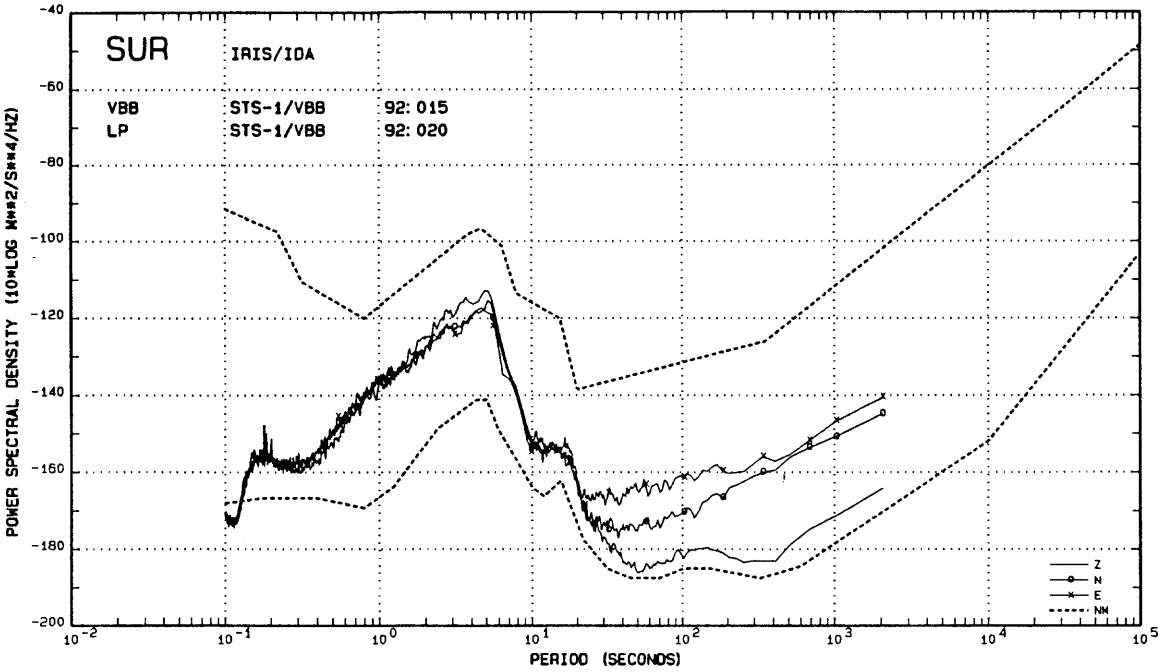

Figure A78.--Noise spectra from the Sutherland, South Africa IRIS/IDA station.

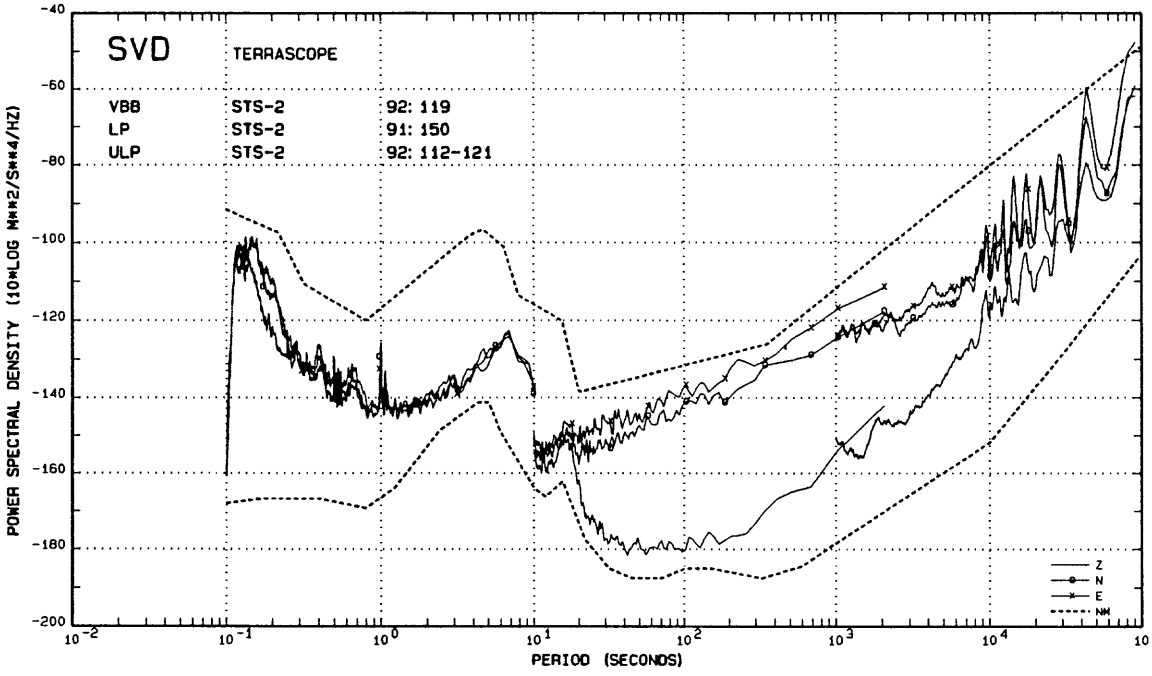

Figure A79.--Noise spectra from the Seven Oaks Dam, California TERRAscope station.

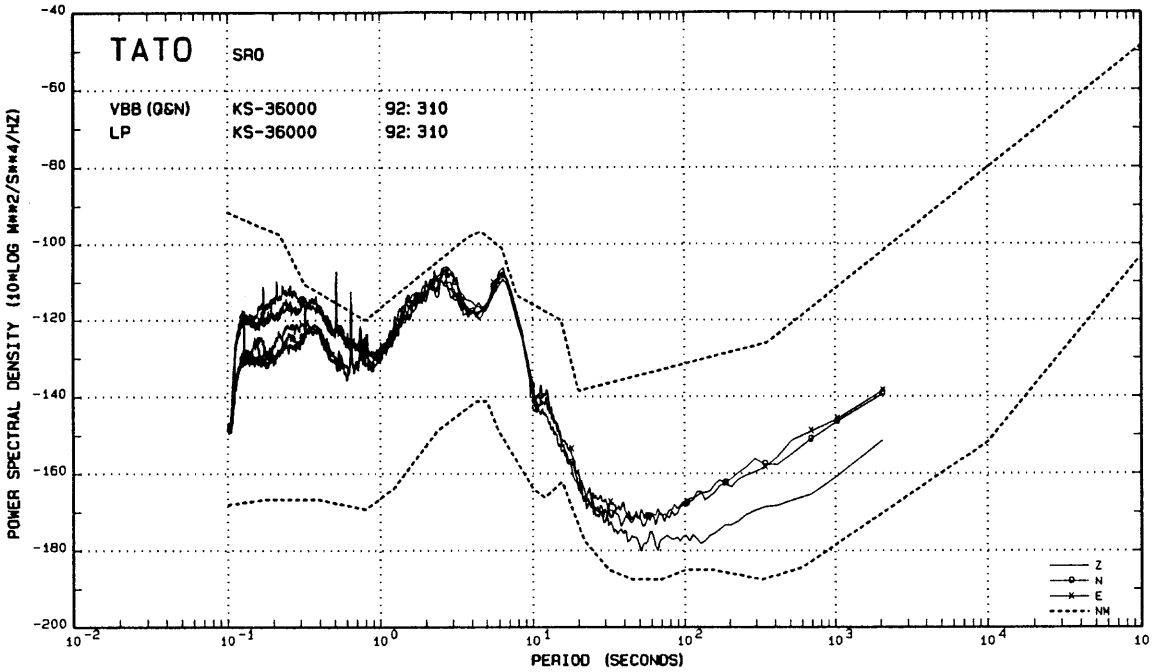

Figure A80.--Noise spectra from the Taipei, Taiwan IRIS-2 station.

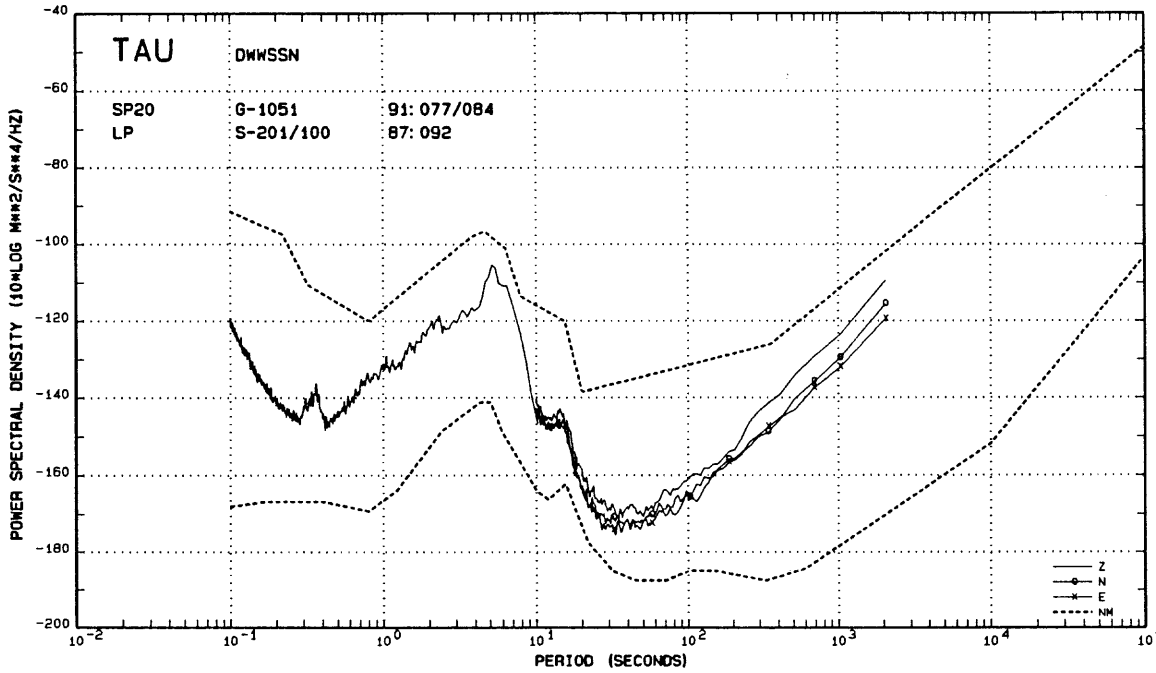

Figure A81.--Noise spectra from the Hobart, Tasmania, Australia DWWSSN station.

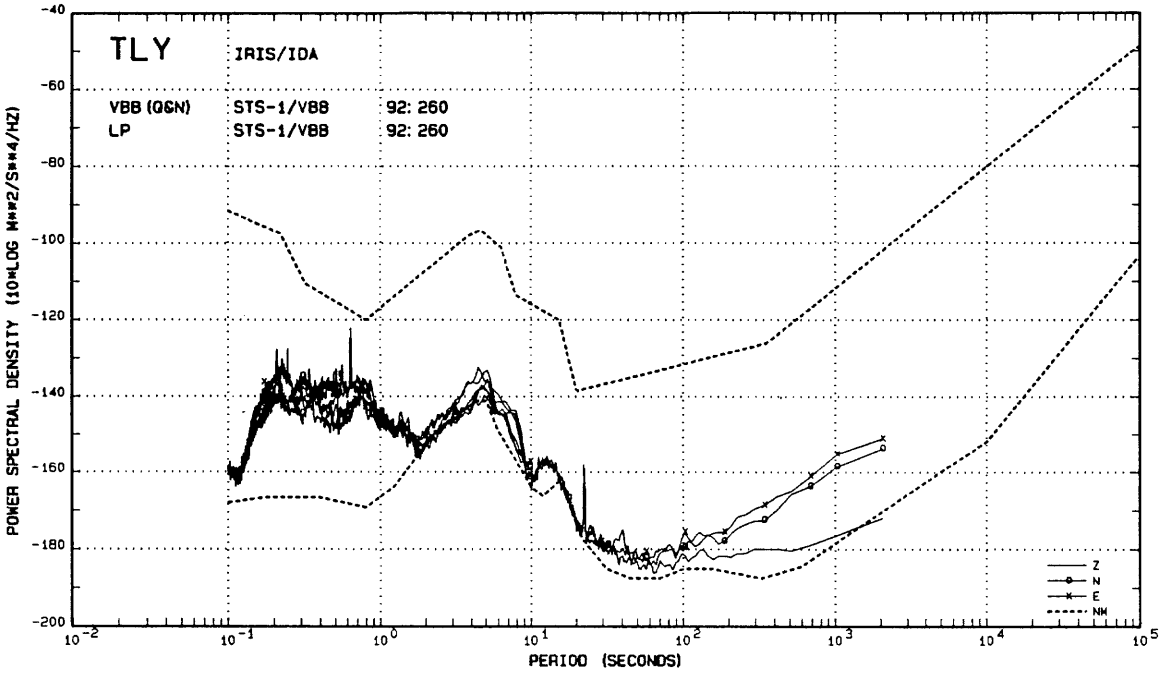

Figure A82.--Noise spectra from the Talaya, Russian Federation IRIS/IDA station.

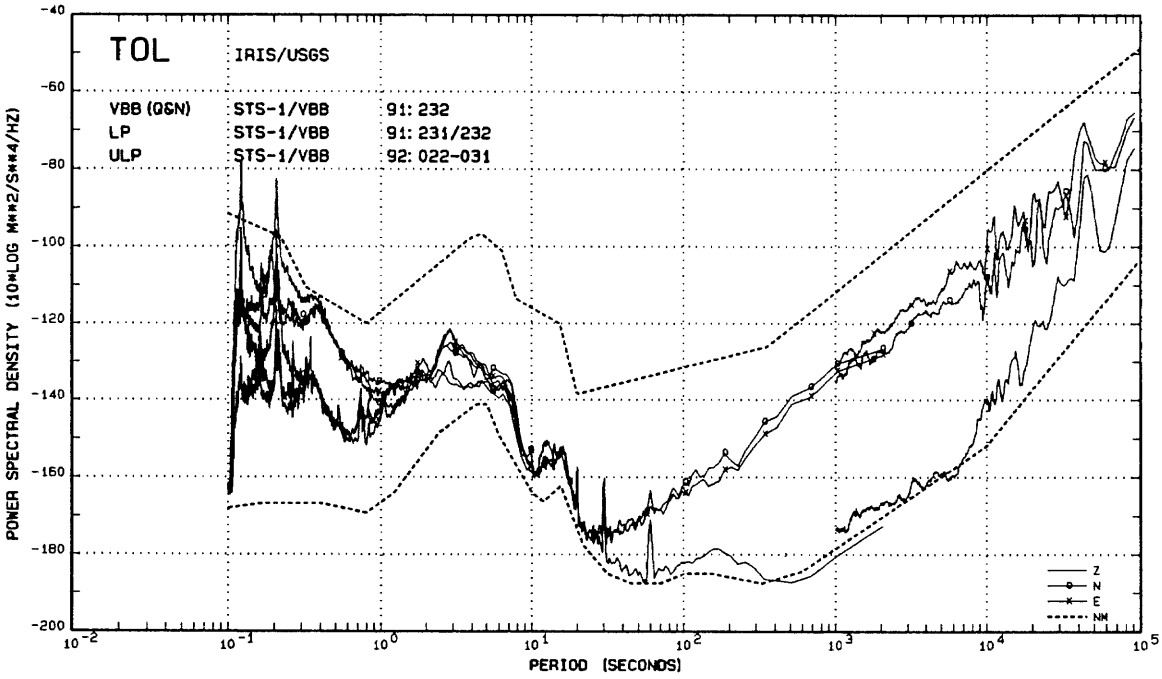

Figure A83.--Noise spectra from the Toledo, Spain IRIS-2 station. The IRIS-2 system has since been moved to San Pablo, Spain.

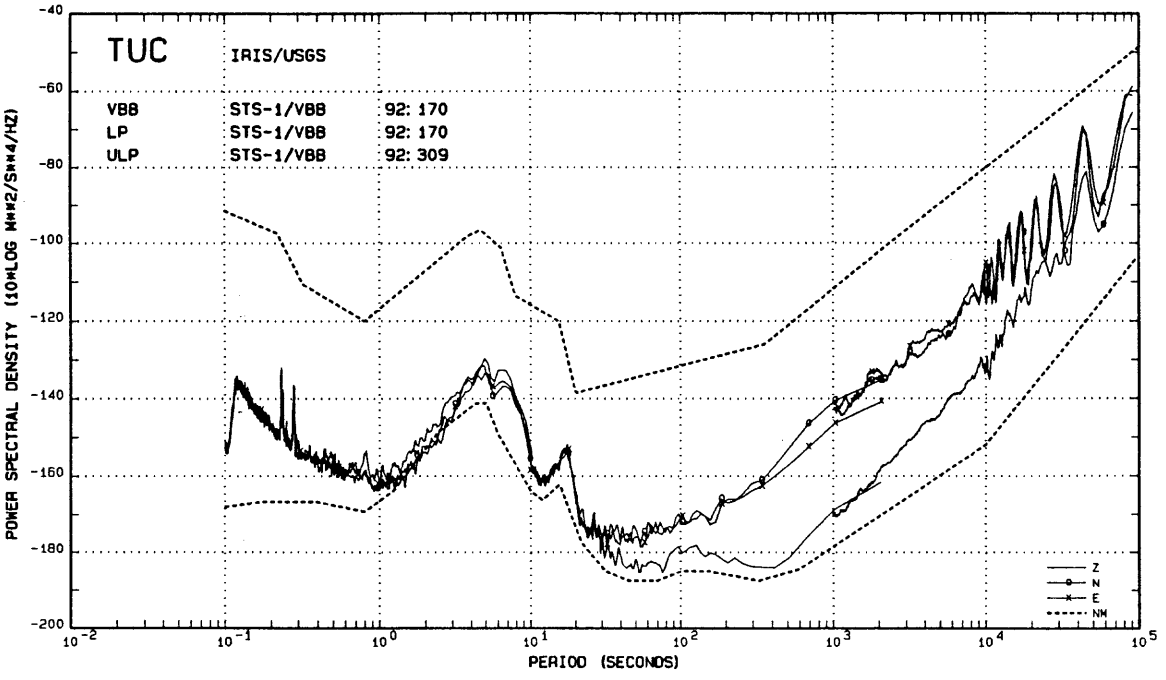

Figure A84.--Noise spectra from the Tucson, Arizona IRIS-2 station.

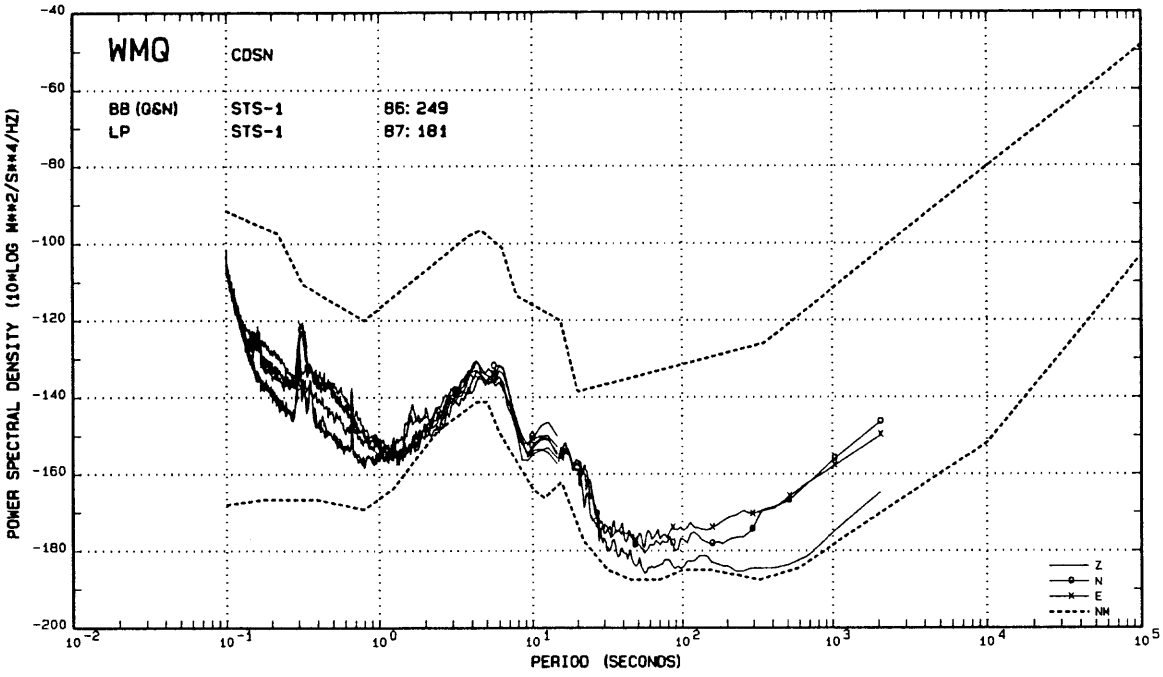

Figure A85.--BB and LP noise spectra from the Urumqi, China CDSN station.

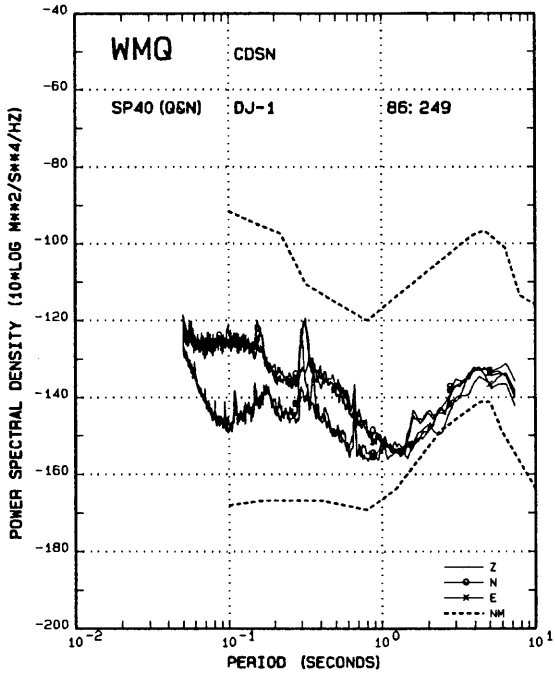

Figure A86.--SP noise spectra from the Urumqi station.

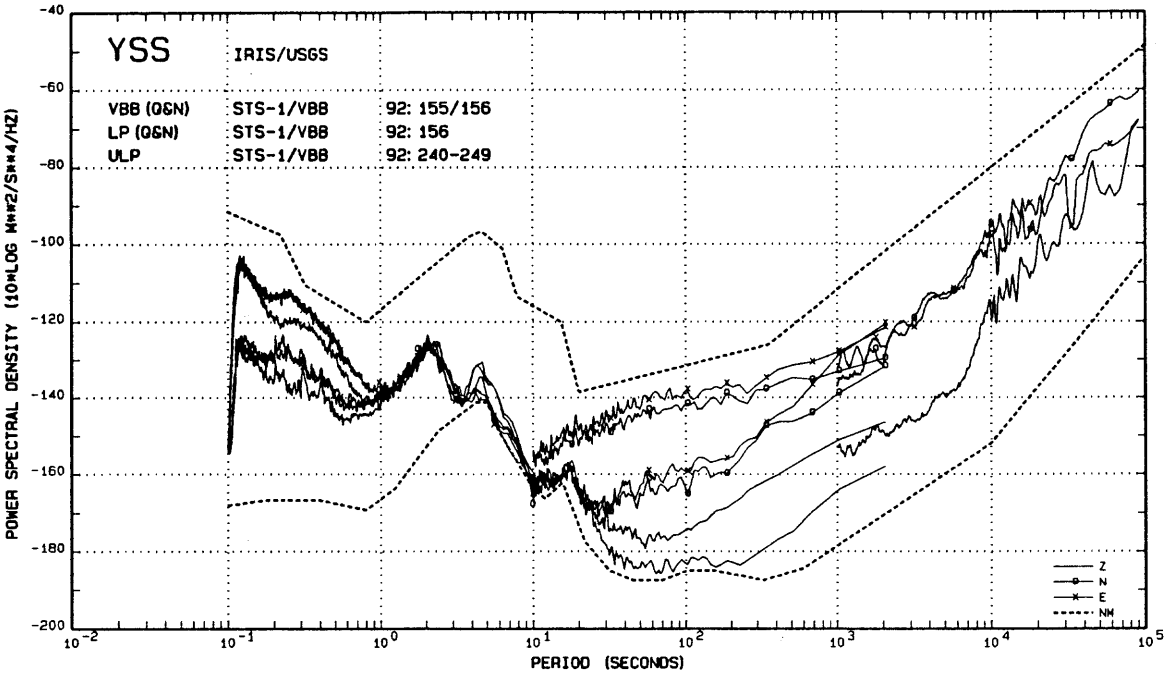

Figure A87.--VBB, LP, and ULP noise spectra from the Yuzhno-Sahkalinsk, Russia IRIS-2 station. Both noisy and quiet LP spectra are shown.

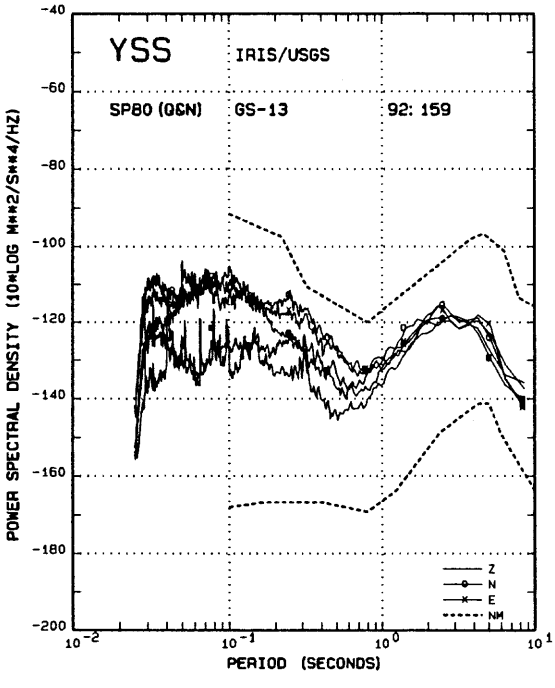

Figure A88.--SP noise spectra from the Yuzhno-Sakhalinsk station.

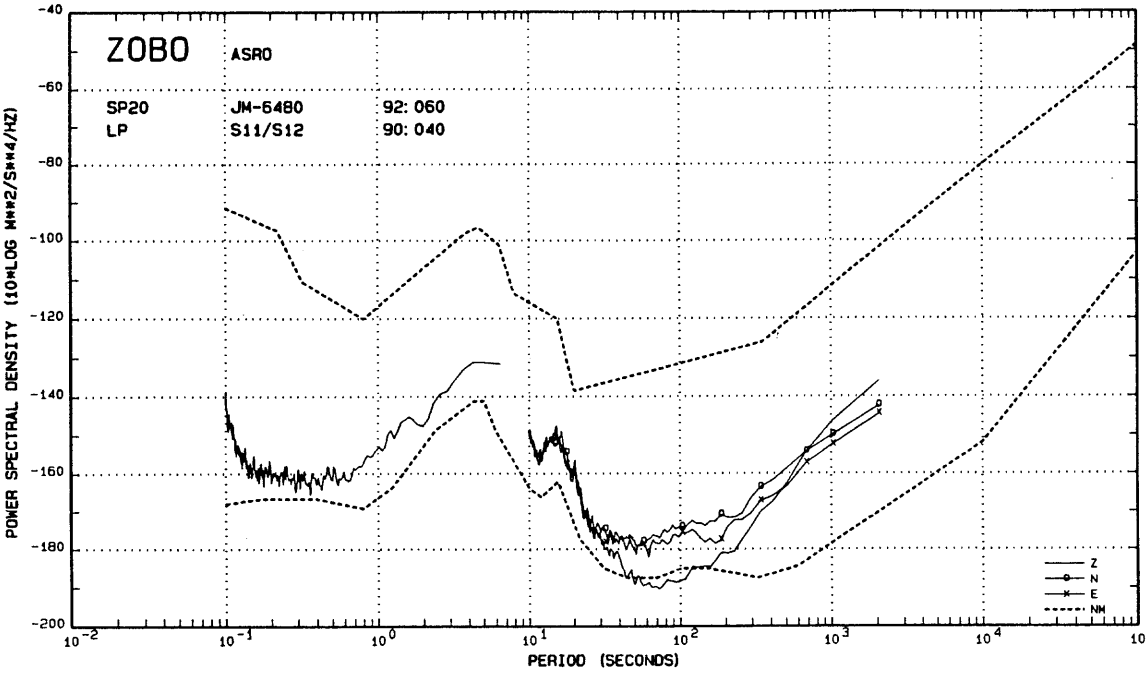

Figure A89.--Noise spectra from the Zongo Valley, Bolivia ASRO station.